A high order regularisation method for solving the Poisson equation and selected applications using vortex methods

PhD Thesis

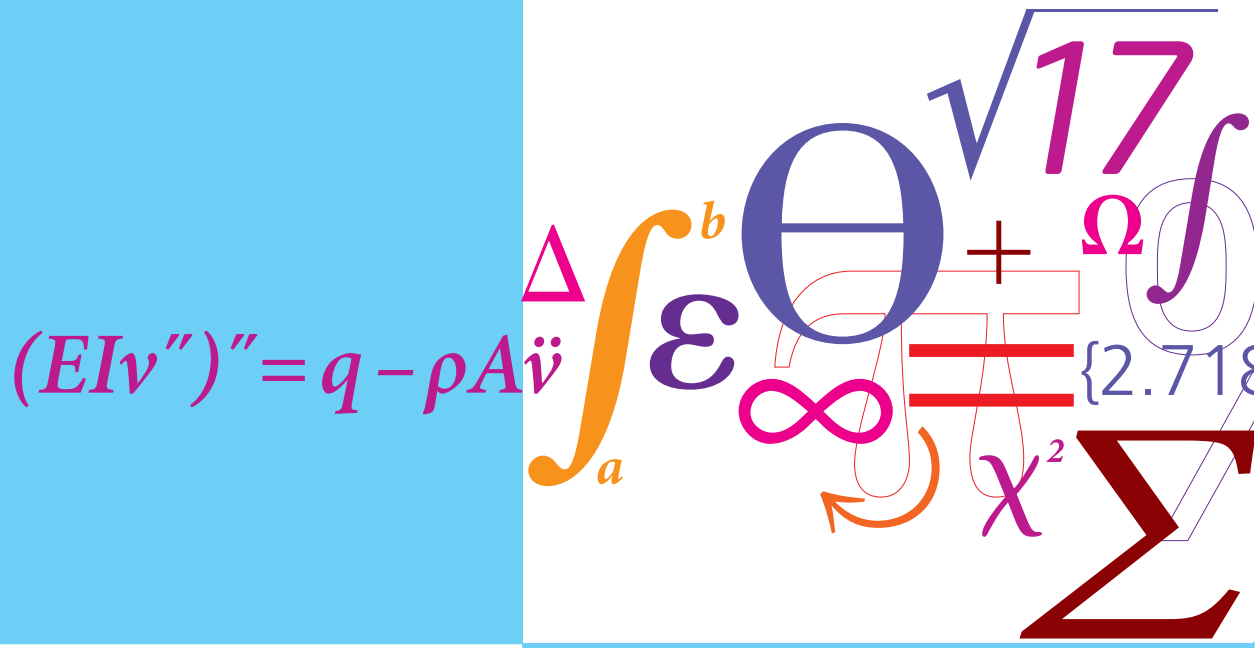

Mads Mølholm Hejlesen
DCAMM Special Report No. S198
February 2016

DTU Mechanical Engineering
Department of Mechanical Engineering

A high order regularisation method for solving the Poisson equation and selected applications using vortex methods

by
Mads Mølholm Hejlesen

A dissertation submitted for the degree of Philosophiae Doctor
at the Technical University of Denmark

Dissertation by:
Mads Mølholm Hejlesen

Supervisor:
Jens Honoré Walther

Institution:
Section for Fluid Mechanics, Coastal and Maritime Engineering
Department of Mechanical Engineering
Technical University of Denmark

Nils Koppels Allé, Building 403
DK-2800, Kgs. Lyngby, Denmark

ISBN	978-87-7475-444-2
Report ID-number:	DCAMM Special Report no. S198
Report type:	Ph.D. dissertation.
Project period:	1st November 2012 – 31st January 2016
Field:	Fluid Mechanics
Classification:	unclassified
Revision:	Last edited on: May 10, 2016
Remarks:	This dissertation is submitted as a partial fulfilment of the requirements for the degree of Philosophiae Doctor at the Technical University of Denmark.

Preface

This dissertation concludes the work carried out in a Ph.D. project at the Department of Mechanical Engineering at the Technical University of Denmark during the period of November 2012 to February 2016. The content of this dissertation is original work where large parts has been published in scientific journals or conference proceedings. The featured publications and planned journal submissions are listed below:

Published journal papers:

[1] **M. M. Hejlesen**, J. T. Rasmussen, A. Larsen and J. H. Walther. *On estimating the aerodynamic admittance of bridge sections by a mesh-free vortex method*. J. Wind Eng. Ind. Aerodyn., 146:117–127, 2015.

[2] **M. M. Hejlesen**, P. Koumoutsakos, A. Leonard, and J. H. Walther. *Iterative Brinkman penalization for remeshed vortex methods*. J. Comput. Phys., 280:547–562, 2015.

[3] **M. M. Hejlesen**, J. T. Rasmussen, P. Chatelain, and J. H. Walther. *A high order solver for the unbounded Poisson equation*. J. Comput. Phys., 252:458–467, 2013.

[4] J. T. Rasmussen, **M. M. Hejlesen**, A. Larsen, and J. H. Walther. *Discrete vortex method simulations of the aerodynamic admittance in bridge aerodynamics*. J. Wind Eng. Ind. Aerodyn., 98:754–766, 2010.

Journal submissions:

[5] **M. M. Hejlesen**, H. J. Spietz, and J. H. Walther. *A regularisation method for solving the Poisson equation with mixed periodic and free-space boundary conditions*. J. Comput. Phys., planned submission in 2016.

[6] **M. M. Hejlesen** and J. H. Walther. *A multi-resolution regularization method for solving the unbounded Poisson equation*. in review for J. Comput. Phys.

[7] **M. M. Hejlesen**, and J. H. Walther. *Stochastically generated turbulence with improved kinematic properties*. in review for J. Comput. Phys.

Conference papers:

[8] **M. M. Hejlesen**, H. J. Spietz, and J. H. Walther. *Simulations of a single vortex ring using an unbounded, regularized particle-mesh based vortex method*. Proceedings of the 6th International Conference on Vortex Flows and Vortex Models, Nagoya, Japan, 2014.

[9] **M. M. Hejlesen**, J. T. Rasmussen, P. Chatelain, and J. H. Walther. *High order Poisson solver for unbounded flows*. IUTAM Procidea, 18:56–65, 2015.

The layout and structure of the dissertation

The topics studied in this project spans a wide range of different fields and disciplines. From mathematical physics to selected applications in fluid mechanics, the topics varies from being quite general with relevance in many scientific fields to being focused on one specific application. Therefore, this dissertation is structured such that the topics are kept separate in order to maintain both the generality and specificity of the individual subjects although there naturally also exists many connections and similarities between topics. In specific, this dissertation is divided into two parts where the first part consists of a monograph which deals with the most general and the second part consists of individual articles.

The first part of this dissertation addresses the solution to a specific type of equation which is often encountered in physical systems. That is the Poisson equation. A formal derivation of the homogeneous solutions i.e. the Green's function subject to different boundary conditions is presented in Chapter I-1, the numerical implementation is introduced in Chapter I-2 and the validation of the numerical solver is established in Chapter I-3.

The second part consists of four standalone articles which presents selected topics and applications of vortex methods. Article II-1 presents the simulation and advanced field analysis of the instability, transition to turbulence and eventual destruction of a single vortex ring. Article II-2 introduces a novel implementation and improvement of the Brinkman penalisation method which is used in vortex methods to simulate the fluid-solid interface. Article II-3 is a further discussion and validation of a previously presented stochastic method that simulates the effect of an oncoming turbulent flow past a bridge deck cross-section. Article II-4 is a short note that expands the stochastic turbulence generator used in Article II-3 to a vorticity formulation with improved kinematic properties in the generated turbulent flow field.

Developed software

During the project an MPI-based FORTRAN library `pmlib` was developed. The library contains routines for simulating fluid flow using the particle-mesh method to solve the vorticity formulation of a fluid. The library is inspired by the high performance computing library `ppm` (Sbalzarini et al., 2006) developed at ETH Zürich.

Acknowledgements

A part of the research presented in this dissertation has been supported by the Danish Research Council of Independent Research (Grant. No. 274-08-0258) and support from the COWI foundation. Computer resources was made available by the Department of Physics at DTU through the Danish Center for Scientific Computing (DCSC).

Although they are only sparsely cited in the dissertation, I would like to acknowledge some text-books which has given me a better understanding of the subject and have greatly inspired my research: *Vortex Methods – Theory and Practice* by Cottet and Koumoutsakos (Cottet and Koumoutsakos, 2000), *Vortex Dynamics* by Saffman (Saffman, 1992), *Vorticity and vortex dynamics* by Wu, Ma, and Zhou (Wu et al., 2006a), and *Computer Simulation Using Particles* by Hockney and Eastwood (Hockney and Eastwood, 1988). On a similar note I would like to acknowledge the online video lectures of Leonard Suskind (Stanford University), Gilbert Strang (Massachusetts Institute of Technology), and Venkataraman Balakrishnan (Indian Institute of Technology Madras).

I would like to acknowledge the co-authors of the publications which this dissertation is build on: Jens Honoré Walther, Johannes Tophøj Rasmussen, Allan Larsen, Philippe Chatelain, Anthony Leonard, and Petros Koumoutsakos. I would also like to acknowledge the helpful discussions with Grégoire Winckelmans, George-Henri Cottet, Ivo Sbalzarini and Wim van Rees.

I thank the Computational Science and Engineering Laboratory, at ETH Zürich for hosting a short visit during the project and also for providing the `ppm` library which has served as a starting point for my own numerical implementation.

A special thanks to Jens Honoré Walther, my supervisor, for his invaluable support and council throughout the project. I especially owe him many thanks for allowing me the freedom to pursue many different ideas and topics in my studies and to always provide a constructive perspective on things. This has been a most valued privilege that has provided me with much inspiration and motivation, a deeper general understanding of physics and have played a key role in both my scientific as well as personal development – one could not ask for a better mentor!

Mads Mølholm Hejlesen
DTU, Kgs. Lyngby, Denmark
February 2016.

Abstract

A regularisation method for solving the Poisson equation using Green's functions is presented. The method is shown to obtain a convergence rate which corresponds to the design of the regularised Green's function and a spectral-like convergence rate is obtained using a spectrally ideal regularisation. It is shown that the regularised Poisson solver can be extended to handle mixed periodic and free-space boundary conditions. This is done by solving the equation spectrally in the periodic directions which yields a modified Helmholtz equation for the free-space directions which in turn is solved by deriving the appropriate regularised Green's functions. Using an analogy to the particle-particle particle-mesh method, a framework for calculating multi-resolution solutions using local refinement patches is presented. The regularised Poisson solver is shown to maintain a high order converging solution for different configurations of the refinement patches.

The regularised Poisson solver has been implemented in a high order particle-mesh based vortex method for simulating incompressible fluid flow. A re-meshing of the vortex particles is used to ensure the convergence of the method and a re-projection of the vorticity field is included to explicitly fulfil the kinematic constraints of the flow field. The high order, unbounded particle-mesh based vortex method is used to simulate the instability, transition to turbulence and eventual destruction of a single vortex ring. From the simulation data, a novel analysis on the vortex ring dynamics is presented based on the alignment of the vorticity vector with the principal axis of the strain rate tensor.

A novel iterative implementation of the Brinkman penalisation method is introduced for the enforcement of a fluid-solid interface in re-meshed vortex methods. The iterative scheme is shown to improve the enforcement of the interface and also allow the simulation to perform significantly larger time steps, than what is customary for the method. The improved accuracy of the iterative implementation is demonstrated by considering challenging benchmark problems such as the impulsively started flow past a cylinder and a flat plate normal or inclined to the flow. The iterative implementation is shown to enhance the quality of the solution by Brinkman penalisation significantly for simulations of highly unsteady flows past complex geometries.

A stochastic method of generating a synthetic turbulent flow field is combined with a 2D mesh-free vortex method to simulate the effect of an oncoming turbulent flow on a bridge deck cross-section within the atmospheric boundary layer. The mesh-free vortex method is found to be capable of preserving the a priori specified statistics as well as anisotropic characteristics of the synthesized turbulent flow field. From the simulation, the aerodynamic admittance is estimated and the instantaneous effect of a time varying angle of attack is briefly investigated. The obtained aerodynamic admittance of four aerodynamically different bridge sections are compared to available wind tunnel data, showing good agreement between the two.

A vorticity formulated stochastic turbulence generator is presented which improves the kinetic properties of the generated turbulent field compared to present methods. Additional measures, such as explicit high order smoothing of the flow field, is introduced to insure that the generated field can be introduced into numerical simulations without an excessive loss of energy due to numerical dissipation.

Contents

Part A:

A high order regularised solver for the Poisson equation

Introduction

Conservation laws form the most essential axioms in physical systems and is often associated with an underlying principle of symmetry. The conservation of flux and circulation subject to a spherical symmetry describe phenomena such as the radiation from a source quantity or some of the fundamental interactions between objects of a system e.g. the gravitational or electro-magnetic force. Considering the limit of the infinitesimal point of a continuous field, the conservation of flux and circulation is described for the vector field in a differential formulation. Here the total flux and circulation becomes source/sink and rotation densities given by the fundamental operations of divergence and curl, respectively. A mathematical and often a physical simplification for solving these conservation equations is obtained by describing the vector field by potential functions using the Helmholtz decomposition. Here the potentials related to the divergence and rotation are separated into two separate terms. Both terms yield a Poisson equation for solving the potential functions, and once obtained, these give access to the induced vector field.

Classical particle systems are discrete systems where a finite number of particles each represent a physical object such as a planet or a molecule. The particles carry an intrinsic quantity e.g. mass or electrical charge which interacts with the potential field resulting in forces on the particle. Through this interaction the solution of Poisson's equation describes the potential energy and directly governs the dynamics of the system following a given initial state.

The discrete particle system may be extended in a more abstract mathematical manner to numerically approximate a continuum field such as a fluid (Cottet and Koumoutsakos, 2000; Koumoutsakos, 2005). This is done by regularising the intrinsic quantity of the particle which now may represent a more abstract property of the field (such as dilation or vorticity in the case of fluids). In mathematics the term *regularisation* refers to introducing additional information implicitly to amend an ill-posed problem. In this case the regularisation will consist of replacing the singular point particles with particles of a pre-defined spherical symmetric distribution of a characteristic radius. In this way a dense cloud of particles may represent a discretised approximation to a continuum field by using a regularisation radius that is greater than the spacing between the particles as elaborated in Fig. 1. This regularised extension is most useful in numerical simulations where a discretised system is indeed needed to solve the governing equations using computers. Here the particles are viewed as the computational points of the numerical discretisation and the particle regularisation then corresponds to the smoothness of the field, which in turn is obtained by super-position of the regularised particle quantities.

The class of numerical techniques that uses discrete particles to simulate a vast range of systems, of both discrete and continuous nature is called *particle methods*. The methods have been extensively applied and validated in the past three decades, see e.g. the references (Hockney and Eastwood, 1988; Cottet and Koumoutsakos, 2000; Griebel et al., 2007). Most particle methods provide a solution to Poisson's equation by using Green's functions (e.g. the Biot-Savart law or the Coulomb law) where each particle in principle interacts with every other particle in the system. The direct evaluation of the mutual particle interaction is an N_p-body problem where the computational complexity scales as $\mathcal{O}(N_p^2)$ – a scaling which at this point in computational

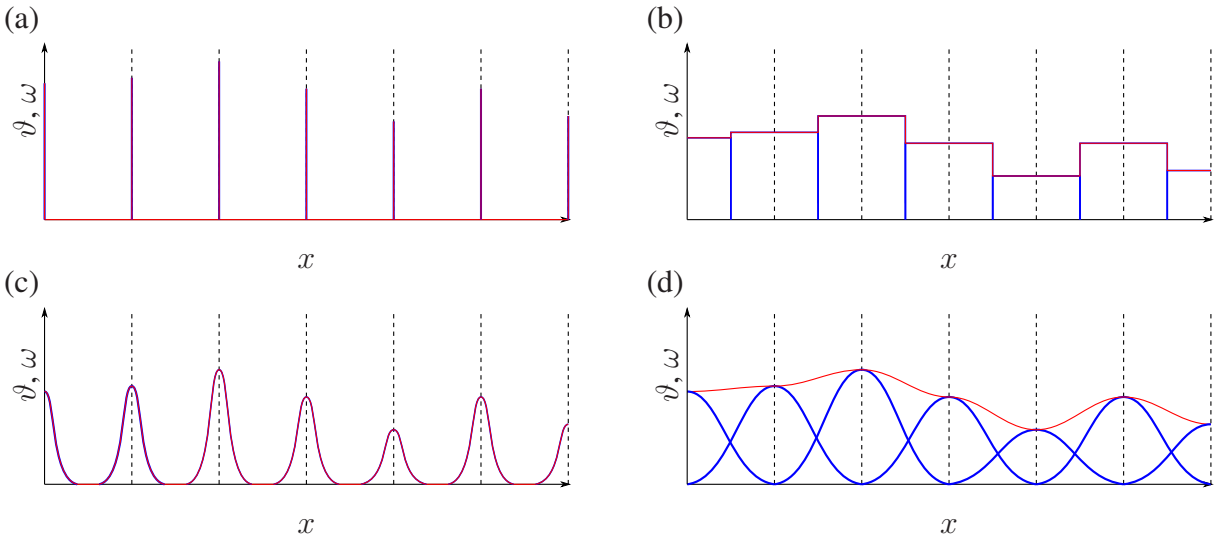

Figure 1: A sketch of different regularised discrete particles and their super-positioned field. The dashed lines indicates the position of the particles (here uniformly spaced), the blue lines the individual distribution of the particle density and the red line represents the super-positioned density field. (a) singular particles (b) uniformly distributed particles (c) Non-overlapping Gaussian distributions (d) Overlapping Gaussian distributions. It is thus seen that overlapping distributions are needed for the super-positioned field to be coherent and differentiable.

technology makes large simulations ($N_p \gg \mathcal{O}(10^4)$) computationally infeasible. On this ground more computationally effective methods have to be employed in order to simulate large particle systems.

For simulating strict free-space boundary conditions there are two widely used methods, both based essentially on the same principle. The main principle is to merge the particles into a new set of data-points which conserves a desired number of moments of the original particles and furthermore offers a favourable data-structure for a more effective evaluation of the interaction.

The first method is the multipole methods such as the fast multipole method (FMM) (Carrier et al., 1988) based on tree algorithms (Barnes and Hut, 1986). In multipole methods data merging is prioritised in order to reduce the number of interactions needed and is performed by constructing high order multipole expansions of the particles. The longer distance from the particle of interest, the more interacting particles can be merged into one single multipole interaction which in turn requires a higher order multipole expansions in order to maintain its accuracy. For the nearby interactions the multipole methods uses a particle-particle interaction by which the method is not restricted by a minimum interaction length and can be used to evaluate the interaction of singular particles. The FMM is capable of achieving an optimal scaling of $\mathcal{O}(N_p)$ (Carrier et al., 1988), however it is subject to a large pre-factor when constructing and traversing the data tree structure. This reduces the efficiency of the FMM and makes it less attractive, particularly for three dimensional simulations where the calculation of multipole expansions also becomes significantly more expensive due to the increasing number of moments that needs to be conserved for each dimension.

The second method is the particle-mesh method. Here moment-conserving schemes are used to interpolate the particle quantities to structured data-points of a uniform mesh. The interpola-

tion can be viewed as the counterpart to calculating the multipoles in multipole methods. The number of new data-points in the particle-mesh method is however not reduced significantly but the equispaced structure of the data-points enables the use of fast recursive algorithms such as the Fast Fourier transform (FFT). Given optimal conditions, the particle-mesh method has the capability of scaling as $\mathcal{O}(dN^d \log(N))$ on a square/cubic domain where N is the number of grid points in each direction, and d is the number of dimensions.

Evidently, using a mesh to calculate the particle interactions prevents any interactions at lengths shorter than the mesh cell length. However a nearby particle-particle correction scheme can be applied to recover contribution from the lost short-range interaction potential. This method is known as the particle-particle particle-mesh method (P^3M) (Hockney and Eastwood, 1988; Walther, 2003; Luty and van Gunsteren, 1996) and strongly resembles the particle-particle interaction of the nearby particles in the FMM.

The primary challenge in FFT-based solvers is to obtain non-periodic boundary conditions. A method of obtaining the free-space boundary conditions is proposed by (Hockney and Eastwood, 1988) and is widely used in the field of particle-mesh methods. The method uses a Green's function convolution that is made efficient by applying the FFT algorithm where the periodicity is avoided by zero-padding the domain.

This method may be extended to obtain mixed periodic and free-space boundary conditions. A naive approach is to use the method of repeating domains where the free-space Green's function is directly corrected to implicitly account for a specified number of repeated fields and thus obtain pseudo-periodic boundaries (Cottet and Koumoutsakos, 2000). The method converges with the number of repeated domains to first order and thus requires a large number of repeated domains to reduce the error significantly. A more formal approach to achieve mixed periodic and free-space boundary conditions was proposed by (Chatelain and Koumoutsakos, 2010). Here the Poisson equation was solved directly in the periodic directions yielding a modified Helmholtz equation for the free-space directions which in turn is solved by deriving the appropriate Green's functions.

As mentioned above, the length of the mesh cells is related to the spacing between the particles in the particle-mesh method. Hence for many particle systems where particles tend to condense in local regions (e.g. galaxies in astrophysics or the vortex structures of fluid dynamics) the method may increase its computational efficiency by applying a localised mesh refinement scheme here referred to as *multi-resolution* methods. Several multi-resolution methods have been implemented in particle-mesh simulation for astrophysics (Villumsen, 1989) and represents the state-of-the-art vortex methods (Bergdorf et al., 2005; Bergdorf and Koumoutsakos, 2006; El Ossmani and Poncet, 2010; Rasmussen et al., 2011).

Previous implementations of the particle-mesh method has not included a regularisation of the Green's function as the minimum interaction length enforced by the mesh prevents singular interactions which may cause a numerical instability of the method. Regularisation is thus not needed to maintain the numerical instability of the method, however as will be shown in this monograph the absence of regularisation limits the convergence rate of the solver for problems including either full or partial free-space boundary conditions.

In this monograph the FFT-based Poisson solver of the particle-mesh method is extended to achieve an increased order of convergence by formulating and applying regularised Green's functions. This extension is based on the work of (Leonard, 1980; Beale and Majda, 1985; Perlman, 1985; Hald, 1987; Winckelmans and Leonard, 1993) who uses regularised particles for

mesh free particle interactions to avoid the sensitivity of singular interactions towards numerical instability in vortex methods. The approach of this monograph is however different than the conventional approach (Leonard, 1980; Beale and Majda, 1985; Perlman, 1985; Hald, 1987; Winckelmans and Leonard, 1993) as the regularisation will be viewed and derived from arguments based on the problem transformed into Fourier space. Using this approach it is shown that the problem is simplified for identifying approximative errors and the choice of regularisation parameters becomes more evident. Attention is primarily on the free-space boundary conditions however an example of the regularised extension to mixed periodic and free-space boundary conditions is also provided.

A novel method of achieving a multi-resolution solver is also presented by combining the idea of particle-particle correction from the P^3M method with the regularisation method. Here a number of local refinement patches are used to retrieve a the solution at a higher band of wave-numbers after which the super-position principle is used to obtain the full solution. The multi-resolution implementation is shown to maintain a high order converging solution for different configurations of the refinement patches.

For a full implementation of the presented regularised Poisson solver in a particle-mesh based method, the reader is referred to Part II of this dissertation. Regarding a full implementation of the multi-resolution method in a particle-mesh method the reader is referred to the approach of (Rasmussen et al., 2011) in terms of combining a mesh-based Poisson solver and particles in a multi-resolution implementation using local refinement patches.

Chapter 1

The Poisson equation and its solution using regularised Green's functions

1.1 The homogeneous solution to the Poisson equation in unbounded domains

For a given vector field $\boldsymbol{v}$ which has at least two continuous derivatives (i.e. $\boldsymbol{v} \in C^2$) we may use the Helmholtz decomposition to describe the field in terms of potential functions:

$$\boldsymbol{v}(\boldsymbol{x}) = \boldsymbol{\nabla} \times \boldsymbol{\psi}(\boldsymbol{x}) - \boldsymbol{\nabla}\phi(\boldsymbol{x}) \qquad \text{where} \qquad \boldsymbol{\nabla} \cdot \boldsymbol{\psi}(\boldsymbol{x}) = 0 \tag{1-1}$$

Here the first term consists of the curl of a vector potential and thus represents the divergence-free part of $\boldsymbol{v}$. The second term is the gradient of a scalar function and thus gives the irrotational part of $\boldsymbol{v}$. The added constraint of the divergence-free vector potential (i.e. $\boldsymbol{\nabla} \cdot \boldsymbol{\psi}(\boldsymbol{x}) = 0$) is essential for the decomposition to be unique as the decomposition replaces the three components of $\boldsymbol{v}$ with the total four components of the vector and scalar potential combined.

As mentioned in the introduction the fundamental operations describing the conservation of the flux and circulation of the vector field $\boldsymbol{v}$ is the divergence $\vartheta(\boldsymbol{x}) = \boldsymbol{\nabla} \cdot \boldsymbol{v}(\boldsymbol{x})$ and the curl $\boldsymbol{\omega}(\boldsymbol{x}) = \boldsymbol{\nabla} \times \boldsymbol{v}(\boldsymbol{x})$, respectively. From the Helmholtz decompositions it follows that these may be expressed by the potential functions as:

$$\vartheta(\boldsymbol{x}) = -\boldsymbol{\nabla}^2\phi(\boldsymbol{x}) \qquad \text{and} \qquad \boldsymbol{\omega}(\boldsymbol{x}) = -\boldsymbol{\nabla}^2\boldsymbol{\psi}(\boldsymbol{x}) \tag{1-2}$$

As seen both potentials may thus be obtained by solving the Poisson equation. By utilising the linearity of the Poisson equation and considering the equations by their Fourier transform we get:

$$\begin{aligned} -k^2\,\widehat{\phi}(\boldsymbol{k}) &= -\widehat{\vartheta}(\boldsymbol{k}) \\ -k^2\,\widehat{\boldsymbol{\psi}}(\boldsymbol{k}) &= -\widehat{\boldsymbol{\omega}}(\boldsymbol{k}) \end{aligned} \quad \Rightarrow \quad \begin{aligned} \widehat{\phi}(\boldsymbol{k}) &= \frac{\widehat{\vartheta}(\boldsymbol{k})}{k^2} \\ \widehat{\boldsymbol{\psi}}(\boldsymbol{k}) &= \frac{\widehat{\boldsymbol{\omega}}(\boldsymbol{k})}{k^2} \end{aligned} \tag{1-3}$$

Here the $\widehat{\cdot}$ denotes a full or partial Fourier transformed variable where $\boldsymbol{k} = (k_x, k_y, k_z)$ is the angular wave-number of the Fourier space and:

$$k^2 = \begin{cases} k_x^2 & \text{in 1D} \\ k_x^2 + k_y^2 & \text{in 2D} \\ k_x^2 + k_y^2 + k_z^2 & \text{in 3D} \end{cases} \tag{1-4}$$

The unbounded Fourier transform and its inverse transform of a function $A(\boldsymbol{x})$ are formally given by:

$$\widehat{A}(\boldsymbol{k}) = \int_{-\infty}^{\infty} A(\boldsymbol{x})\, e^{-\imath\, \boldsymbol{k}\, \boldsymbol{x}}\, d\boldsymbol{x} \qquad \text{and} \qquad A(\boldsymbol{x}) = \frac{1}{2\pi} \int_{-\infty}^{\infty} \widehat{A}(\boldsymbol{k})\, e^{\imath\, \boldsymbol{k}\, \boldsymbol{x}}\, d\boldsymbol{k} \tag{1-5}$$

where ι is the imaginary unit. The unbounded integrals of the transforms are however not always feasible as we in practise only can integrate a bounded interval given an arbitrary field. The Fourier transform of the vector field divergence and curl (i.e. the right-hand-sides of the Poisson equations) are nonetheless obtained without great difficulties as these are typically bounded in the real space. The inverse transforms, which we need in order to recover the solution in the real space, may pose some difficulties which compromises the solution of the Poisson equations. For periodic boundary conditions we in fact do have a bounded interval by which we can calculate the inverse Fourier transform directly to the precision of the Fourier transform which depends on the number of continuous derivatives of the field (Körner, 1988). However for free-space boundary condition the integral of the inverse Fourier transform is unbounded and other methods must thus be applied in order to get an accurate solution. A simple way to overcome this is the expanding domain method (Anderson, 2014). Here the integral boundaries are expanded in order to reduce the error of the finite integral approximation albeit at an additional computational cost and limited convergence rate of the solution.

Another approach is to define Green's functions. Here the homogeneous solution with appropriate boundary conditions (i.e. the Green's function) is derived analytically and the particular solution is then found by convolving the Green's function with the right-hand-side of the Poisson equation. In other terms we may invert the Poisson equation by convolving with a Green's function G and utilise the commutative properties of the convolution operation with respect to differentiation:

$$\begin{aligned} G(\boldsymbol{r}) * \boldsymbol{\nabla}^2\phi(\boldsymbol{x}) &= -G(\boldsymbol{r}) * \vartheta(\boldsymbol{x}) \\ G(\boldsymbol{r}) * \boldsymbol{\nabla}^2\boldsymbol{\psi}(\boldsymbol{x}) &= -G(\boldsymbol{r}) * \boldsymbol{\omega}(\boldsymbol{x}) \end{aligned} \quad \Rightarrow \quad \begin{aligned} \boldsymbol{\nabla}^2 G(\boldsymbol{r}) * \phi(\boldsymbol{x}) &= -G(\boldsymbol{r}) * \vartheta(\boldsymbol{x}) \\ \boldsymbol{\nabla}^2 G(\boldsymbol{r}) * \boldsymbol{\psi}(\boldsymbol{x}) &= -G(\boldsymbol{r}) * \boldsymbol{\omega}(\boldsymbol{x}) \end{aligned} \tag{1-6}$$

Here $\boldsymbol{r} = \boldsymbol{x} - \boldsymbol{x}'$ and $*$ denotes the linear convolution:

$$A(\boldsymbol{r}) * B(\boldsymbol{x}) = \int_{-\infty}^{\infty} A(\boldsymbol{x} - \boldsymbol{x}')\, B(\boldsymbol{x}')\, d\boldsymbol{x}' \tag{1-7}$$

Hence by defining the Laplacian of the Green's function as the Dirac delta function the potential functions $\phi(\boldsymbol{x})$ and $\boldsymbol{\psi}(\boldsymbol{x})$ are obtained by:

$$\phi(\boldsymbol{x}) = G(\boldsymbol{r}) * \vartheta(\boldsymbol{x}) \quad \text{and} \quad \boldsymbol{\psi}(\boldsymbol{x}) = G(\boldsymbol{r}) * \boldsymbol{\omega}(\boldsymbol{x}) \tag{1-8}$$

where:

$$\boldsymbol{\nabla}^2 G(\boldsymbol{r}) = -\delta(\boldsymbol{r}) \tag{1-9}$$

is the equation that we have to solve in order to obtain the Green's function which represents the homogeneous solution for $\boldsymbol{r} \neq \boldsymbol{0}$. In Fourier space the homogeneous solution becomes:

$$-k^2\, \widehat{G}(k) = -1 \quad \Rightarrow \quad \widehat{G}(k) = \frac{1}{k^2} \tag{1-10}$$

Here we formally define $\widehat{G}(0) = 0$ as this value represents the average value of the solution which for potential functions is arbitrary due to an invariance of the vector field. It is noted that in order to represent the homogeneous solution (associated with the delta function) an infinite domain is needed in Fourier space as the right-hand-side $(1/k^2)$ is in fact unbounded. Hence for free-space boundary conditions we must thus derive the Green's function analytically from

the unbounded inverse Fourier transform. The unbounded inverse Fourier transform yields the Green's function in real space which for 1D yields:

$$G(x) = \frac{1}{2\pi}\int_{-\infty}^{\infty} \frac{1}{k_x^2 + k_y^2}\, e^{\iota\, k_x\, x}\, dk_x \tag{1-11}$$

for 2D:

$$G(x,y) = \frac{1}{2\pi}\int_{-\infty}^{\infty} \left(\frac{1}{2\pi}\int_{-\infty}^{\infty} \frac{1}{k_x^2 + k_y^2}\, e^{\iota\, k_x\, x}\, dk_x\right)\, e^{\iota\, k_y\, y}\, dk_y \tag{1-12}$$

and for 3D:

$$G(x,y,z) = \frac{1}{2\pi}\int_{-\infty}^{\infty} \left(\frac{1}{2\pi}\int_{-\infty}^{\infty} \left(\frac{1}{2\pi}\int_{-\infty}^{\infty} \frac{1}{k_x^2 + k_y^2 + k_z^2}\, e^{\iota\, k_x\, x}\, dk_x\right)\, e^{\iota\, k_y\, y}\, dk_y\right)\, e^{\iota\, k_z\, z}\, dk_z \tag{1-13}$$

Transformed to d-dimensional spherical/polar coordinates this becomes:

$$G(r) = \frac{1}{(2\pi)^{\frac{d}{2}}}\int_0^{\infty} \frac{1}{k^2}\, \frac{J_{\frac{d}{2}-1}(k\,r)}{(k\,r)^{\frac{d}{2}-1}} k^{d-1}\, dk = \frac{1}{(2\pi)^{\frac{d}{2}} r^{\frac{d}{2}-1}}\int_0^{\infty} J_{\frac{d}{2}-1}(k\,r)\, k^{d/2-2}\, dk \tag{1-14}$$

Here J_μ is the Bessel function of first kind and r denotes the modulus i.e. $r = |\boldsymbol{r}| = |\boldsymbol{x} - \boldsymbol{x}'|$.

By analysing the exponential behaviour we find, that for the integral to converge for $k \to \infty$ the integrand must decay as k^p where $p < -1$. For $n \geq -1$ the integral diverges for $k \to \infty$ and the unbounded inverse Fourier transform cannot be determined. As the Bessel function decays as $k^{-1/2}$ for $k \to \infty$ we may evaluate the integrand by summing the exponents for which we have that:

$$p = \frac{d}{2} - 2 - \frac{1}{2} = \frac{d}{2} - \frac{5}{2} < -1 \qquad \text{by which} \qquad d < 3 \tag{1-15}$$

This answer seems to exclude a solution for $d = 3$. However the integrand for $d = 3$ yields the *sinc* function whose integral indeed convergences asymptotically towards a finite value and is known as the Dirichlet integral. Hence we can in fact determine the Green's function for $d = 3$:

$$G(r) = \frac{1}{2\pi^2\, r}\int_0^{\infty} \frac{\sin(k\,r)}{k}\, dk = \frac{1}{4\pi\, r} \qquad \text{as} \qquad \int_0^{\infty} \frac{\sin(k\,r)}{k}\, dk = \frac{\pi}{2} \tag{1-16}$$

Additionally we need the integral to be finite for $k \to 0$. This requires that the integrand is proportional to k^p where $p > -1$. For $p \leq -1$ the integrand is singular for $k \to 0$. As the Bessel function is proportional to $k^{d/2-1}$ for $k \to 0$ we have the exponential behaviour:

$$p = \frac{d}{2} - 2 + \frac{d}{2} - 1 = d - 3 > -1 \qquad \text{by which} \qquad 2 < d \tag{1-17}$$

Hence for dimension $d = 2$ the integral is not finite. However, we may apply some mathematical ingenuity to circumvent this restriction by using the Leibniz integration rule to define dG/dr which then can be integrated with respect to r. For $d = 2$ we have:

$$\frac{d}{dr}G(r) = \frac{1}{2\pi}\frac{d}{dr}\left(\int_0^{\infty} \frac{J_0(k\,r)}{k}\, dk\right) = \frac{1}{2\pi}\int_0^{\infty} \frac{1}{k}\frac{d}{dr}\left(J_0(k\,r)\right)\, dk = \frac{1}{2\pi\, r} \tag{1-18}$$

by which:

$$G(r) = -\frac{1}{2\pi}\ln(r) \tag{1-19}$$

Here we have used that:

$$\frac{d}{dr}J_0(k\,r) = k\,J_{-1}(k\,r) = -k\,J_1(k\,r) \qquad \text{and} \qquad \int_0^\infty J_1(k\,r)\,dk = \frac{1}{r} \tag{1-20}$$

The respective Green's functions for 2D and 3D thus becomes:

$$G(\boldsymbol{r}) = \begin{cases} -\dfrac{1}{2\pi}\ln(r) & \text{in 2D,} \\ \dfrac{1}{4\pi\,r} & \text{in 3D.} \end{cases} \qquad \text{where} \qquad r > 0 \tag{1-21}$$

To obtain the vector field $\boldsymbol{v}$ of the Helmholtz decomposition the gradient of the potential functions are needed. The corresponding Green's functions for the gradient $\boldsymbol{K}(\boldsymbol{r}) = \boldsymbol{\nabla} G(\boldsymbol{r})$ by which $\boldsymbol{K}(\boldsymbol{r}) = \dfrac{d}{dr}G(r)\,\boldsymbol{e}_r$ are given by:

$$\boldsymbol{K}(\boldsymbol{r}) = \begin{cases} -\dfrac{1}{2\pi\,r}\boldsymbol{e}_r & \text{in 2D,} \\ -\dfrac{1}{4\pi\,r^2}\boldsymbol{e}_r & \text{in 3D,} \end{cases} \qquad \text{where} \qquad r > 0 \tag{1-22}$$

Here $\boldsymbol{e}_r = \boldsymbol{r}/r$ is the radial unit normal vector. It is here noted that the $\boldsymbol{K}(\boldsymbol{r})$ functions of 2D and 3D corresponds to the well-known inverse square law which form the basis of the Biot-Savart and Coulomb's law.

1.2 The homogeneous solution to the Poisson equation in domains with mixed periodic and free-space boundary conditions

For mixed periodic and free-space boundary conditions we obtain the Green's function by defining the inverse Fourier transform with different integration bounds for the periodic and the free-space directions.

1.2.1 Mixed periodic and free-space boundary condition in 2D

For the 2D case with one periodic (in this case the y-direction) and one free-space (in this case the x-direction) boundary conditions we get:

$$G(x,y) = \frac{1}{2\pi}\int_{-k_s/2}^{k_s/2}\left(\frac{1}{2\pi}\int_{-\infty}^{\infty}\frac{1}{k_x^2+k_y^2}\,e^{\iota\,k_x\,x}\,dk_x\right)\,e^{\iota\,k_y\,y}\,dk_y \tag{1-23}$$

Here k_s is the maximum angular wave-number which is determined by the extent of the domain in the periodic direction. The bounded interval of the periodic direction is easily calculated by

regular Fourier transforms after which we are left with a Green's function in mixed real and Fourier space. Hence we need to determine the integral:

$$\widehat{G}(x, k_y) = \frac{1}{2\pi} \int_{-\infty}^{\infty} \frac{1}{k_x^2 + k_y^2} \, e^{\iota \, k_x \, x} \, dk_x \tag{1-24}$$

Here it is noticed that for $k_y \neq 0$ the divergence of the integral when $k_x \to 0$ is conveniently avoided and for the case of $k_y = 0$ we once again can define the Green's function arbitrarily as it represents the average value of the solution which for a potential is arbitrarily defined. Using a 1D radial (i.e. even) inverse Fourier transform (where $r = |x|$ and $k = k_x$) we get the Green's function for mixed boundary conditions:

$$\widehat{G}(r, k_y) = \frac{1}{\pi} \int_0^{\infty} \frac{\cos(k\, r)}{k^2 + k_y^2} \, dk = \frac{1}{2} \frac{\exp(-|k_y|\, r)}{|k_y|} \tag{1-25}$$

This Greens functions is similar to that proposed in (Chatelain and Koumoutsakos, 2010).

1.2.2 Mixed boundary conditions in 3D case with one free-space direction

The result of the 2D case may be extended to the 3D case with two periodic (in this case the y and z-directions) and one free-space (in this case the x-direction) boundaries. The Green's function which now is initially transformed and implicitly solved in the y and z-direction becomes:

$$\widehat{G}(r, k_y, k_z) = \frac{1}{\pi} \int_0^{\infty} \frac{\cos(k\, r)}{k^2 + k_y^2 + k_z^2} \, dk = \frac{1}{2} \frac{\exp\left(-\sqrt{k_y^2 + k_z^2}\, r\right)}{\sqrt{k_y^2 + k_z^2}} \tag{1-26}$$

1.2.3 Mixed boundary conditions in 3D case with two free-space direction

For the 3D case with one periodic (in this case the z-direction) and two free-space (in this case the x and y-directions) boundaries the Green's function is initially transformed and implicitly solved in the z-direction after which we have:

$$\widehat{G}(x, y, k_z) = \frac{1}{2\pi} \int_{-\infty}^{\infty} \left(\frac{1}{2\pi} \int_{-\infty}^{\infty} \frac{1}{k_x^2 + k_y^2 + k_z^2} \, e^{\iota \, k_x \, x} \, dk_x \right) \, e^{\iota \, k_y \, y} \, dk_y \tag{1-27}$$

Switching to a 2D radial inverse Fourier transform (where $r = \sqrt{x^2 + y^2}$ and $k = \sqrt{k_x^2 + k_y^2}$) we have:

$$\widehat{G}(r, k_z) = \frac{1}{2\pi} \int_0^{\infty} \frac{k}{k^2 + k_z^2} \, J_0(k\, r) \, dk = \frac{1}{2\pi} K_0(r\, |k_z|) \tag{1-28}$$

Again we obtain a Greens functions which is equivalent to that proposed by (Chatelain and Koumoutsakos, 2010).

1.3 The homogeneous solution to the Poisson equation using a discretised approximation with high order regularisation

The discrete equivalent to the field quantities are obtained by defining a set of N discrete points $\boldsymbol{x}_i$ where $i = \{0, 1, ..., N-1\}$. The points are assigned the field values ϑ_i and $\boldsymbol{\omega}_i$ such that the approximated continuous field values $\vartheta(\boldsymbol{x})$ and $\boldsymbol{\omega}(\boldsymbol{x})$ become:

$$\vartheta(\boldsymbol{x}) = \sum_{i=0}^{N-1} \zeta(\boldsymbol{x} - \boldsymbol{x}_i)\, \vartheta_i \quad \text{and} \quad \boldsymbol{\omega}(\boldsymbol{x}) = \sum_{i=0}^{N-1} \zeta(\boldsymbol{x} - \boldsymbol{x}_i)\, \boldsymbol{\omega}_i \tag{1-29}$$

Here ζ is a regularisation function which represents the density distribution of the discrete element. Using this representation the convolution equations takes the semi-discrete form:

$$\phi(\boldsymbol{x}) = \sum_{i=1}^{N} G(\boldsymbol{x} - \boldsymbol{x}_i)\ \vartheta_i \qquad \text{and} \qquad \boldsymbol{\psi}(\boldsymbol{x}) = \sum_{i=1}^{N} G(\boldsymbol{x} - \boldsymbol{x}_i)\ \boldsymbol{\omega}_i \tag{1-30}$$

and the regularised homogeneous equation now takes the form:

$$\boldsymbol{\nabla}^2 G(\boldsymbol{x} - \boldsymbol{x}_i) = -\zeta(\boldsymbol{x} - \boldsymbol{x}_i) \tag{1-31}$$

It is here noted that the singular particle system is obtained if the regularisation function is equal to the Dirac delta function i.e. $\zeta(\boldsymbol{x} - \boldsymbol{x}_i) = \delta(\boldsymbol{x} - \boldsymbol{x}_i)$ which in turn results in a singular Green's function as seen in Sec. 1.1. This result is evident from the perspective that containing a quantity in a infinitesimal small point results in an infinite density of that quantity.

For a discrete approximation used in numerical simulations singularities cannot be handled in Fourier space. Due to the discretisation of the domain in the physical space $\boldsymbol{x}_i$, the Fourier space, represented by the wave-numbers $k_i = \{-k_s/2, ..., k_s/2\}$, is bounded and can therefore only approximate a singularity by a finite estimation. Here $k_s = 2\pi/h$ is the angular sampling wave-number corresponding to the discrete mesh cell length h and $k_s/2$ is the highest resolved angular wave-number due to the Nyquist-Shannon sampling theorem. Attempts of defining a finite value to replace the singularity $G(\mathbf{0})$ have been presented in (Hockney and Eastwood, 1988; Chatelain and Koumoutsakos, 2010; Rasmussen, 2011) however no better than a convergence rate of $\mathcal{O}(h^2)$ has been achieved.

A method to achieve a higher order convergence rate is to use a spectrally compact regularisation function which makes the integral of the inverse Fourier transform convergent. Hence is the regularisation function must fulfil:

$$\widehat{\zeta}(k) = 1 \quad \text{for} \quad k = 0 \qquad \text{and} \qquad \widehat{\zeta}(k) = 0 \quad \text{for} \quad k \geq k_s/2 \tag{1-32}$$

The order is increased to an m-th order regularisation by nullifying the $m-2$ order derivatives of the spectral function at $k = 0$. This is equal to conserving the higher order moments in real space. This is summarised by the following additional requirements:

$$\left.\frac{d^\beta \widehat{\zeta}}{dk^\beta}\right|_{k=0} = \int_{-\infty}^{\infty} r^\beta\, \zeta(r)\, d\boldsymbol{x} = 0^\beta \quad \text{for} \quad \beta = \{0, 2, ..., m-2\} \tag{1-33}$$

We note that m is an even number since the moments for odd integers of β are automatically satisfied due to the radial symmetry of the function.

The regularised Green's functions for the Poisson equation with free-space boundary conditions may thus be found by the inverse Fourier transforms:

$$G(r) = \begin{cases} \dfrac{1}{2\pi}\displaystyle\int_0^\infty \widehat{\zeta}(k)\,\frac{J_0(k\,r)}{k}\,dk & \text{for 2D} \\ \dfrac{1}{2\pi^2}\displaystyle\int_0^\infty \widehat{\zeta}(k)\frac{\sin{(k\,r)}}{k\,r}\,dk & \text{for 3D} \end{cases} \tag{1-34}$$

Using integration by parts and the Leibniz integration rule we may re-write these as:

$$G(r) = \begin{cases} \dfrac{1}{2\pi}\displaystyle\int\int_0^\infty \widehat{\zeta}(k)\,J_1(kr)\,dk\,dr & \text{for 2D} \\ \dfrac{1}{2\pi^2}\displaystyle\int_0^\infty \frac{\mathrm{Si}(k\,r)}{r}\,\frac{d\widehat{\zeta}}{dk}\,dk & \text{for 3D} \end{cases} \tag{1-35}$$

and for the Green's functions of the gradient $\boldsymbol{K}(\boldsymbol{r}) = \dfrac{d}{dr}G(r)\,\boldsymbol{e}_r$ we get:

$$\boldsymbol{K}(r) = \begin{cases} \dfrac{1}{2\pi}\displaystyle\int_0^\infty \widehat{\zeta}(k)\,J_1(kr)\,dk\,\boldsymbol{e}_r & \text{for 2D} \\ \dfrac{1}{2\pi^2}\displaystyle\int_0^\infty \frac{d}{dr}\left(\frac{\mathrm{Si}(k\,r)}{r}\right)\,\frac{d\widehat{\zeta}}{dk}\,dk\,\boldsymbol{e}_r & \text{for 3D} \end{cases} \tag{1-36}$$

Here $\mathrm{Si}(k\,r) = \displaystyle\int_0^{k\,r} \frac{\sin{(q)}}{q}\,dq$.

1.3.1 Regularisation by Gaussian smoothing for unbounded domains

One method of regularisation is obtained by Gaussian smoothing. For this, the regularisation is given by the Gauss function whose Fourier representation is given by:

$$\widehat{\zeta}(s) = \exp\left(-\frac{s^2}{2}\right) \tag{1-37}$$

Here $s = k\,\sigma$ is the angular wave-number normalized with σ, which in this case represents a smoothing radius. In respect to Eq. (1-33) it is seen that the Gauss function only satisfies the 0-th moment and thus gives a second order regularisation.

One approach to obtain a high order Gaussian regularisation ζ_m of order m is by performing an approximate deconvolution on the low order regularisation function which effectively conserves higher order moments of the original field. A high order regularisation function can thus be obtained from a low order regularisation by:

$$\widehat{\zeta}_m(s) = D_m\,\widehat{\zeta}(s) \tag{1-38}$$

Here D_m is an m-th order approximation of the inverse regularisation function. To find D_m, the Taylor expansion of the inverse Gauss function is used:

$$D_\infty = \left(\exp\left(-\frac{s^2}{2}\right)\right)^{-1} = 1 + \frac{1}{2}s^2 + \frac{1}{8}s^4 + \frac{1}{48}s^6 + ... = \sum_{n=0}^{\infty} \frac{(s^2/2)^n}{n!} \tag{1-39}$$

An m-th order deconvolution function is thus obtained by the truncated series by which an m-th order Gaussian regularisation function is given by:

$$\widehat{\zeta}_m(s) = \sum_{n=0}^{m/2-1} \frac{(s^2/2)^n}{n!} \exp\left(-\frac{s^2}{2}\right) \tag{1-40}$$

The regularisation functions for $m = \{2, 4, 6, 8, 10\}$ are shown in Fig. 1.1 for both Fourier and real space. It is seen as the order of the regularisation is increased, the bandwidth in the Fourier space increases, and manifests in real space as oscillations of the regularisation function which is needed for the conservation of higher order moments. It should here be mentioned that the oscillatory behaviour of the high order regularisation function may formally violate constraints of the simulated physics as the density obtains negative values in the close vicinity of the particle. An example of such violation is a gravitational system where the intrinsic particle value is its mass by which negative values in the regularisation function formally represent a negative mass density which indeed conflicts with the physics. However for most cases this conflict constitutes a mere theoretical formality and is sufficiently corrected when super-positioning the particles.

As the Gaussian regularisation functions are not formally bounded in Fourier space the constraint of Eq. (1-32) introduces an additional error. This restricts the choice of the smoothing radius σ which determines the extent of the Gaussian regularisation function and hence the error of the truncation at $k = k_s/2$. As k_s is proportional to $1/h$ and the extent of the Gaussian regularisation function in Fourier space is proportional to $1/\sigma$ the formal choice of smoothing radius is $\sigma = \alpha h$ where $\alpha = 2$. In this way the bounds of the Fourier space (i.e. $k_s/2$) and the extent of the Gaussian regularisation function scales equally resulting in a constant truncation error when varying h. It was shown in (Hejlesen et al., 2013) that choosing $\alpha < 2$ may result in the reduction of a high order method to a second order convergence rate. It is noted that that (Beale and Majda, 1982b,a, 1985) use a different choice of smoothing radius (i.e. $\sigma = h^\alpha$ with $0 < \alpha < 1$) however an apparent reason for this choice is not provided. However it is emphasized that the choice of smoothing radius is somewhat arbitrary and must only be proportional to h for the smoothing error to converge to zero. The formal choice of $\sigma = \alpha h$ with $\alpha = 2$ is thus only to ensure the convergence rate of the regularisation, however choosing $\alpha = 1.5$ has shown in (Hejlesen et al., 2013) to keep the convergence rate until the order of machine precision.

Inserting the high order Gaussian regularisation functions of Eq. (1-40) into the expression for the regularised Green's function Eq. (1-35) we see that the Gaussian regularised Green's functions G_m of order m takes the general form:

$$G_m(\rho) = \begin{cases} -\dfrac{1}{2\pi}\left(\ln(\sigma\,\rho) - P_m(\rho)\, \exp\left(-\dfrac{\rho^2}{2}\right) + \dfrac{1}{2}\,\mathrm{E}_1\left(\dfrac{\rho^2}{2}\right)\right) & \text{in 2D} \\ \dfrac{1}{4\pi\,\sigma\,\rho}\left(Q_m(\rho)\, \exp\left(-\dfrac{\rho^2}{2}\right) + \mathrm{erf}\left(\dfrac{\rho}{\sqrt{2}}\right)\right) & \text{in 3D} \end{cases} \tag{1-41}$$

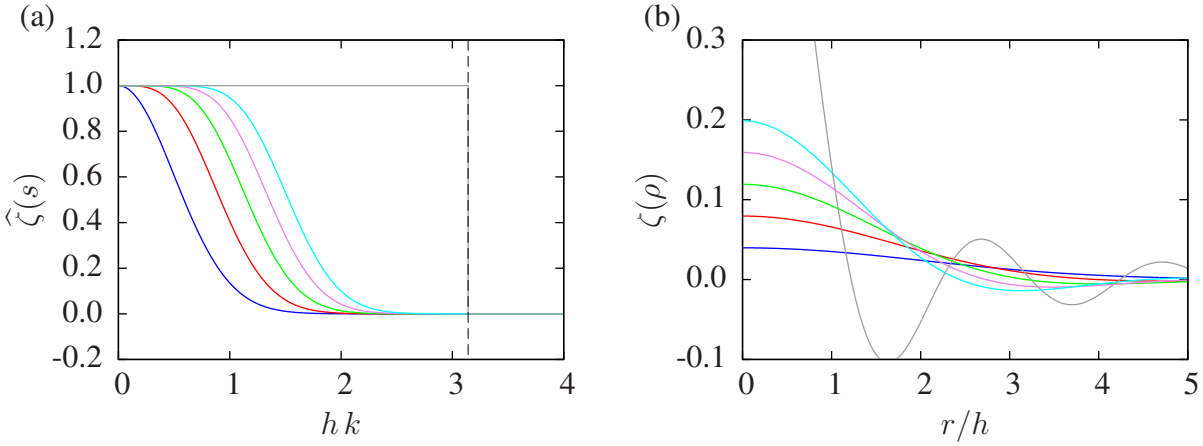

Figure 1.1: (a) The regularisation function in radial Fourier space and (b) the corresponding regularisation functions in 2D real space. The Gauss functions with $\sigma = 2h$ for $m = 2$: (——); $m = 4$: (——); $m = 6$: (——); $m = 8$: (——); $m = 10$: (——), and the Bessel function regularisation with $\sigma = h/\pi$: (——). The highest wave-number is indicated by: (– – – –)

where $\rho = r/\sigma$ is the normalised radial coordinate, $\mathrm{E}_1(z)$ is the first exponential integral function and $\mathrm{erf}(z)$ is the regular error function given by:

$$\mathrm{E}_1(z) = \int_1^\infty \frac{\exp(-zq)}{q}\,dq \qquad \text{and} \qquad \mathrm{erf}(z) = \frac{2}{\sqrt{\pi}}\int_0^z \exp\left(-q^2\right)\,dq \tag{1-42}$$

P_m is the resulting polynomials for the 2D function which for $m = \{2, 4, 6, 8, 10\}$ are:

$$\begin{aligned} P_2(\rho) &= 0 & P_8(\rho) &= \frac{11}{12} - \frac{7}{24}\rho^2 + \frac{1}{48}\rho^4 \\ P_4(\rho) &= \frac{1}{2} & P_{10}(\rho) &= \frac{25}{24} - \frac{23}{48}\rho^2 + \frac{13}{192}\rho^4 - \frac{1}{384}\rho^6 \\ P_6(\rho) &= \frac{3}{4} - \frac{1}{8}\rho^2 \end{aligned} \tag{1-43}$$

Q_m is the resulting polynomials for the 3D function which for $m = \{2, 4, 6, 8, 10\}$ are:

$$\begin{aligned} Q_2(\rho) &= 0 & Q_8(\rho) &= \frac{1}{\sqrt{2\pi}}\left(\frac{19}{8}\rho - \frac{2}{3}\rho^3 + \frac{1}{24}\rho^5\right) \\ Q_4(\rho) &= \frac{1}{\sqrt{2\pi}}(\rho) & Q_{10}(\rho) &= \frac{1}{\sqrt{2\pi}}\left(\frac{187}{64}\rho - \frac{233}{192}\rho^3 + \frac{29}{192}\rho^5 - \frac{1}{192}\rho^7\right) \\ Q_6(\rho) &= \frac{1}{\sqrt{2\pi}}\left(\frac{7}{4}\rho - \frac{1}{4}\rho^3\right) \end{aligned} \tag{1-44}$$

In order to define $G_m(\mathbf{0})$ the exponential integral function $\mathrm{E}_1(z)$ can be expanded to an infinite series (Abramowitz and Stegun, 1972) by:

$$\mathrm{E}_1(z) = -\gamma - \ln(z) - \sum_{n=1}^{\infty}\frac{(-1)^n z^n}{n n!}, \tag{1-45}$$

where $\gamma = 0.5772156649$ is Euler's constant. The finite value of $G_m(\mathbf{0})$ is now defined as:

$$G_m(0) = \lim_{\rho\to 0}(G_m) = \begin{cases} \dfrac{1}{2\pi}\left(\dfrac{\gamma}{2} - \ln\left(\sqrt{2}\sigma\right) + Q_m(0)\right) & \text{in 2D} \\ \dfrac{\sqrt{2}}{8\pi^{3/2}\sigma}\left(\dfrac{R_m(\rho)}{\rho}\right)_{r=0} + \dfrac{\sqrt{2}}{4\pi^{3/2}\sigma} & \text{in 3D} \end{cases} \tag{1-46}$$

For $m = \{2, 4, 6, 8, 10\}$ we get the values for the 2D function:

$$\begin{aligned} G_2(0) &= \frac{1}{2\pi}\left(\frac{\gamma}{2} - \log\left(\sqrt{2}\sigma\right)\right) & G_8(0) &= \frac{1}{2\pi}\left(\frac{\gamma}{2} - \log\left(\sqrt{2}\sigma\right) + \frac{11}{12}\right) \\ G_4(0) &= \frac{1}{2\pi}\left(\frac{\gamma}{2} - \log\left(\sqrt{2}\sigma\right) + \frac{1}{2}\right) & G_{10}(0) &= \frac{1}{2\pi}\left(\frac{\gamma}{2} - \log\left(\sqrt{2}\sigma\right) + \frac{25}{24}\right) \\ G_6(0) &= \frac{1}{2\pi}\left(\frac{\gamma}{2} - \log\left(\sqrt{2}\sigma\right) + \frac{3}{4}\right) \end{aligned} \tag{1-47}$$

and for the 3D function:

$$\begin{aligned} G_2(0) &= \frac{1}{4}\,\frac{\sqrt{2}}{\pi^{3/2}\sigma} & G_6(0) &= \frac{15}{32}\,\frac{\sqrt{2}}{\pi^{3/2}\sigma} & G_{10}(0) &= \frac{315}{512}\,\frac{\sqrt{2}}{\pi^{3/2}\sigma} \\ G_4(0) &= \frac{3}{8}\,\frac{\sqrt{2}}{\pi^{3/2}\sigma} & G_8(0) &= \frac{35}{64}\,\frac{\sqrt{2}}{\pi^{3/2}\sigma} \end{aligned} \tag{1-48}$$

From the relation $\boldsymbol{K}(r) = \dfrac{d}{dr}G(r)\,\boldsymbol{e}_r$ the corresponding velocity kernels $\boldsymbol{K}$ of m-th order are now easily found to be:

$$\boldsymbol{K}_m(\boldsymbol{\rho}) = \begin{cases} -\dfrac{1}{2\pi\,\sigma\,\rho}\left(1 - P_m(\rho)\,\exp\left(-\dfrac{\rho^2}{2}\right)\right)\boldsymbol{e}_r & \text{in 2D,} \\ -\dfrac{1}{4\pi\sigma^2\rho^2}\left(Q_m(\rho)\,\exp\left(-\dfrac{\rho^2}{2}\right) + \operatorname{erf}\left(\dfrac{\rho}{\sqrt{2}}\right)\right)\boldsymbol{e}_r & \text{in 3D,} \end{cases} \tag{1-49}$$

where the polynomials P_m for the 2D function are given for $m = \{2, 4, 6, 8, 10\}$ by:

$$\begin{aligned} P_2(\rho) &= 1 & P_8(\rho) &= 1 - \frac{3}{2}\rho^2 + \frac{3}{8}\rho^4 - \frac{1}{48}\rho^6 \\ P_4(\rho) &= 1 - \frac{1}{2}\rho^2 & P_{10}(\rho) &= 1 - 2\rho^2 + \frac{3}{4}\rho^4 - \frac{1}{12}\rho^6 + \frac{1}{384}\rho^8 \\ P_6(\rho) &= 1 - \rho^2 + \frac{1}{8}\rho^4 \end{aligned} \tag{1-50}$$

and the polynomials Q_m for the 3D function are given by:

$$\begin{aligned} Q_2(\rho) &= \frac{1}{\sqrt{2\pi}}\left(-2\rho\right) & Q_8(\rho) &= \frac{1}{\sqrt{2\pi}}\left(-2\rho + \frac{89}{24}\rho^3 - \frac{20}{24}\rho^5 + \frac{1}{24}\rho^7\right) \\ Q_4(\rho) &= \frac{1}{\sqrt{2\pi}}\left(-2\rho + \rho^3\right) & Q_{10}(\rho) &= \frac{1}{\sqrt{2\pi}}\left(-2\rho + \frac{1027}{192}\rho^3 - \frac{349}{192}\rho^5\right. \\ Q_6(\rho) &= \frac{1}{\sqrt{2\pi}}\left(-2\rho + \frac{9}{4}\rho^3 - \frac{1}{4}\rho^5\right) & &\left. + \frac{35}{192}\rho^7 - \frac{1}{192}\rho^9\right) \end{aligned} \tag{1-51}$$

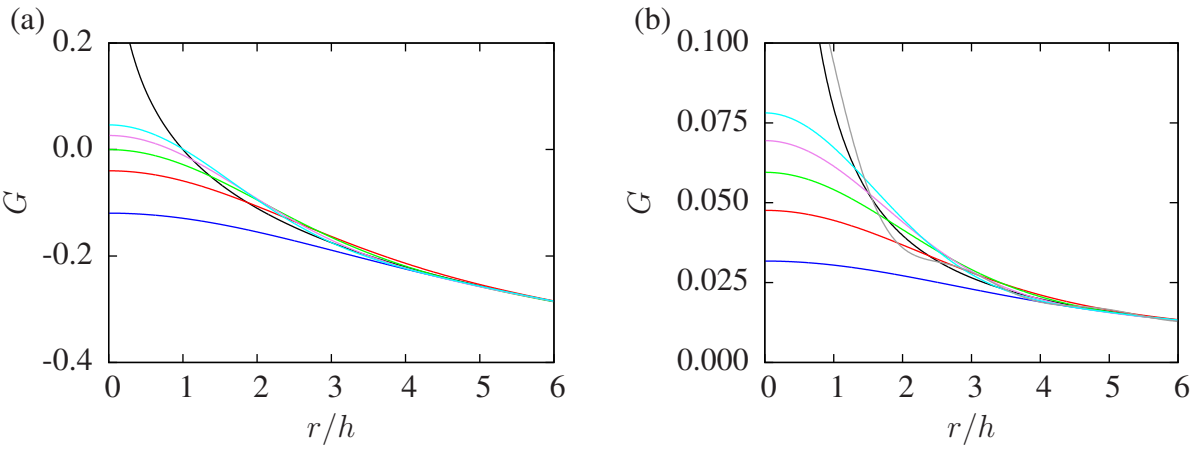

Figure 1.2: Regularised Green's functions for 2D (a) and 3D (b). The singular Green's functions G: (———). The Gaussian regularised Green's functions G_m with $\sigma = 2h$ for $m = 2$: (———); $m = 4$: (———); $m = 6$: (———); $m = 8$: (———); $m = 10$: (———). Bessel function regularisation with $\sigma = h/\pi$: (———).

The derived regularised Green's functions up to $m = 10$ are shown in Figs. 1.2 for G_m and in Fig. 1.3 for $\boldsymbol{K}_m$. As seen, the regularised Green's functions are all smoothly converging towards a finite value at $r = 0$ and towards the singular kernel functions for $r \to \infty$. The derived Green's functions are consistent with those presented in (Leonard, 1980; Beale and Majda, 1985; Perlman, 1985; Winckelmans and Leonard, 1993) and have here been extended to higher order. Furthermore, the value of $G_m(0)$ has been defined which allows for the integration kernels to be implemented in the FFT-based Poisson solver presented in Sec. 2.1.

1.3.2 *Regularisation by Gaussian smoothing for domains with mixed periodic and free-space boundary conditions in 2D and in 3D with two periodic and one free-space direction*

Analogous to Sec. 1.2 we now derive the regularised Green's functions for the Poisson equation with mixed periodic and free-space boundary conditions in 2D, and then extend the result to the 3D case with two periodic and one free-space direction. In 2D with one periodic (the y-direction) and one free-space (the x-direction) boundary conditions, the regularised Green's function is thus found by the inverse Fourier transform:

$$G_m(r,z) = \frac{1}{2\pi}\int_{-k_s/2}^{k_s/2}\left(\frac{1}{2\pi}\int_{-\infty}^{\infty}\frac{\widehat{\zeta}_m(k_x^2+k_y^2)}{k_x^2+k_y^2}\exp\left(\iota\, k_x\, x\right)\, dk_x\right)\exp\left(\iota\, k_y\, y\right)\, dk_y \qquad (1\text{-}52)$$

For the Green's function which has been Fourier transformed in the y-direction and using normalised coordinates, we have:

$$\widehat{G}_m(\rho_x, s_y) = \frac{\sigma}{2\pi}\int_{-\infty}^{\infty}\frac{\widehat{\zeta}_m(s_x^2+s_y^2)}{s_x^2+s_y^2}\exp\left(\iota\, s_x\, \rho_x\right)\, ds_x \qquad (1\text{-}53)$$

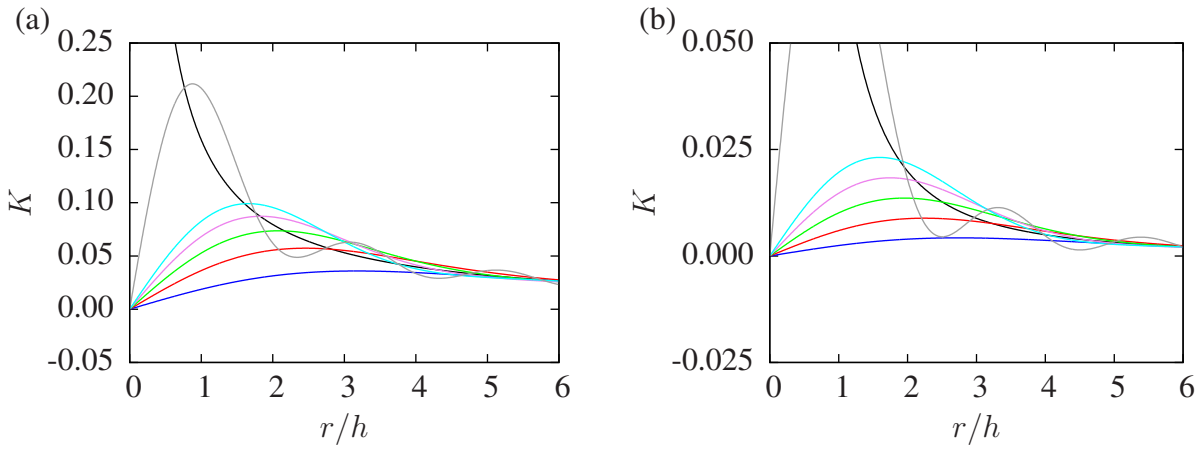

Figure 1.3: Regularised Green's functions for the gradient of the potential in 2D (a) and 3D (b). The singular Green's functions $\boldsymbol{K}$: (——). The Gaussian regularised Green's functions $\boldsymbol{K}_m$ with $\sigma = 2h$ for $m = 2$: (——); $m = 4$: (——); $m = 6$: (——); $m = 8$: (——); $m = 10$: (——). Bessel function regularisation with $\sigma = h/\pi$: (——).

where $s_x = \sigma\, k_x$, $s_y = \sigma\, k_y$, and $\rho_x = |x|/\sigma$. Inserting the Gaussian regularisation function on the generic form:

$$\widehat{\zeta}_m\left(s_x^2 + s_y^2\right) = D_m\left(s_x^2 + s_y^2\right)\, \exp\left(-\frac{s_x^2 + s_y^2}{2}\right) \tag{1-54}$$

we get:

$$\widehat{G}_m(\rho_x, s_y) = \frac{\sigma}{2\pi} \exp\left(-\frac{\rho_x^2 + s_y^2}{2}\right) \int_{-\infty}^{\infty} \frac{D_m(s_x^2 + s_y^2)}{s_x^2 + s_y^2} \exp\left(-\frac{(s_x - \iota\, \rho_x)^2}{2}\right)\, ds_x \tag{1-55}$$

By a change of variables and using integration by parts this integral may be found on the general form:

$$\begin{aligned}\widehat{G}_m(\rho, s) = \frac{\sigma}{4\, s}\Bigg(&\left(1 - \text{ erf}\left(\frac{s-\rho}{\sqrt{2}}\right)\right)\, \exp\left(-s\,\rho\right) + \left(1 - \text{ erf}\left(\frac{s+\rho}{\sqrt{2}}\right)\right)\, \exp\left(s\,\rho\right)\Bigg) \\ &+ \frac{\sigma\sqrt{2}}{\sqrt{\pi}}\, P_m(s,\rho)\, \exp\left(-\frac{s^2+\rho^2}{2}\right)\end{aligned} \tag{1-56}$$

Here $P_m(s,\rho)$ is a polynomial which for $m = \{2, 4, 6, 8, 10\}$ is given by:

$$\begin{aligned} P_2(s,\rho) &= 0 & P_8(s,\rho) &= \frac{11}{32} + \frac{1}{12}s^2 - \frac{1}{8}\rho^2 - \frac{1}{48}s^2\rho^2 + \frac{1}{96}(s^4 + \rho^4) \\ P_4(s,\rho) &= \frac{1}{4} & P_{10}(s,\rho) &= \frac{93}{256} + \frac{73}{768}s^2 - \frac{47}{256}\rho^2 - \frac{17}{384}s^2\rho^2 + \frac{11}{768}s^4 \\ P_6(s,\rho) &= \frac{5}{16} + \frac{1}{16}(s^2 - \rho^2) & &+ \frac{23}{768}\rho^4 + \frac{1}{256}(s^2\rho^4 - s^4\rho^2) + \frac{1}{768}(s^6 - \rho^6) \end{aligned} \tag{1-57}$$

with:

$$s = \begin{cases} |s_y| & \text{for 2D} \\ \sqrt{s_y^2 + s_z^2} & \text{for 3D} \end{cases} \qquad \text{and} \qquad \rho = \begin{cases} |\rho_x| & \text{for 2D} \\ |\rho_x| & \text{for 3D} \end{cases} \tag{1-58}$$

For the case of $s = 0$ we once again may define the Green's function arbitrarily as it represents the average value of the solution which for a potential is arbitrarily defined.

1.3.3 Ideal regularisation by Bessel functions for unbounded domains

Given the basic constraints on the regularisation function in Eq. (1-32) an ideal regularisation is obtained when:

$$\widehat{\zeta}(k) = \begin{cases} 1 & \text{for} \quad 0 < k \leq \dfrac{k_s}{2} \\ 0 & \text{for} \quad \dfrac{k_s}{2} < k \end{cases} \tag{1-59}$$

On account of the structure of radial Fourier transform we may in fact construct ideal regularisation functions by utilising the following integral identity of the Bessel functions given by (Olver et al., 2010):

$$\widehat{\zeta}(s) = \int_0^\infty J_\mu(a\rho) J_{\mu-1}(b\rho)\, d\rho = \begin{cases} b^{\mu-1}\, a^{-\mu} & \text{for} \quad 0 < b < a \\ (2b)^{-1} & \text{for} \quad a = b \\ 0 & \text{for} \quad 0 < a < b \end{cases} \tag{1-60}$$

For the 2D case with free-space boundary conditions it is seen from the radial Fourier transform of the regularisation function:

$$\widehat{\zeta}(s) = 2\pi\sigma^2 \int_0^\infty \zeta(\rho) J_0(s\,\rho)\rho\, d\rho \tag{1-61}$$

that an ideal regularisation can be obtained by the Bessel function:

$$\zeta(\rho) = \frac{J_1(\rho)}{2\pi\,\sigma^2\,\rho} \tag{1-62}$$

after which the regularisation function in Fourier space is given by Eq. (1-60) with $\mu = 1$, $a = 1$ and $b = s$:

$$\widehat{\zeta}(s) = \int_0^\infty J_1(\rho) J_0(s\,\rho)\, d\rho = \begin{cases} 1 & \text{for} \quad 0 < s < 1 \\ 1/2 & \text{for} \quad s = 1 \\ 0 & \text{for} \quad 1 < s \end{cases} \tag{1-63}$$

We determine σ by fulfilling $s = \sigma\, k = 1$ for $k = k_s/2$ by which:

$$\sigma\,\frac{k_s}{2} = \sigma\frac{\pi}{h} = 1 \qquad \Rightarrow \qquad \sigma = \frac{h}{\pi} \tag{1-64}$$

after which an ideal regularisation function is obtained.

From radial integration of the equation Eq. (1-9) in real space we may obtain the corresponding Green's function as:

$$G(r) = -\frac{1}{2\pi\,\sigma}\int \frac{1 - J_0(\rho)}{\rho}\, d\rho = -\frac{1}{2\pi\,\sigma}\sum_{i=1}^{\infty}(-1)^{i-1}\frac{\left(\dfrac{\rho}{2}\right)^{2\,i}}{2\,i\,(i\,!)^2} \tag{1-65}$$

This expression is however very computationally expensive to evaluate as it contains large factorials for an accurate estimate. The Green's function for the gradient is however easier to evaluate as it is given by:

$$\boldsymbol{K}(\boldsymbol{\rho}) = -\frac{1 - J_0(\rho)}{2\pi\,\sigma\,\rho}\,\boldsymbol{e}_r \qquad \text{with} \qquad \boldsymbol{K}(\boldsymbol{0}) = \boldsymbol{0} \tag{1-66}$$

This result is similar to that presented in (Leonard, 1980; Winckelmans and Leonard, 1993).

We may now use a similar approach to estimate the ideal regularised Green's function for the 3D Poisson equation with free-space boundary conditions. The radial Fourier transform of the regularisation function is given as:

$$\widehat{\zeta}(s) = (2\pi)^{3/2}\,\sigma^3 \int_0^\infty \zeta(\rho)\,\frac{J_{1/2}(s\,\rho)}{(s\,\rho)^{1/2}}\rho^2\,d\rho \tag{1-67}$$

where defining the regularisation function as:

$$\zeta(\rho) = \frac{J_{3/2}(\rho)}{(2\pi\,\rho)^{3/2}\,\sigma^3} \tag{1-68}$$

gives the regularisation function in Fourier space as:

$$\widehat{\zeta}(s) = \frac{1}{s^{1/2}}\int_0^\infty J_{3/2}(\rho)\,J_{1/2}(s\,\rho)\,d\rho = \begin{cases} 1 & \text{for} \quad 0 < s < 1 \\ 1/2 & \text{for} \quad s = 1 \\ 0 & \text{for} \quad 1 < s \end{cases} \tag{1-69}$$

This has been obtained by Eq. (1-60) with $\mu = 3/2$, $a = 1$ and $b = s$ and an ideal regularisation is then given analogous to the 2D case by setting $\sigma = h/\pi$.

By radial integration in real space we obtain the Green's function as:

$$G(\rho) = \frac{\mathrm{Si}(\rho)}{2\pi^2\sigma\,\rho} \qquad \text{with} \qquad G(0) = \frac{1}{2\pi^2\sigma} \tag{1-70}$$

and the Green's function for the gradient:

$$\boldsymbol{K}(\boldsymbol{\rho}) = \frac{\sin(\rho) - \mathrm{Si}(\rho)}{2\pi^2\sigma^2\rho^2}\boldsymbol{e}_\rho \qquad \text{with} \qquad \boldsymbol{K}(\boldsymbol{0}) = \boldsymbol{0} \tag{1-71}$$

Here $\mathrm{Si}(\rho) = \displaystyle\int_0^\rho \frac{\sin(q)}{q}\,dq$.

The regularisation function is shown in Fig. 1.1 and the corresponding Green's functions in Figs. 1.2 and 1.3 compared to the counterparts using regularisation by Gaussian smoothing.

1.4 The regularisation method for a multi-resolution Poisson solver

As mentioned in the introduction, the particle-mesh method introduces a shortest distance for which singular particles can interact without being subject to significant smoothing error. For

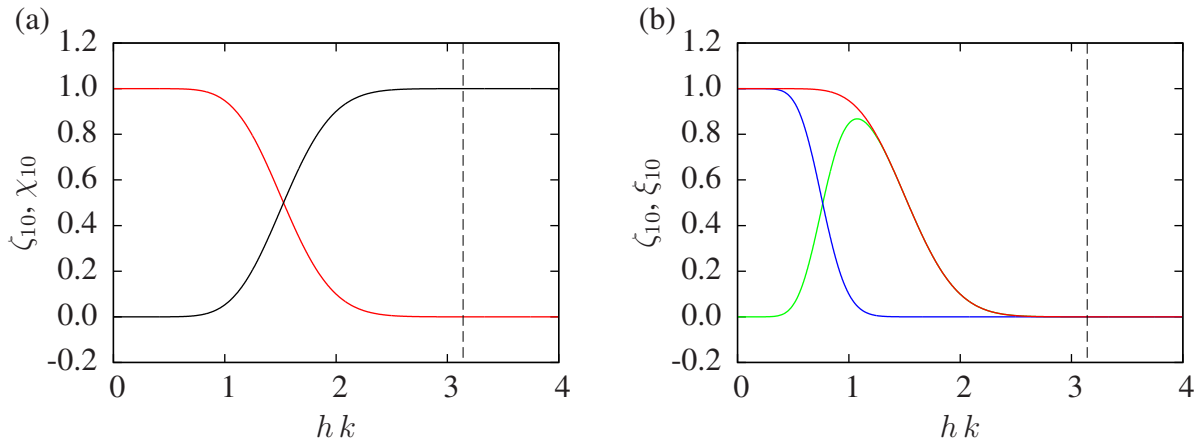

Figure 1.4: (a) the 10th order Gaussian regularisation function with $\sigma = 2\,h$ in Fourier space (———) and its spectral complement (———) used for the particle-particle correction in the P^{3}M method. (b) the 10th order Gaussian regularisation function with $\sigma = 2\,h$ corresponding to the coarse mesh (———), the corresponding correction regularisation function (———), and the resulting regularisation obtained by super-position (———).

the vector field representation this equals a highest resolved scale characterised by the Nyquist-Shannon sampling theorem. However due to the linearity of the Poisson equation we may decompose the problem into a multi-scale formulation which can be solved independently and use a super-position of the solutions to solve the full problem. This strategy is used in the particle-particle particle-mesh method (P^{3}M) (Hockney and Eastwood, 1988; Walther, 2003; Luty and van Gunsteren, 1996) to perform singular particle interactions using a particle-mesh method for the large scales and a particle-particle interaction for recovering the unresolved part of the potentials.

1.4.1 Singular particle interactions

Using the regularisation frame-work introduced in Sec. 1.3 we may formulate the singular distribution by:

$$\delta(\boldsymbol{r}) = \zeta_m\left(\frac{\boldsymbol{r}}{\sigma}\right) + \left(\delta(\boldsymbol{r}) - \zeta_m\left(\frac{\boldsymbol{r}}{\sigma}\right)\right) = \zeta_m(\rho) + \chi_m(\rho) \tag{1-72}$$

with $\boldsymbol{r} = \boldsymbol{x} - \boldsymbol{x}'$. Here $\chi_m(\rho) = \delta(\rho) - \zeta_m(\rho)$ is the "spectral complement" of the regularisation function which in Fourier space is given by $\widehat{\chi}_m(s) = 1 - \widehat{\zeta}_m(s)$ and is shown in Fig. 1.4.

For the homogeneous equation Eq. (1-9) we may introduce the decomposition of Eq. (1-72) after which we get:

$$\boldsymbol{\nabla}^2 G(\rho) = -\left(\zeta_m(\rho) + \chi_m(\rho)\right) \tag{1-73}$$

The Green's function may thus also be decomposed as:

$$\boldsymbol{\nabla}^2 G(\rho) = \boldsymbol{\nabla}^2 G_m(\rho) + \boldsymbol{\nabla}^2 S_m(\rho) \tag{1-74}$$

where:

$$\boldsymbol{\nabla}^2 G_m(\rho) = -\zeta_m(\rho) \qquad \text{and} \qquad \boldsymbol{\nabla}^2 S_m(\rho) = -\chi_m(\rho) \tag{1-75}$$

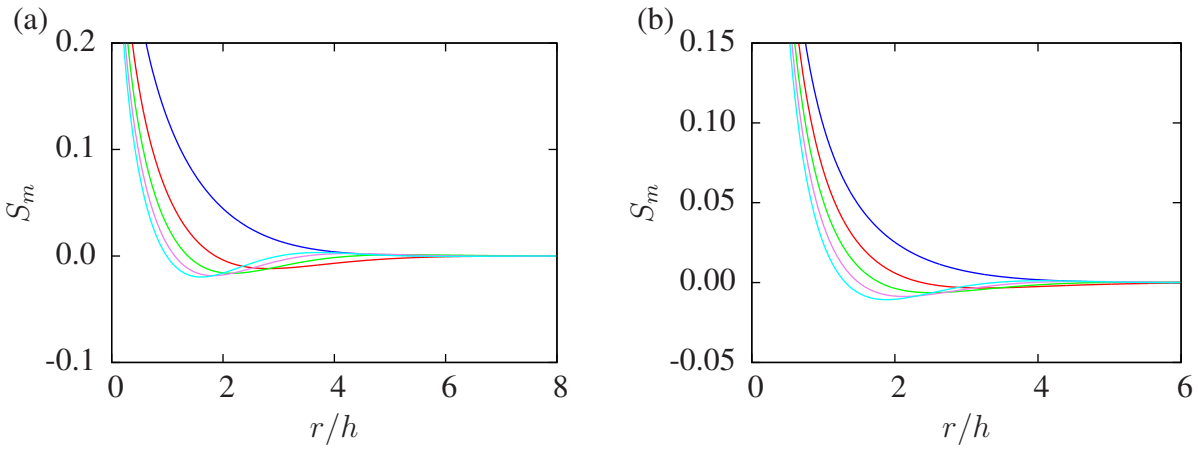

Figure 1.5: The 2D (a) and 3D (b) Green's functions for particle-particle correction of a Gaussian regularisation with $\sigma = 2\,h$. $m = 2$: (——); $m = 4$: (——); $m = 6$: (——); $m = 8$: (——); $m = 10$: (——).

The former equation is the regularised equation whose Green's function was derived in Sec. 1.3 and represents the interactions that can be resolved on the mesh and can thus be calculated using the particle-mesh method. The latter equation represents the residual potential which can be calculated using a direct particle-particle evaluation with the nearby particles. The Green's functions for the corrections towards a singular interaction is given by:

$$S_m(\rho) = \begin{cases} -\dfrac{1}{2\pi}\left(P_m(\rho)\,\exp\left(-\dfrac{\rho^2}{2}\right) - \dfrac{1}{2}\,\mathrm{E}_1\left(\dfrac{\rho^2}{2}\right)\right) & \text{in 2D,} \\ \dfrac{1}{4\pi\,\sigma\,\rho}\left(1 - Q_m(\rho)\,\exp\left(-\dfrac{\rho^2}{2}\right) - \mathrm{erf}\left(\dfrac{\rho}{\sqrt{2}}\right)\right) & \text{in 3D,} \end{cases} \tag{1-76}$$

The obtained Green's functions are seen in Fig. 1.5. Here it is noticed that the singular interaction is re-introduced and that the correction Green's function converges to zero relatively fast. This behaviour illustrates that it is indeed only the particles in the close vicinity that contributes to the particle-particle correction term.

1.4.2 The multi-resolution method

The same approach is now used to formulate a multi-resolution method for the vector field representation. However instead of using a particle-particle correction we now use a number particle-mesh solvers at a higher resolution in order to recover a band of smaller scales. Again we make a decomposition of the regularisation function as in Eq. (1-72) however now using n number of "nested" regularisation functions which effectively serves a filter-bank of band-pass filters. Hence we may decompose the highest resolved filter at level n into the sum of the coarsest (low-pass) filter at level 0 plus the n multi-resolution (band-pass) filters ξ_m for the refinement meshes of mesh cell length h_j where $j = \{0, 1, \ldots, n\}$:

$$\zeta_m(\rho_n) = \zeta_m(\rho_0) + \sum_{j=1}^{n} \xi_m(\rho_j) \qquad \text{where} \qquad \rho_j = \frac{r}{\sigma_j} \quad \text{and} \quad \sigma_j = \alpha\, h_j \tag{1-77}$$

The band-pass regularisation functions are then given by:

$$\xi_m(\rho_j) = \zeta_m(\rho_j) - \zeta_m\left(\frac{\rho_j}{a_j}\right) \qquad \text{where} \qquad a_j = \frac{h_{j-1}}{h_j} > 1 \tag{1-78}$$

The Green's function is decomposed in a similar fashion:

$$\boldsymbol{\nabla}^2 G(\rho_n) = \boldsymbol{\nabla}^2 G_m(\rho_0) + \sum_{j=1}^{n} \boldsymbol{\nabla}^2 C_m(\rho_j) \tag{1-79}$$

leading to two equations for the regularised homogeneous solutions:

$$\boldsymbol{\nabla}^2 G_m(\rho_0) = -\zeta_m(\rho_0) \qquad \text{and} \qquad \boldsymbol{\nabla}^2 C_m(\rho_j) = -\xi_m(\rho_j) \tag{1-80}$$

The former is the, by now familiar, regularised equation whose Green's function was derived in Sec. 1.3 and thus represents the regularised homogeneous solution of the coarser scales that can be calculated using the particle-mesh method on the base mesh h_0. The latter equation represents each of the n refinement levels used to recover the finer scales of the solution by additional particle-mesh evaluations which can be super-positioned with the base solution by interpolation schemes. The Green's functions for the refined scales are given in 2D by:

$$C_m(\rho_j, a_j) = \frac{1}{2\pi}\left(P_m(\rho_j)\,\exp\left(-\frac{\rho_j^2}{2}\right) - P_m\left(\frac{\rho_j}{a_j}\right)\,\exp\left(-\frac{\rho_j^2}{2\,a_j^2}\right)\right. \tag{1-81}$$

$$\left. -\frac{1}{2}\,\mathrm{E}_1\left(\frac{\rho_j^2}{2}\right) + \frac{1}{2}\,\mathrm{E}_1\left(\frac{\rho_j^2}{2\,a_j^2}\right)\right) \tag{1-82}$$

and in 3D by:

$$C_m(\rho_j, a_j) = \frac{1}{4\pi\,\sigma\,\rho_j}\left(Q_m(\rho_j)\,\exp\left(-\frac{\rho_j^2}{2}\right) - Q_m\left(\frac{\rho_j}{a_j}\right)\,\exp\left(-\frac{\rho_j^2}{2\,a_j^2}\right)\right. \tag{1-83}$$

$$\left. +\,\mathrm{erf}\left(\frac{\rho_j}{\sqrt{2}}\right) - \,\mathrm{erf}\left(\frac{\rho_j}{\sqrt{2}\,a_j}\right)\right) \tag{1-84}$$

An easy way to arrive at this result is to use the linearity of the problem by which:

$$C_m(\rho_j) = G_m\left(\rho_j\right) - G_m\left(\frac{\rho_j}{a_j}\right) \tag{1-85}$$

The obtained Green's functions are seen in Fig. 1.6. Here it is noticed that a similar convergence towards zero as for the singular correction functions is also observed for the Green's functions for mesh refinement. As will be shown in the following chapter the fast convergence towards zero can be utilised to reduce the computational load of the numerical implementation.

Now that the homogeneous solutions are found we may solve the Poisson equation by the principle of super-position of solutions:

$$\phi(\boldsymbol{x}) = \sum_{i=1}^{N_0} G_m\left(\frac{\boldsymbol{x}-\boldsymbol{x}_i}{\sigma_0}\right)\,\vartheta_i \;+\; \sum_{j=1}^{n}\sum_{i=1}^{N_j} C_m\left(\frac{\boldsymbol{x}-\boldsymbol{x}_i}{\sigma_j}\right)\,\vartheta_i \tag{1-86}$$

$$= \phi_0(\boldsymbol{x}) \;+\; \sum_{j=1}^{n} \phi_j(\boldsymbol{x}) \tag{1-87}$$

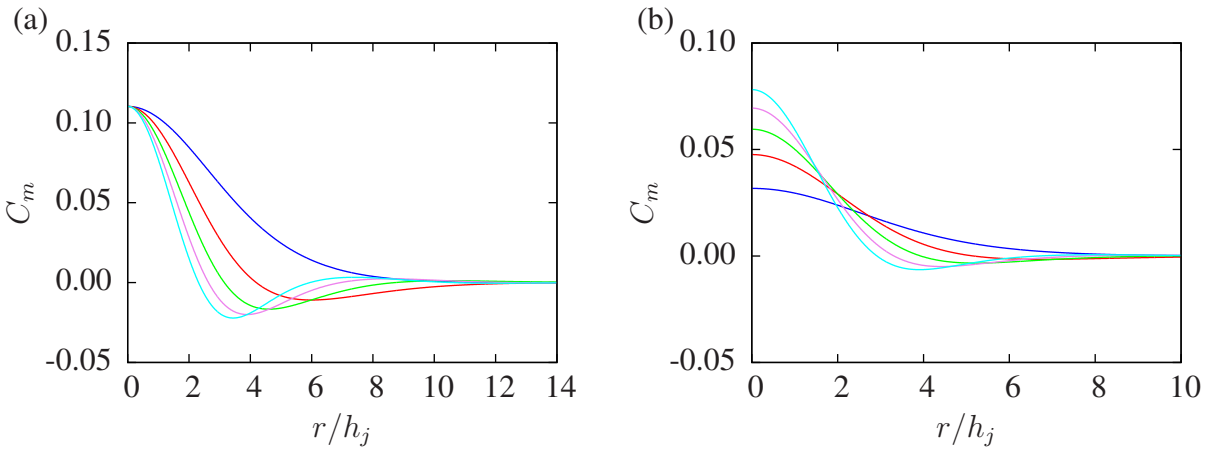

Figure 1.6: The 2D (a) and 3D (b) Green's functions for mesh-mesh correction of a coarse meshed Gaussian regularisation with $\sigma_j = 2\,h_j$ a refinement increment of $a_j = 2$. $m = 2$: (——); $m = 4$: (——); $m = 6$: (——); $m = 8$: (——); $m = 10$: (——).

and similarly for the vector potential:

$$\boldsymbol{\psi}(\boldsymbol{x}) = \sum_{i=1}^{N_0} G_m\left(\frac{\boldsymbol{x}-\boldsymbol{x}_i}{\sigma_0}\right)\,\boldsymbol{\omega}_i \;+\; \sum_{j=1}^{n}\sum_{i=1}^{N_j} C_m\left(\frac{\boldsymbol{x}-\boldsymbol{x}_i}{\sigma_j}\right)\,\boldsymbol{\omega}_i \tag{1-88}$$

$$= \boldsymbol{\psi}_0(\boldsymbol{x}) \;+\; \sum_{j=1}^{n} \boldsymbol{\psi}_j(\boldsymbol{x}) \tag{1-89}$$

here N_j is the number of discrete element on level j and n is the number of refinement levels. As seen, the full solution consists of a super-position of filtered solutions which are calculated individually on meshes of different discretisations. This super-position calls for additional schemes depending on the structure of the data-points. The schemes which is used in the current numerical implementation is presented in the following chapter.

Chapter 2

Numerical implementation of the high order regularised Poisson solver

2.1 The regularised Poisson solver with free-space boundary conditions

In Sec. 1.1 it was shown that the solution of the Poisson equation for free-space boundary conditions was obtained by a convolution with a Green's function. As mentioned in the introduction this is done in the particle-mesh method by interpolating the intrinsic particle quantities to a uniform mesh. The data-structure of the mesh enables the use of FFT-based convolution. In order to circumvent the the inherent periodicity of the FFT convolution for free-space boundary conditions we adopt a zero-padding method introduced by (Hockney and Eastwood, 1988).

To investigate the discrete convolution theorem we start by defining a convolution kernel A and a field B (which in our method is represented by the Green's function and the divergence or curl, respectively):

$$A = \Big\{ A_i : i \in \{-M, -M+1, ..., M-1\} \Big\} \quad \text{and} \quad B = \Big\{ B_i : i \in \{0, 1, ..., N-1\} \Big\} \tag{2-1}$$

Here N is the number of mesh cells for the field B and $M \leq N$ is the extent of the convolution kernel A i.e. the radius of which the interaction is active. We note that the length of A is $2M$ and for $M = N$ the interaction is active in the entire domain. We seek the solution of the linear convolution of A and B is which we denote by C and is given by the set:

$$C = \Big\{ C_i = (A * B)_i : i \in \{0, 1, ..., N-1\} \Big\} \tag{2-2}$$

The discrete equivalent for the unbounded linear convolution operator Eq. (1-7) is given by:

$$(A * B)_i = h \sum_{l=-\infty}^{\infty} A_{i-l}\, B_l \quad \text{with} \quad i = \{0, 1, ..., \infty\} \tag{2-3}$$

which due by the bounds of the respective variables can be re-written to the bounded solution C_i as:

$$C_i = (A * B)_i = h \sum_{l=0}^{M-1} A_{i-l}\, B_l \quad \text{with} \quad i = \{0, 1, ..., N-1\} \tag{2-4}$$

The convolution may be calculated effectively by using the convolution theorem of the Fourier transform. The 1D discrete Fourier transform of an array A_i and its inverse transform are given by:

$$\widehat{\mathcal{A}}_j = h \sum_{i=0}^{n-1} \mathcal{A}_i \, \exp\left(-\frac{2\pi\, \iota\, i\, j}{n} \right) \qquad \text{and} \qquad \mathcal{A}_i = \frac{1}{n\, h} \sum_{j=0}^{n-1} \widehat{\mathcal{A}}_j \, \exp\left(\frac{2\pi\, \iota\, i\, j}{n} \right) \tag{2-5}$$

Here n is the discrete integration length of the Fourier transforms and $\mathcal{A}_i$ is the modified array of A_i which has been modified for the discrete Fourier transform. The modification of $A_i \mapsto \mathcal{A}_i$ consists of first extending the array A_i with zeros in order to obtain a length of n. Then all the values of indexes $i < 0$ of the extended A_i are shifted to append the values of indexes $i \geq 0$ such that the length of the adjusted variable $\mathcal{A}_i$ is indeed n with $i = \{0, 1, \dots, n-1\}$ as is needed in the discrete Fourier transform. The discrete Fourier transforms can be calculated effectively by the recursive FFT algorithm which is one of the clear advantages of the particle-mesh method. From the convolution theorem the Fourier transform of the convolution may be obtained by the product of the Fourier transformed variables:

$$\widehat{\mathcal{C}}_j = \widehat{\mathcal{A}}_j \, \widehat{\mathcal{B}}_j = \left(h \sum_{i=0}^{n-1} \mathcal{A}_i \, \exp\left(-\frac{2\pi \, \iota \, i \, j}{n} \right) \right) \left(h \sum_{i=0}^{n-1} \mathcal{B}_i \, \exp\left(-\frac{2\pi \, \iota \, i \, j}{n} \right) \right) \tag{2-6}$$

$$= h \sum_{i=0}^{n-1} \left(h \sum_{l=0}^{i} \mathcal{A}_{i-l} \, \mathcal{B}_l + h \sum_{l=i+1}^{n-1} \mathcal{A}_{i+n-l} \, \mathcal{B}_l \right) \, \exp\left(-\frac{2\pi \, \iota \, i \, j}{n} \right) \tag{2-7}$$

(no summation over the indexes for $\widehat{\mathcal{A}}_j \, \widehat{\mathcal{B}}_j$). Here we have used an index shift in the summation combined with the shift theorem of the exponential functions. As seen we obtain an expression which is of the form of a discrete Fourier transform and we may thus inverse Fourier transform the expression to obtain the discrete integral:

$$\mathcal{C}_i = h \sum_{l=0}^{i} \mathcal{A}_{i-l} \, \mathcal{B}_l + h \sum_{l=i+1}^{n-1} \mathcal{A}_{i+n-l} \, \mathcal{B}_l \tag{2-8}$$

Here it is seen that reversing the permutation and extension such that $\mathcal{A}_i \mapsto A_i$ and choosing $n = N + M$ we indeed obtain the linear convolution of Eq. (2-4). It is here emphasised that the FFT-based convolution is an exact method for evaluating the discrete integral of the convolution and thus cannot introduce any additional artefacts that may otherwise be related to Fourier series e.g. Gibbs phenomena. Hence the only error is the quadrature of the discrete integral which convergences in a rate proportional to the smoothness of the field.

Using $A_i = G(\boldsymbol{r}_i)$ and $B_i = \vartheta_i$ or $B_i = \boldsymbol{\omega}_i$ with $M = N$ due to the extent of the Green's function, the Poisson equations of Eq. (1-2) may thus be solved by:

$$\widehat{\phi} = \widehat{G} \, \widehat{\vartheta} \qquad \text{and} \qquad \widehat{\boldsymbol{\psi}} = \widehat{G} \, \widehat{\boldsymbol{\omega}} \tag{2-9}$$

The linearity of the Poisson equation enables the gradient to be calculated directly in Fourier space. This can easily be done choosing one of the two methods:

$$\widehat{\boldsymbol{v}} = \widehat{\boldsymbol{K}} \times \widehat{\boldsymbol{\omega}} - \widehat{\boldsymbol{K}} \, \widehat{\vartheta} \qquad \text{or} \qquad \widehat{\boldsymbol{v}} = \iota \boldsymbol{k} \times \widehat{\boldsymbol{\psi}} - \iota \boldsymbol{k} \, \widehat{\phi} \tag{2-10}$$

The zero-padded FFT convolution evidently has a significant impact on the computational footprint of the method, however it can be reduced from $(2N)^d$ to $2N^d + (2N)^{d-1}$. As proposed by (Hockney and Eastwood, 1988) one may transform the entire field in one or two directions and then proceed with a plane-by-plane convolution as is elaborated in Fig. 2.1. The method, however, still requires the Green's function to be calculated initially and stored in their full size of $(2N)^d$. This however only needs to be done when re-sizing the domain which is relatively few times during a simulation. For the present implementation we use the pencil convolution (cf. Fig. 2.1) in order to improve the computational scaling when performing multi-processor computations.

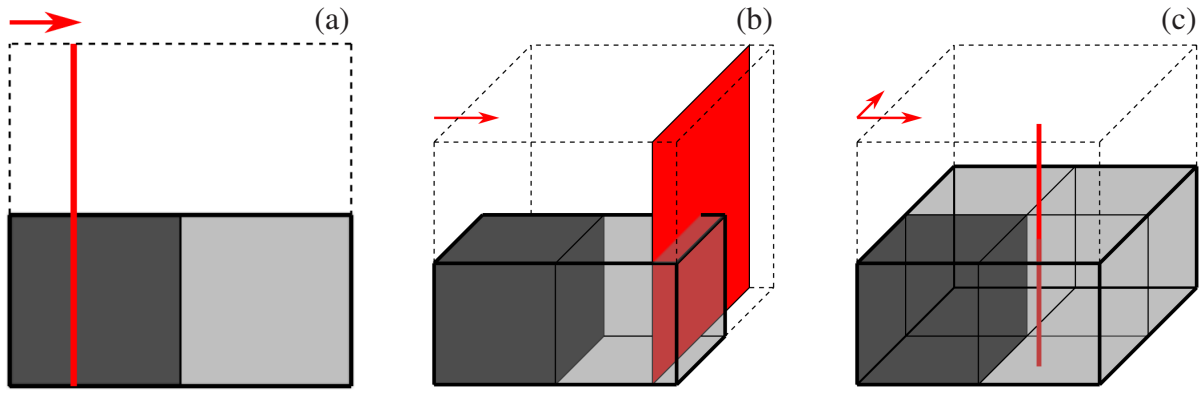

Figure 2.1: Sketch of the zero-padded FFT scheme as proposed by (Hockney and Eastwood, 1988) for (a) 2D, (b) 3D using planes (slabs), and (c) 3D using lines (pencils). The dark-grey represents the actual computational domain. The light-grey represents the initial zero-padding and Fourier transform of either one or two directions. The red line or plane represents the convolution operation where the data is zero-padded and Fourier-transform in the remaining dimensions, then multiplied by the Green's function $\widehat{G}$ and inverse transformed discarding the data of the zero-padding. Once the convolution has traversed the grey data block (indicated by the red arrows) the initial directions may be inverse transformed to recover the solution in real space.

2.2 The regularised Poisson solver with mixed free-space and periodic boundary conditions

For a fully periodic domain the inherent periodicity of the FFT is utilised to obtain the periodicity of the convolution. Hence the domain is not zero-padded and we simply write the Green's function directly in Fourier space as:

$$\widehat{G}(k) = \frac{1}{k^2} \qquad \text{with} \qquad \widehat{G}(k) = 0 \quad \text{for} \quad k = 0 \tag{2-11}$$

The potential functions and the velocity field may be calculated by Eqs. (2-9) and (2-10), respectively.

For mixed periodic and free-space boundary conditions the domain should still be extended however only in the free-space directions. As mentioned briefly in the introduction a naive method of achieving mixed periodic and free-space boundary conditions is to simply use the method of repeating domains. Here the semi-periodic boundary conditions are obtained by summing N_L Green's functions on both sides of the domain which is shifted by the domain length L and thus implicitly emulating a periodic domain:

$$G(\boldsymbol{r}) = \sum_{i=-N_L}^{N_L} G(\boldsymbol{r} - i\,L) \tag{2-12}$$

The more formal approach to obtain mixed periodic and free-space boundary conditions (Chatelain and Koumoutsakos, 2010) is to include the appropriate boundary conditions in the analytical derivation of the Green's functions as done in Sec. 1.2 for the singular distributions

and in Sec. 1.3.2 for the distributions regularised by Gaussian smoothing of high order. Here the Green's function is already partially defined in Fourier space and the function thus only needs to be transformed in the free-space directions using zero-padding for linear convolution. Also here the potential functions and the velocity field may then be calculated by Eqs. (2-9) and (2-10), respectively.

2.3 Implementation of the regularised multi-resolution Poisson solver

The implementation of the multi-resolution solver, whose regularised Green's functions were derived in Sec. 1.4.2, is done by defining local patches of refined meshes as is illustrated in Fig. 2.2. The individual solution on the base mesh and the refinement patches is obtained accordingly to the previous Sec. 2.1 using the appropriate Green's functions. Here it is noted that as the Green's functions of the refinement patches are those of Eqs. (1-82) and (1-84) which was shown to be approximately bounded functions cf. Fig. 1.6. This behaviour may be utilised to reduce the computational footprint of solving the refinement meshes as the extent of the convolution kernel $\mathcal{A}_i$ in Eq. (2-8) becomes less than N after which the zero-padding is reduced together with the length of the Fourier transforms. In the presented study a value of $M = 32$ is used by which the length of the Fourier transformed arrays becomes $N + 32$.

Once the individual solutions are obtained on all meshes the solutions needs to be superpositioned in order to obtain the full solution accordingly to Eqs. (1-87) and (1-89). The superposition of the solution is done by a moment conserving mesh-to-mesh interpolation between a refined patch and its coarser parent mesh. The interpolation between the meshes may be written on the general form:

$$A_f = \sum_c A_c \, W\left(\frac{\boldsymbol{x}_c - \boldsymbol{x}_f}{h_c}\right) \tag{2-13}$$

where the sub-indexes c and f denotes the coarse and refined mesh values, respectively and $W(\boldsymbol{x})$ is the interpolation kernel. The interpolation kernel may be composed as the outer product of the one dimensional interpolation functions $W(\boldsymbol{x}_{ijk}) = M(x_i)M(y_j)M(z_k)$.

Using a B-spline interpolation proposed by (Monaghan, 1985) we may obtain a third order interpolation scheme by using the $M = M_4'$ interpolation function:

$$M_4'(q) = \begin{cases} 0 & \text{for} \quad 2 < |q| \\ \frac{1}{2}(2-|q|)^2(1-|q|) & \text{for} \quad 1 < |q| \leq 2 \\ 1 - \dfrac{5|q|^2}{2} + \dfrac{3|q|^3}{2} & \text{for} \quad |q| \leq 1 \end{cases} \tag{2-14}$$

A fourth order interpolation scheme is obtained using the $M = M_6^*$ interpolation function (Bergdorf and Koumoutsakos, 2006; van Rees et al., 2011):

$$M_6^*(q) = \begin{cases} 0 & \text{for} \quad 3 < |q| \\ -\frac{1}{24}(|q|-2)(|q|-3)^3(5|q|-8) & \text{for} \quad 2 < |q| \leq 3 \\ \frac{1}{24}(|q|-1)(|q|-2)(25|q|^3 - 114|q|^2 + 153|q| - 48) & \text{for} \quad 1 < |q| \leq 2 \\ -\frac{1}{12}(|q|-1)(25|q|^4 - 38|q|^3 - 3|q|^2 + 12|q| + 12) & \text{for} \quad |q| \leq 1 \end{cases} \tag{2-15}$$

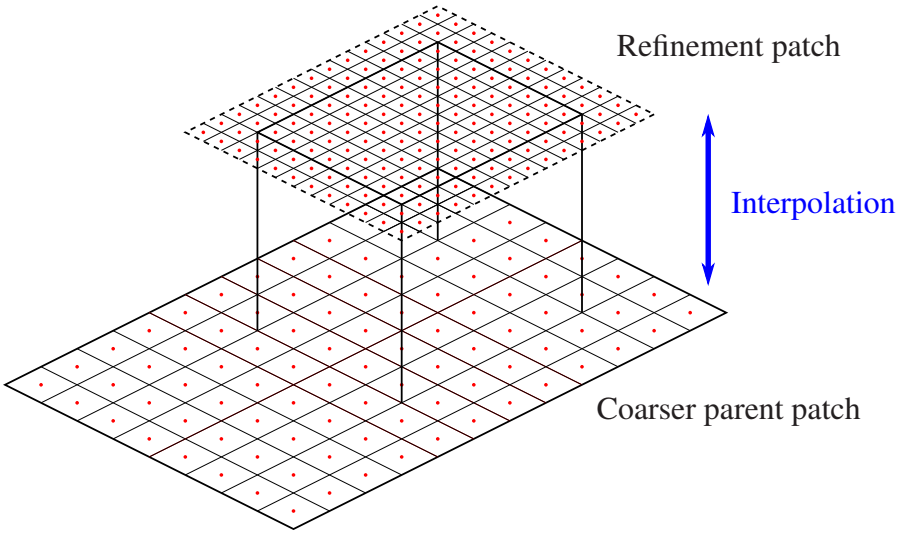

Figure 2.2: Sketch of the numerical implementation of the multi-resolution method using refinement patches with a staggered mesh configuration. The super-position of the solution between the meshes in done via mesh-mesh interpolation where the edge of the refinement mesh is appended with a layer of ghost cells to ensure that the interpolation function is fully supported on the mesh.

In the current implementations we use a staggered mesh refinement as seen Fig. 2.2 where the mesh nodes of the refinement mesh does not coincide with the mesh nodes of its parent mesh. The staggered configuration is practical when using a particle-mesh method as the particles represent an integral value of a density field and is then easily super-positioned. Furthermore, regarding the multi-patch implementation of a particle-mesh method it should be mentioned that some effort must be devoted to correctly ensure the inter-patch consistency of the right-hand-side of the Poisson equation. In doing so it is unavoidable to do a patch-to-parent interpolation going from a fine resolution to a coarser one. This can be done similarly to the interpolation method described however it is here emphasised that one should still use the coarse mesh length h_c as the support of the interpolation function in order to avoid aliasing artefacts in the solution. Hence the interpolation from a fine mesh to a coarse mesh takes the form:

$$A_c = \frac{h_f^d}{h_c^d} \sum_f A_f \, W \left(\frac{\boldsymbol{x}_f - \boldsymbol{x}_c}{h_c} \right) \tag{2-16}$$

For specific details on a complete particle-mesh method using multi-patch refinement, the reader is referred to (Rasmussen et al., 2011) for which the presented multi-resolution Poisson solver is compatible.

Chapter 3

Validation of the regularised Poisson solver

3.1 Convergence test with free-space boundary conditions

The regularised Green's functions of Chapter I-1 together with the numerical implementation of Chapter I-2 is now tested to validate the convergence rate of the Poisson solver with respect to the discretisation length. To investigate the convergence of the Poisson solver, the test function must be bounded within the computational domain for the directions with free-space boundary conditions, and fully continuously differentiable in the direction with periodic boundary conditions. In the presented examples we test the Poisson solver for calculating the vector field $\boldsymbol{v}$ given a defined distribution of the curl $\boldsymbol{\omega}$ through Eqs. (1-1) and (1-2) with $\vartheta = 0$.

Additionally, the test function must have at least two continuous derivatives which is a direct consequence of the mapping of the Laplace operator $\nabla^2 : C^m \mapsto C^{m-2}$ after which $m \geq 2$ is needed to give a continuous solution for the Poisson equation. However, in order to make the quadrature error insignificant and thus allowing an arbitrary high convergence rate the test function must be infinitely differentiable. To meet these requirements we propose the use of a bump function distribution which is of class C^∞ i.e. it has an infinite number of continuous derivatives. The bump function is defined as:

$$f(q) = \begin{cases} \exp\left(-\dfrac{c}{1-q^2}\right) & \text{for} \quad |q| < 1 \\ 0 & \text{for} \quad |q| \geq 1 \end{cases} \tag{3-1}$$

where c is an arbitrary positive constant which for the presented cases $c = 10$ is chosen. In order to obtain bounded test functions, the bump function is used as the radial distribution of a circular patch in 2D and of a torus in 3D as is shown in Fig. 3.1. Using centred polar coordinates (r, θ) in 2D and cylindrical coordinates (r, θ, z) in 3D case the vector potential may then be defined as:

$$\psi = f\left(\frac{r}{R}\right) \quad \text{in 2D} \qquad \text{and} \qquad \boldsymbol{\psi} = f\left(\frac{\sqrt{(r-R)^2 + z^2}}{R}\right)\boldsymbol{e}_\theta \quad \text{in 3D} \tag{3-2}$$

Here R is the radius of the radial distribution of the bump function and $\boldsymbol{e}_\theta$ is the azimuthal normal vector in 3D. The resulting distribution of the curl $\boldsymbol{\omega}$ and corresponding vector field are found analytically by Eqs. (1-1) and (1-2), and is shown in Fig. 3.2.

We define the error of the calculated vector field $\boldsymbol{v}_i$ compared to the analytical solution which

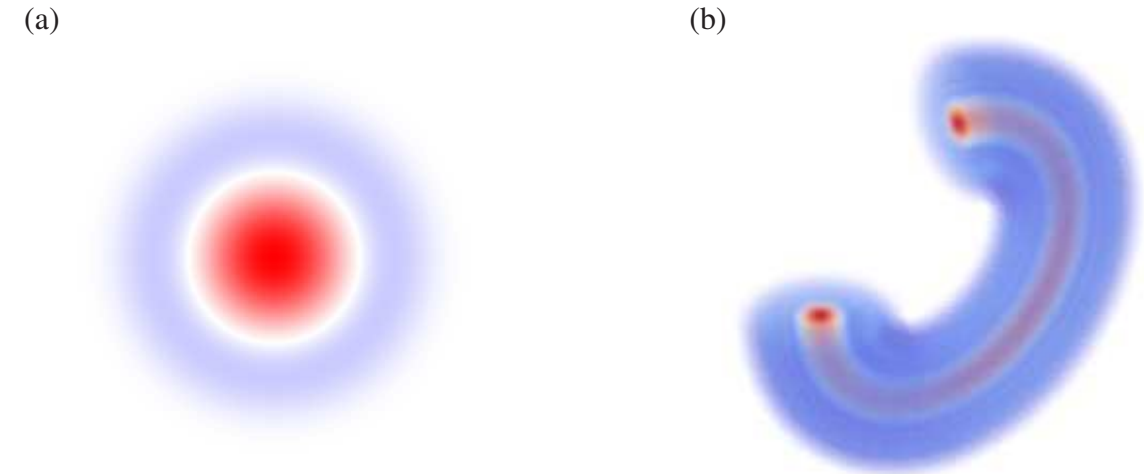

Figure 3.1: The distribution of $\boldsymbol{\omega}$ for the bump test function in 2D (a) and in 3D (b). The 3D test function is a closed torus but is shown in (b) without the upper left quadrant in order to make the core distribution visible.

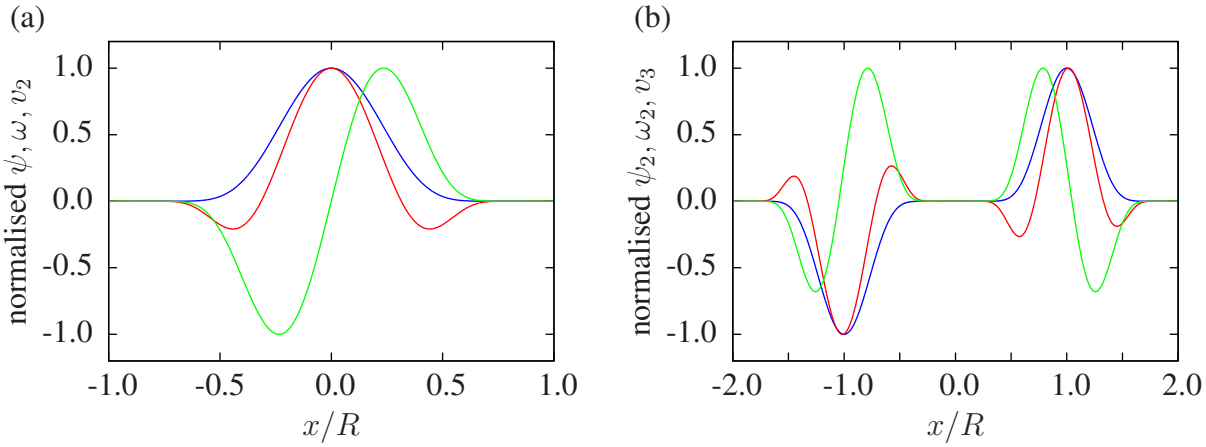

Figure 3.2: The normalised test function and the corresponding solution for $c = 10$: (a) the distribution of the 2D patch at the line given by $(x, y) = ([-1 : 1], 0)$ and (b) the distribution of the 3D torus at the line given by $(x, y, z) = ([-2 : 2], 0, 0)$. (——): circulation density $\omega_i/\max(\omega_i)$; (——): vector potential $\psi_i/\max(\psi_i)$; (——): vector field $v_i/\max(v_i)$.

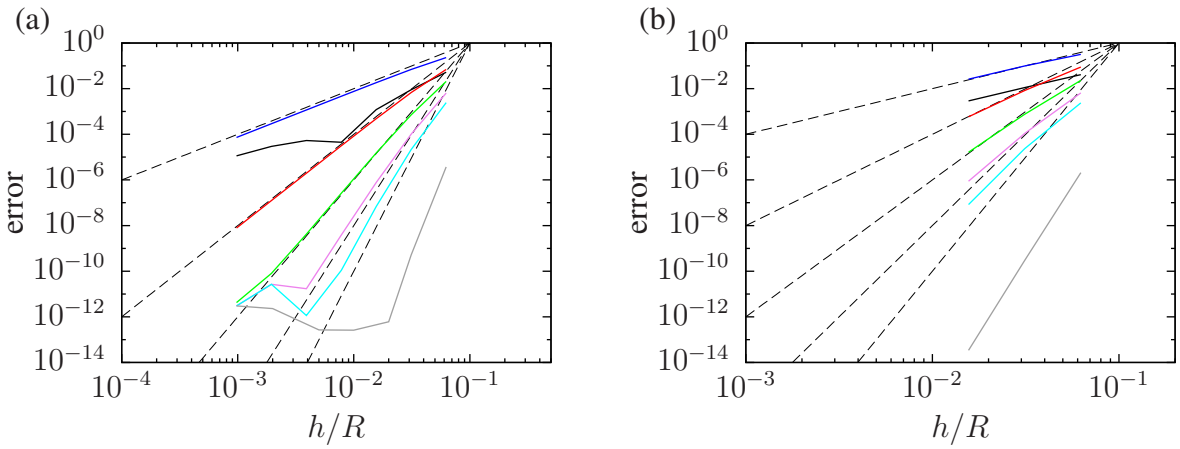

Figure 3.3: The error of the calculated solutions obtained by regularised Green's functions in 2D (a) and in 3D (b) for free-space boundary conditions. Convergence order: (– – –) from top $\mathcal{O}(h^2)$, $\mathcal{O}(h^4)$, $\mathcal{O}(h^6)$, $\mathcal{O}(h^8)$, $\mathcal{O}(h^{10})$; non-regularised kernels: (———); $m = 2$: (———); $m = 4$: (———); $m = 6$: (———); $m = 8$: (———); $m = 10$: (———); Bessel function regularisation: (———)

is sampled in the same points $\boldsymbol{v}(\boldsymbol{x}_i)$ as:

$$\text{error} = \left(\frac{\sum_{i=1}^{N} |\boldsymbol{v}(\boldsymbol{x}_i) - \boldsymbol{v}_i|^2 \, h_i^d}{\sum_{i=1}^{N} |\boldsymbol{v}(\boldsymbol{x}_i)|^2 \, h_i^d} \right)^{1/2} \tag{3-3}$$

The obtained error of the 2D and 3D convergence tests are shown in Fig. 3.3 for the regularised Green's functions of order $m = \{2, 4, 6, 8, 10\}$ using Gaussian smoothing and that of the ideal regularisation. As seen, the error of the 2D and the 3D convergence tests are concurring, and the convergence rate corresponds to the respective design parameters of the Green's functions.

A similar convergence rate is observed with the maximum error (not shown). Furthermore, the solution of the vector field is found to be practically identical, and with the same convergence properties, when using the analytical derivative of the Green's functions for $\boldsymbol{K}$ as when using the spectral differentiating in Eq. (2-10).

3.2 Convergence test with mixed periodic and free-space boundary conditions

As mentioned above the convergence test for mixed periodic and free-space boundary conditions demands a test function which is bounded within the computational domain for the free-space directions, and fully continuously differentiable in the periodic directions. This is obtained for the 2D case by mixing the bump function of Eq. (3-1) with a sine function for the free-space (x) and the periodic (y) directions, respectively. In the examples with mixed boundary conditions we test the Poisson solver for calculating the vector field $\boldsymbol{v}$ given a defined

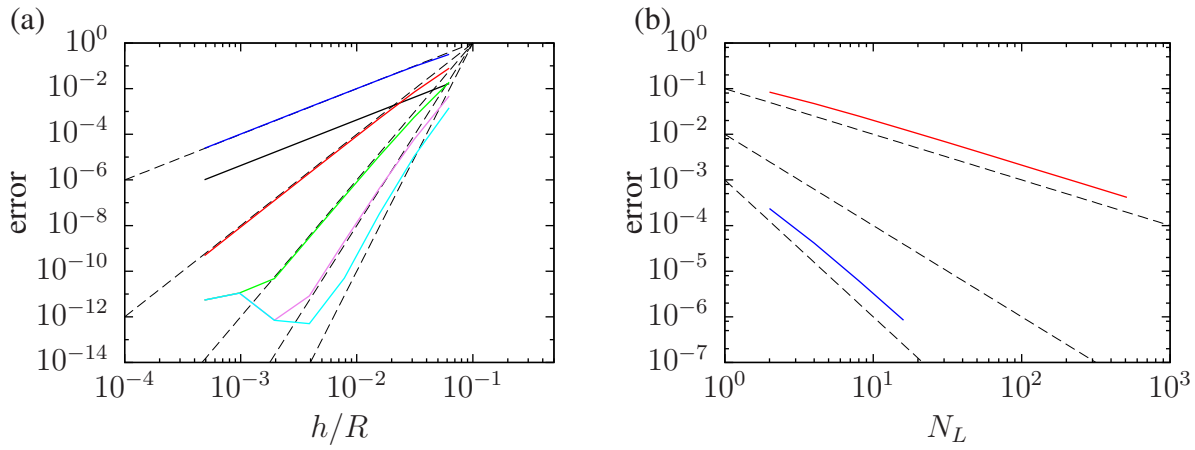

Figure 3.4: (a) The error of the calculated solutions obtained by regularised Green's functions in 2D for mixed periodic and free-space boundary conditions. Convergence order: (— — —) from top $\mathcal{O}(h^2)$, $\mathcal{O}(h^4)$, $\mathcal{O}(h^6)$, $\mathcal{O}(h^8)$, $\mathcal{O}(h^{10})$; non-regularised kernels: (———); $m = 2$: (———); $m = 4$: (———); $m = 6$: (———); $m = 8$: (———); $m = 10$: (———). (b) The error of the repeated domain method. Convergence order: (— — —) from top $\mathcal{O}(N_L^{-1})$, $\mathcal{O}(N_L^{-2})$, $\mathcal{O}(N_L^{-3})$; 2D periodic-free case: (———); 3D periodic-periodic-free case: (———).

distribution of the divergence ϑ through Eqs. (1-1) and (1-2) now with $\boldsymbol{\omega} = 0$:

$$\phi(x, y) = f\left(\frac{x}{R}\right) \sin(2\pi\, y) \quad \text{in 2D}, \tag{3-4}$$

and:

$$\phi(x, y, z) = f\left(\frac{x}{R}\right) \sin(2\pi\, y)\ \sin(2\pi\, z) \quad \text{in 3D} \tag{3-5}$$

The distribution of the divergence ϑ and corresponding vector field $\boldsymbol{v}$ are found analytically by Eqs. (1-1) and (1-2).

The obtained error for the regularised Poisson solver with mixed boundary conditions is shown in Fig. 3.4 compared to the non-regularised method of (Chatelain and Koumoutsakos, 2010) and the method of repeated domains cf. Sec. 2.2. Here it is seen that the method again obtains the convergence rate corresponding to the respective design parameters of the Green's functions. The regularised method is shown to quickly produce an error which is significantly lower than that of (Chatelain and Koumoutsakos, 2010) in the 2D case for $m > 2$. Regarding the method of repeated domains it is seen that the method converges with the number of repeated domains N_L as $\mathcal{O}(N_L^{-1})$ for 2D and $\mathcal{O}(N_L^{-3})$ for 3D. This is due to the decay of the Green's functions which is proportional to $1/r$ in 2D and $1/r^2$ in 3D as seen in Eq. (1-22) and hence the integral contribution of the repeated domains decreases one order faster in 3D than in 2D.

3.3 Convergence test for the multi-resolution method with free-space boundary conditions

The multi-resolution implementation of Secs. 1.4.2 and 2.3 are now validated for free-space boundary conditions. For this the free-space test function of Eqs. (3-1) and (3-2) are used with local refinement patches as seen in Fig. 3.5.

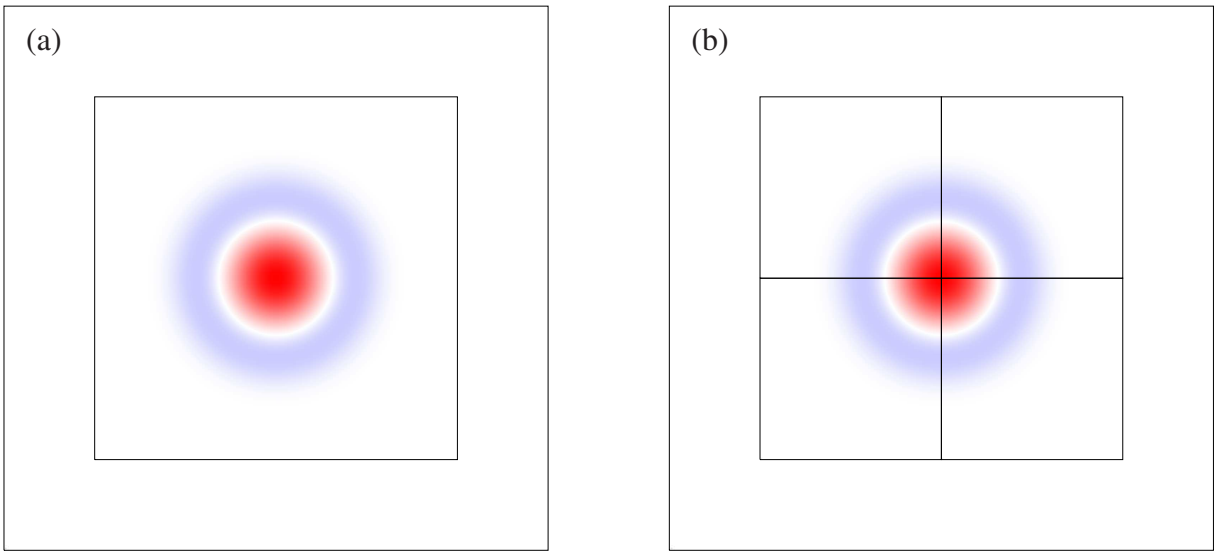

Figure 3.5: The 2D test function for free-space boundary conditions with the patch configuration used for the multi-patch convergence test. The one patch configuration (a) and the four patch configuration (b).

The obtained error of the multi-resolution method is shown in Figs. 3.6 and 3.7 where we test one level of refinement patches with two different ratios of mesh refinement which is $a_1 = 2$ and $a_1 = 3$. The method is tested using a single refinement patch or four bordering patches as seen in Fig. 3.5. For the case of the four bordering patches an overlapping ghost region of $a_1 \times 32$ cells are used according to the extent of the Green's function for the refinement patch (cf. Secs. 1.4.2 and 2.3).

The fourth order interpolation function M_6^* of Eq. (2-15) is used for the super-position of the solution. It is seen in Fig. 3.6 that the obtained rate of convergence obtains the order of the Green's functions for $m = \{2, 4\}$ however is limited by the interpolation scheme for higher order Green's function ($m > 4$). It is furthermore observed that for the larger mesh refinement ratio $a_1 = 3$ the error is larger when dominated by the interpolation error. Finally, it is noted that the method is capable of handling bordering refinement patches without increasing the error significantly as is shown in Fig. 3.7. This result assumes however that a sufficient amount of ghost cells are used as mentioned above.

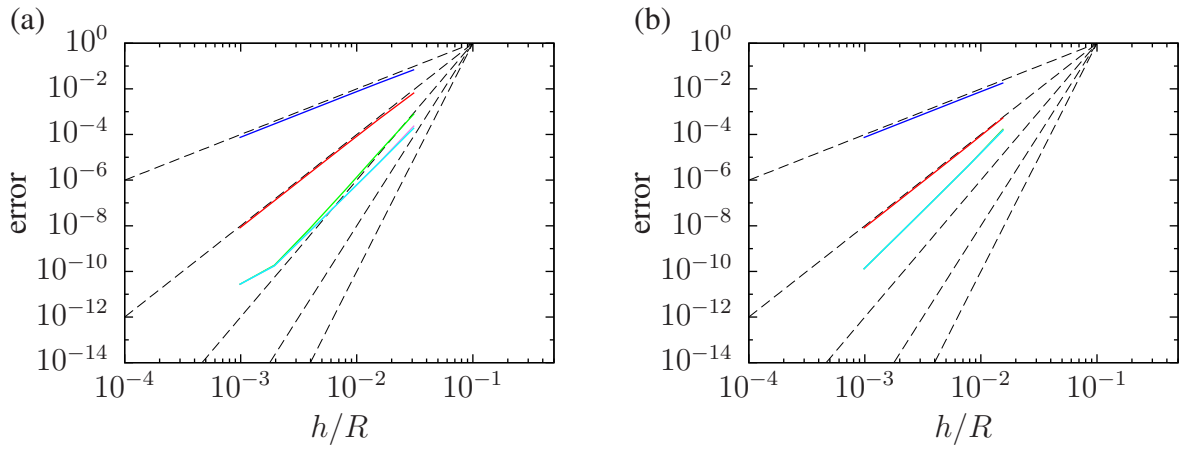

Figure 3.6: The error of the calculated solutions obtained by regularised Green's functions using the multi-resolution method with one patch and a mesh refinement ratio of $a_1 = 2$ (a) and $a_1 = 3$ (b) for free-space boundary conditions. Convergence order: (— — —) from top $\mathcal{O}(h^2)$, $\mathcal{O}(h^4)$, $\mathcal{O}(h^6)$, $\mathcal{O}(h^8)$, $\mathcal{O}(h^{10})$; $m = 2$: (———); $m = 4$: (———); $m = 6$: (———); $m = 8$: (———); $m = 10$: (———).

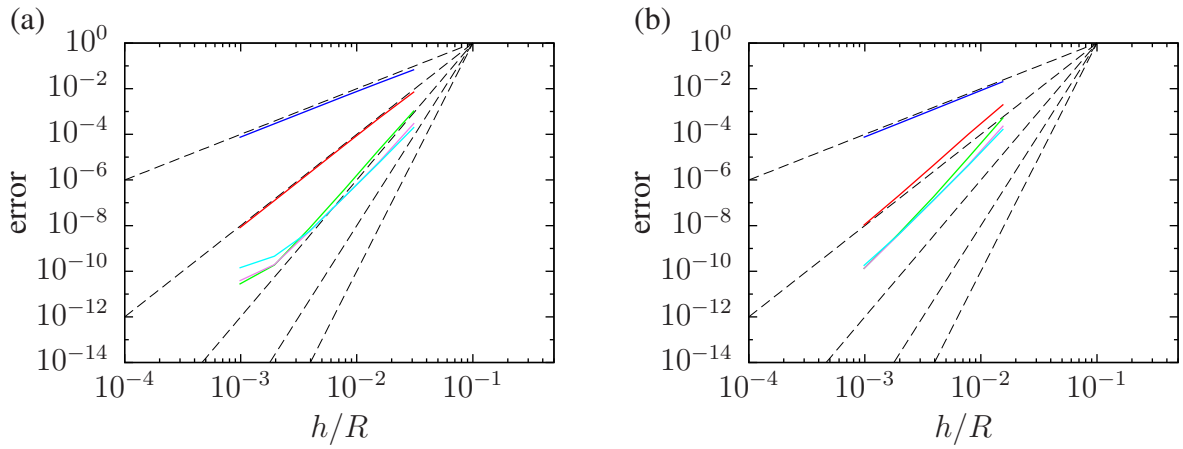

Figure 3.7: The error of the calculated solutions obtained by regularised Green's functions using the multi-resolution method with four patches and a mesh refinement ratio of $a_1 = 2$ (a) and $a_1 = 3$ (b) for free-space boundary conditions. Convergence order: (— — —) from top $\mathcal{O}(h^2)$, $\mathcal{O}(h^4)$, $\mathcal{O}(h^6)$, $\mathcal{O}(h^8)$, $\mathcal{O}(h^{10})$; $m = 2$: (———); $m = 4$: (———); $m = 6$: (———); $m = 8$: (———); $m = 10$: (———).

Conclusion

A regularisation method was presented for calculating the solution to the Poisson equation of a continuum field using Green's functions. The regularisation method is based on a method used in mesh-free vortex methods to produce regularised Green's functions ensure the numerical stability of the method. In this monograph an unconventional derivation of the regularisation is used which illuminate the approximative errors and the choice of regularisation parameters which is essential to the method.

The regularisation method which under certain conditions can be viewed as a discrete approximation to a smooth continuum field, was combined with the FFT-based Poisson solver of particle-mesh methods to achieve a method with an arbitrary high rate of convergence. The high order is achieved without any additional computational cost from the conventional FFT-based Poisson solver and is able to calculate the derivative of the solution to the same high order either by direct spectral differentiating or by analytically differentiating the Green's function.

The regularisation method was extended to achieve mixed periodic and free-space boundary conditions and to handle a local refinement of the solution by a patch-based multi-resolution method. The multi-resolution extension is achieved by combining the idea of a particle-particle correction from the P^3M method with the regularisation method in order to recover the solution from interactions of a sub-mesh scale.

For a full implementation of the presented regularised Poisson solver in a particle-mesh based method, the reader is referred to Part II of this dissertation. Regarding a full implementation of the multi-resolution method in a particle-mesh method the reader is referred to the approach of (Rasmussen et al., 2011) in terms of combining a mesh-based Poisson solver and particles in a multi-resolution implementation using local refinement patches.

Part B:

Articles of selected topics and applications of vortex methods

Article I

Simulations of a single vortex ring using an unbounded, regularised particle-mesh based vortex method

Mads Mølholm Hejlesen[1], Henrik Juul Spietz[1], Jens Honoré Walther[1,2]

[1]Department of Mechanical Engineering, Technical University of Denmark, Building 403, DK-2800 Kgs. Lyngby, Denmark

[2]Computational Science and Engineering Laboratory, ETH Zürich, Clausiusstrasse 33, CH-8092 Zürich, Switzerland

This chapter consists of a modified version of the conference article:
Simulations of a single vortex ring using an unbounded, regularised particle-mesh based vortex method. Proceedings of the 6th International Conference on Vortex Flows and Vortex Models, Nagoya, Japan, 2014.

Abstract

In resent work we have developed a new FFT based Poisson solver, which uses regularised Greens functions to obtain arbitrary high order convergence to the unbounded Poisson equation. The high order Poisson solver has been implemented in an unbounded particle-mesh based vortex method which uses a re-meshing of the vortex particles to ensure the convergence of the method. Furthermore, a re-projection of the vorticity field is applied to include the constraint of a divergence-free stream function which is essential for the underlying Helmholtz decomposition and ensures a divergence free vorticity field. The high order, unbounded particle-mesh based vortex method is used to simulate the instability, transition to turbulence and eventual destruction of a single vortex ring. From the simulation data a novel method on analysing the dynamics of the vortex ring enstrophy is presented based on the alignment of the vorticity vector with the principal axis of the strain rate tensor. We find that the dynamics of the enstrophy density is dominated by the local flow deformation and axis of rotation, which is used to infer some concrete tendencies related to the topology of the vorticity field.

I-1 Introduction

Vortex methods is a class of numerical methods that pre-dates the programmable computer. Vortex methods started out being popular due to its compact nature and limited number of degrees of freedom. As vorticity is a material property that is transported by the flow, it is conveniently solved in an Lagrangian formulation by using computational elements referred

to as particles. The Lagrangian formulation additionally has the fortunate consequence in 2D simulations of eliminating the non-linear terms of the vorticity equation and thus reducing it to a simple diffusion equation.

However, as the years past, the computational power increased and the field of scientific computing matured, leading to an ever growing demand for accuracy in computation simulations. This caused the majority of the computational fluid dynamics society to focus on mesh-based methods which has formal theory of convergence which cannot be generalised to particle methods. Furthermore, as the number of computational elements increased drastically the particle based vortex method suffered from low computational efficiency especially in 3D simulations.

In recent years vortex methods have been developed towards a hybrid particle-mesh formulation in order to ensure the formal convergence of the method. Here the vorticity of the particles is interpolated to an auxiliary equispaced mesh where the velocity-vorticity coupling constituted by a Poisson equation is efficiently solved. The velocity is then interpolated back to the particles which in turn is frequently re-initiated with uniform spacing (re-meshing) (Koumoutsakos and Leonard, 1995). Re-meshing has been shown to be an important factor for the convergence of particle based methods (Cottet and Koumoutsakos, 2000).

Another challenge that one faces using particle-based vortex methods for 3D simulations, is to preserve a divergence-free vorticity field. As the trajectory of the particles are solved numerically to a finite order of accuracy the solution is subject to an error accordingly. As a consequence, the particles are formally no longer material points and the resulting error is manifested as a divergence in the vorticity field.

In resent work we have developed a particle-mesh based vortex method to perform simulations of unbounded flows. The method is implemented using particle re-meshing to ensure a numerical convergence and a re-projection which ensures a divergence-free vorticity field (Cottet and Koumoutsakos, 2000). The high order method is achieved by using a recently developed unbounded Poisson solver (Hejlesen et al., 2013) based on a regularisation of the Greens function to obtain arbitrary high order convergence. Using the unbounded solver we are able to minimise the size of the auxiliary mesh while imposing strict free-space boundary conditions. In this way we avoid exposing the simulation to erroneous boundary conditions.

Vortex rings have been subject to intense experimental and numerical research (Shariff and Leonard, 1992; Bergdorf et al., 2007; Archer et al., 2008) in order to gain valuable insights into the evolution, instability and break down of vortex structures. Studying the flow topology of this fundamental flow structure has extended the knowledge of dynamical instability and the eventual transition to turbulence of vortical flow structures. Although extensive, much of the analysis of the previous investigations has been focused on the topology of the vortex core structure and the time history of various moments of the flow field. Only little focus has been put into analysing the local deformation of vorticity and the formation of secondary vortex structures (Bergdorf et al., 2007).

In this work we present simulations of a single vortex ring using the aforementioned particle-mesh based vortex method with free-space boundary conditions. We present a detailed analysis on the alignment of the vorticity and the principal axes of the strain rate tensor which is shown to have a great significance to the changes of enstrophy density in the flow (Jimenez et al., 1993; Jiménez and Wray, 1998; Wallace, 2009).

The vortex and enstrophy dynamics represent an essential process in the characteristic transfer properties of kinetic energy in turbulence (Moser et al., 1999; Zeff et al., 2003; Bernard,

2006; Wallace, 2009). As the topology of the vorticity field is deformed into sheet- and tube-like structures, the conservation of angular momentum constitutes an energy transfer between different length scales of the flow. The coupling of the vorticity and kinetic energy is given by the enstrophy density which can be viewed as a quantity representing the local rotational kinetic energy of the fluid. Thus any preferred alignment of the vorticity vector has a direct consequence on the isotropic properties of the turbulent energy transfer and has a significant role in many other topics of fluid dynamics. An example of this is found in aero-acoustics where the generated vortex sound is significantly reduced if the local vorticity becomes aligned with the velocity (Powell, 1964). Thus an in depth knowledge of vortex deformation and alignment is essential for multiple disciplines in fluid dynamics.

I-2 Methodology

The velocity-vorticity formulation of the Navier-Stokes equations can be solved in a Lagrangian frame of reference by advecting computational particles which represents an elementary distribution of vorticity often referred to as a vortex blob. Hence the particle position $\boldsymbol{x}_p$ is solved in the Eulerian frame of reference by:

$$\frac{d}{dt}\boldsymbol{x}_p = \boldsymbol{v}(\boldsymbol{x}_p) \tag{I-1}$$

where $\boldsymbol{v}$ is the velocity vector in the Eulerian frame of reference. In order to represent the vortex blob the particles are assigned a circulation $\boldsymbol{\xi}_p$ which may be obtained by interpolating the circulation field $\boldsymbol{\xi}(\boldsymbol{x})$ calculated by a regularisation of the vorticity field $\boldsymbol{\omega}$ by:

$$\boldsymbol{\xi}(\boldsymbol{x}) = h^3 \int_{\mathbb{R}^d} \zeta_m(\boldsymbol{x} - \boldsymbol{x}')\, \boldsymbol{\omega}(\boldsymbol{x}')\, d\boldsymbol{x}' \tag{I-2}$$

Here ζ_m is a moment conserving regularisation function of order m and h is the cell length of the auxiliary mesh. In this work we construct the regularisation function by de-convolving the Gaussian filter with an m-th order Taylor approximation. In this way the obtained method inherently resembles the de-convolution methods used in large eddy simulations (LES) (Stolz and Adams, 1999; Sagaut, 1998). It is here noticed that the specific method of regularisation results in a de-convolution method similar to that of (Stolz and Adams, 1999; Adams, 2011).

The vorticity equation which gives temporal change of the vorticity in a material point and thus insures the conservation of angular momentum is given by:

$$\frac{d}{dt}\boldsymbol{\omega} = \boldsymbol{\omega} \cdot \boldsymbol{\nabla}\boldsymbol{v} + \nu \boldsymbol{\nabla}^2 \boldsymbol{\omega} \tag{I-3}$$

The equivalent regularised equation for the circulation is thus found by filtering the vorticity equation accordingly to Eq. (I-2) which leaves:

$$\frac{d}{dt}\boldsymbol{\xi} = \boldsymbol{\xi} \cdot \boldsymbol{\nabla}\boldsymbol{v} + \nu \boldsymbol{\nabla}^2 \boldsymbol{\xi} + \mathcal{O}(h^m) \tag{I-4}$$

Here ν is the kinematic viscosity and an error term is included instead of the sub-grid stresses usually seen in LES equations. This replacement has been made under the assumption that all

flow scales are properly resolved by the discretisation after which the additional term represents a smoothing error of the regularisation function and is thus in the order h^m.

As the particles represents an integral of the vorticity we may reconstruct the vorticity field $\boldsymbol{\omega}(\boldsymbol{x})$ by utilising the super-position principle which for N particles is:

$$\boldsymbol{\omega}(\boldsymbol{x}) = \frac{1}{h^3}\sum_{p}^{N} \boldsymbol{\xi}_p \, W\left(\frac{\boldsymbol{x}_p - \boldsymbol{x}}{h}\right) \tag{I-5}$$

Here $W(x)$ is the interpolation kernel.

In order to calculate the velocity field we use a functional orthogonal decomposition leaving:

$$\boldsymbol{\nabla}^2\boldsymbol{v} = \boldsymbol{\nabla}(\boldsymbol{\nabla}\cdot\boldsymbol{v}) - \boldsymbol{\nabla}\times(\boldsymbol{\nabla}\times\boldsymbol{v}) \tag{I-6}$$

For an incompressible flow the velocity field is divergence free (i.e. $\boldsymbol{\nabla}\cdot\boldsymbol{v} = 0$) which can easily be obtained by nullifying the former term on the right-hand-side and thus by defining the vorticity as the curl of the velocity field one obtains:

$$\boldsymbol{\nabla}^2\boldsymbol{v} = -\boldsymbol{\nabla}\times\boldsymbol{\omega} \tag{I-7}$$

This equation is recognised as a Poisson equation and can thus be solved for unbounded boundary conditions to an arbitrary high order by a regularisation Green's function solution (Hejlesen et al., 2013).

I-2.1 Correction of divergence in the vorticity field

From the definition of vorticity $\boldsymbol{\omega} \equiv \boldsymbol{\nabla}\times\boldsymbol{v}$ we see that the vorticity field is inherently divergence-free as:

$$\boldsymbol{\nabla}\cdot\boldsymbol{\omega} = \boldsymbol{\nabla}\cdot(\boldsymbol{\nabla}\times\boldsymbol{v}) = 0 \tag{I-8}$$

The velocity field may be described by a Helmholtz decomposition:

$$\boldsymbol{v} = \boldsymbol{\nabla}\times\boldsymbol{\psi} - \boldsymbol{\nabla}\phi \qquad \text{with} \qquad \boldsymbol{\nabla}\cdot\boldsymbol{\psi} = 0 \tag{I-9}$$

Here ϕ is a scalar potential and $\boldsymbol{\psi}$ is a vector potential which is divergence-free in order to ensure the uniqueness of the decomposition in 3D. Again due to the constraint of an incompressible and thus a divergence-free velocity field we have that $\boldsymbol{\nabla}\phi = \boldsymbol{0}$.

From Eq. (I-9) and the definition of vorticity we may express the vorticity as:

$$\boldsymbol{\omega} = -\boldsymbol{\nabla}^2\boldsymbol{\psi} \tag{I-10}$$

It is now seen that the divergence of the vorticity field is:

$$\boldsymbol{\nabla}\cdot\boldsymbol{\omega} = -\boldsymbol{\nabla}^2(\boldsymbol{\nabla}\cdot\boldsymbol{\psi}) \tag{I-11}$$

In theory, the right-hand-side is zero due to the restriction of the Helmholtz decomposition cf. Eq. (I-9). However, the trajectory of the vortex particles, essentially represented by the stream function, which in turn is contained in the vector potential $\boldsymbol{\psi}$, is only solved numerically to

a finite order of accuracy. This gives cause to an error which manifests itself as a divergence in the vorticity field. To amend this error the vorticity field $\boldsymbol{\omega}_*$ where $\boldsymbol{\nabla} \cdot \boldsymbol{\omega}_* \neq 0$ should be corrected accordingly to:

$$\boldsymbol{\omega} = \boldsymbol{\omega}_* + \boldsymbol{\nabla}(\boldsymbol{\nabla} \cdot \boldsymbol{\psi}_*) \qquad \text{where} \qquad \boldsymbol{\nabla} \cdot \boldsymbol{\omega}_* = -\boldsymbol{\nabla}^2(\boldsymbol{\nabla} \cdot \boldsymbol{\psi}_*) \tag{I-12}$$

where the divergence of the uncorrected vector potential $\boldsymbol{\psi}_*$ is found by solving the latter equation which conveniently constitutes a Poisson equation and can thus be easily implemented in the existing Poisson solver. This method of correcting the divergence in the vorticity field, although derived differently, is equal to the re-projection method given by (Cottet and Koumoutsakos, 2000).

I-2.2 Analysis of the enstrophy by the alignment of the vorticity and the strain rate tensor

In the following section an inviscid assumption is made in order to exclusively investigate the inertial dynamics of the enstrophy and we thus disregards the diffusive behaviour of the fluid. From the vorticity equation (Eq. (I-3)) it is seen that the only non-diffusive term is the stretching term which may be re-written by decomposing the velocity gradient tensor into the strain rate tensor $\boldsymbol{S} = (\boldsymbol{\nabla v} + \boldsymbol{\nabla v}^T)/2$ and rotation rate tensor $\boldsymbol{R} = (\boldsymbol{\nabla v} - \boldsymbol{\nabla v}^T)/2$ as:

$$\boldsymbol{\omega} \cdot \boldsymbol{\nabla v} = \boldsymbol{\omega} \cdot (\boldsymbol{S} + \boldsymbol{R}) = \boldsymbol{\omega} \cdot \boldsymbol{S} \tag{I-13}$$

It is here noted that the vortex stretching is given by the inner product of the vorticity and the strain rate tensor. Given a sufficiently small control volume the vorticity can be viewed as the angular momentum of the volume per moment of inertia (Wu et al., 2006b). Furthermore, the strain rate tensor may be regarded as the change of the moment of inertia which, due to the conservation of angular momentum, causes a change in vorticity if these are properly aligned. In a similar fashion we will extend this view by interpreting the enstrophy density (defined by $\varepsilon = (\boldsymbol{\omega} \cdot \boldsymbol{\omega})/2$) as the rotational kinetic energy per moment of inertia. By substituting Eq. (I-13) into Eq. (I-3) and taking the inner product with the vorticity vector, an equation for the material derivative of the enstrophy density is derived for the inviscid case (i.e. $\nu = 0$):

$$\frac{d}{dt}\varepsilon = \boldsymbol{\omega} \cdot (\boldsymbol{\omega} \cdot \boldsymbol{S}) \tag{I-14}$$

Described in the principle axes of the strain rate tensor (denoted henceforth by a tilde) the strain rate tensor is diagonalised containing only its eigenvalues which represents the strain rate in the principal directions. Hence the enstrophy equation, which is invariant to rotation, may be written using the eigenvalues of the strain rate tensor:

$$\frac{d}{dt}\varepsilon = \tilde{\omega}_1^2 \, \lambda_1 + \tilde{\omega}_2^2 \, \lambda_2 + \tilde{\omega}_3^2 \, \lambda_3 \tag{I-15}$$

where the eigenvalues are related as:

$$\lambda_1 \geq \lambda_2 \geq \lambda_3 \qquad \text{and} \qquad \lambda_1 + \lambda_2 + \lambda_3 = \boldsymbol{\nabla} \cdot \boldsymbol{v} = 0 \tag{I-16}$$

here enforcing the incompressibility constraint. Hence we may write the three contributions in Eq. (I-15):

$$\tilde{\omega}_1^2\lambda_1 = -\tilde{\omega}_1^2\left(\lambda_2+\lambda_3\right), \quad \tilde{\omega}_2^2\lambda_2 = -\tilde{\omega}_2^2\left(\lambda_1+\lambda_3\right) \quad \text{and} \quad \tilde{\omega}_3^2\lambda_3 = -\tilde{\omega}_3^2\left(\lambda_1+\lambda_2\right) \tag{I-17}$$

From this we can infer that the contributions to the change in enstrophy is governed by the fluid deformation (given by the eigenvalues) in the plane perpendicular to the axis of rotation (given by the vorticity component). The governing dynamics of the enstrophy density may thus be parametrised as: 1) the alignment of the vorticity vector with the principal axes of the strain rate tensor and 2) the relation of the eigenvalues of the strain rate tensor. Where the former may by described by the normalised inner product (i.e. the alignment) of the vorticity and the eigenvectors, the latter is represented by the normalised skewness of the eigenvalues referred to as the deformation mode:

$$\text{mode}(\boldsymbol{S}) = \sqrt{2}\,\text{skewness}(\lambda_1,\lambda_2,\lambda_3) \tag{I-18}$$

Here a deformation mode of -1 corresponds to a disc-like deformation whereas a deformation mode of 1 corresponds to a tube-like deformation of a initially spherical fluid element.

I-3 Results

I-3.1 Simulations of a single vortex ring

Using the vortex method summarised above we simulate the evolution of a single vortex ring using the following parameters for Reynolds number, adaptive time step size and mesh cell size of:

$$\text{Re}_\Gamma = \frac{\Gamma}{\nu} = 10^4, \quad \delta t = \frac{0.1}{\max\left(|\boldsymbol{\omega}|\right)}, \quad \frac{h}{D} = \frac{1}{128} \tag{I-19}$$

Here Γ is the circulation of the vortex ring cross-section and D is the vortex ring diameter. In the presented implementation we use: a 3rd order scheme for interpolation between particles and mesh, a 3rd order scheme for calculating the trajectory of the particles, a 4th order finite difference scheme for calculating spatial derivatives, and a 10th order regularisation of the particles cf. (Hejlesen et al., 2013). In Fig. I-1 the magnitude of the vorticity is presented at six stages of the simulation. The vortex ring is initiated as a perturbed Gaussian distribution which becomes unstable, creating secondary vortex structures. At some point, the distortion of the vortex core leads to the break-down of the vortex ring topology and the vorticity field transcends into turbulence which eventually decays and dies out.

I-3.2 Analysis of the enstrophy by the alignment of vorticity and the deformation mode of the strain rate tensor

Using the analysis of Sec. I-2.2 based on the eigenvalues of the strain rate tensor the components contributing to the change of the enstrophy density is investigated by a field analysis in Fig. I-2 for stage B (cf. Fig. I-1). In this stage it is seen that clear regions are dominated

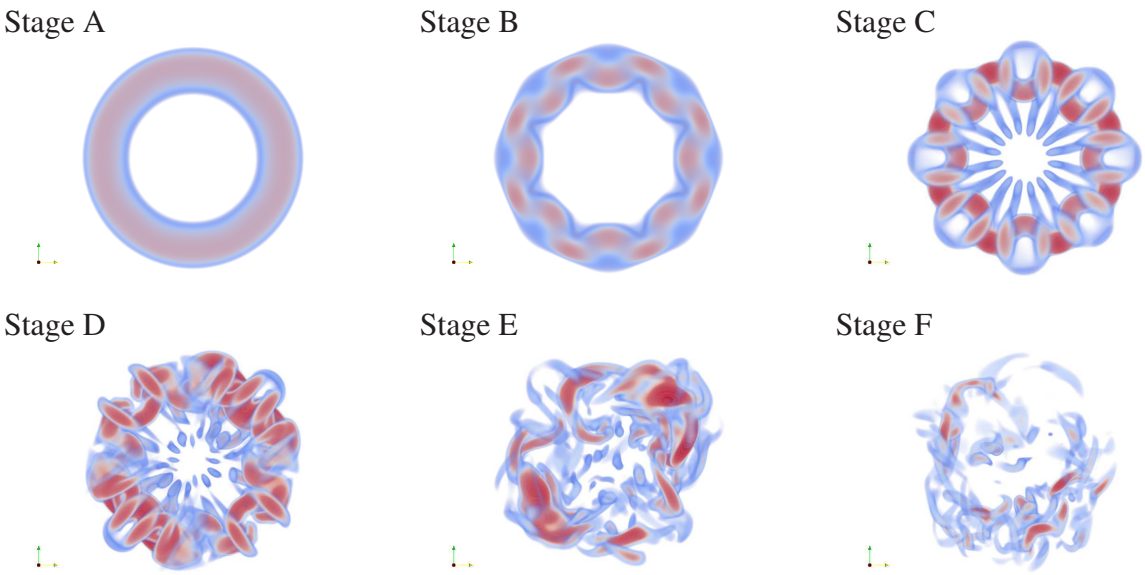

Figure I-1: The magnitude of the vorticity at five different time stages of a single vortex ring simulated at a circulation based Reynolds number of 10.000. The red and blue colour indicate regions of high and low vorticity, respectively. A) $t\,\Gamma/D^2 = 15.3$ The initial vortex ring. B) $t\,\Gamma/D^2 = 31.1$ The vortex ring becomes unstable. C) $t\,\Gamma/D^2 = 39.9$ Secondary structures appear around the core. D) $t\,\Gamma/D^2 = 46.7$ The vortex core becomes highly irregular. E) $t\,\Gamma/D^2 = 55.6$ The vortex ring ruptures into turbulence. F) $t\,\Gamma/D^2 = 66.4$ The turbulence decays accordingly to viscous effects.

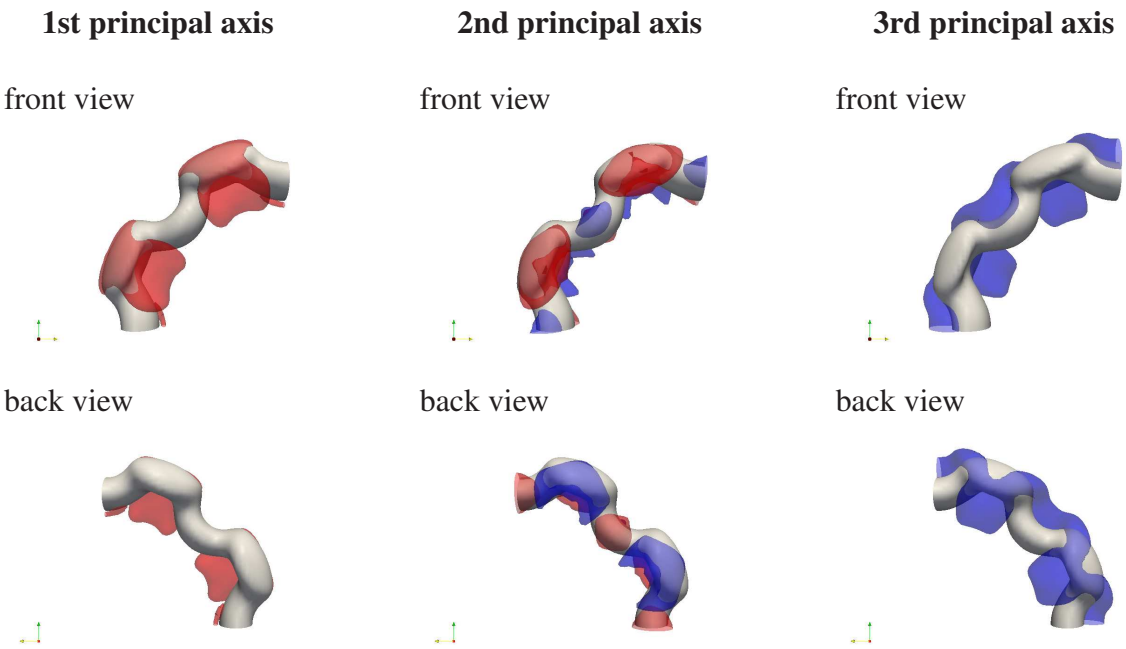

Figure I-2: Analysis of the three components contributing to the material derivative of the enstrophy in Eq. (I-15) related to each of the principal axes of the strain rate tensor for stage B shown in Fig. I-1. The red iso-surfaces represents a positive change of enstrophy density, the blue iso-surfaces represents a negative change of enstrophy density, and the white iso-surfaces represents the vortex ring core which is used as a spatial reference.

by different components the enstrophy equation (Eq. (I-15)). It is seen that the vortex core is dominated by the component related to the second eigenvalue whereas the secondary vortex structures are dominated by the components related to the first and third eigenvalue of the strain rate tensor.

This tendency is also shown in Fig. I-3 where the probability of the vorticity alignment and deformation mode of the strain rate tensor are shown for the six different stages. It is seen that in the early stages the clear majority of the vorticity is aligned with the principal axis related to the intermediate eigenvalue λ_2 with both disk and tube deformation. As the vortex ring becomes unstable and secondary vortex structures are formed a larger part of the vorticity is aligned with the first and third eigenvalues. The correlation of the vorticity alignment with the first and third eigenvectors and the secondary vortex structures corresponds to what is shown in Fig. I-2.

In the late stages where the topology of the vortex ring is disrupted it is seen that the vast majority of the vorticity is aligned with the principal axes which is related to either the first or the second eigenvalue and the flow deformation is solely that of a disk deformation. The results at this stage corresponds well with that reported by (Ashurst et al., 1987) for the alignment of vorticity in free turbulence.

It is here emphasised that the presented analysis regards the dynamics of the local vorticity and enstrophy density and does not represent the macroscopic tendencies of the vorticity field. In this context it is quite noticeable that at no point was it observed that the vorticity was aligned with the stretching axis of a tube-like deformation (i.e. the alignment with the principal axis of the largest eigenvalue λ_1 combined with a deformation mode of 1). This indicates that

the stretching of vortex tubes, which is often associated with the energy cascade from larger to smaller flow scales, is entirely a macroscopic behaviour. It is noted that if this observation of the microscopic behaviour is indeed a consequence of the flow kinematics, it prevents the vorticity field to develop singularities which in turn prevents the blow-up of the Euler equations (Beale et al., 1984).

I-4 Conclusion

A high order particle-mesh based vortex method has been presented for the simulation of vortical flows with free-space boundary conditions. The high order was achieved by a high order regularisation of the vorticity field and a re-projection of the vorticity field was applied to ensure a divergence-free vorticity field. The presented vortex method was used to simulate the evolution, instability and break-down of a single vortex ring. By considering the angular momentum and rotational kinetic energy of a infinitesimal material volume of fluid a novel analysis of the vortex dynamics of a single vortex ring was made. The analysis showed that the different stages of the vortex ring break-down display clear differences in the dynamics of the enstrophy density. A field analysis of the dynamics of the enstrophy density furthermore showed different tendencies for primary and secondary vortex structures indicating a strong relation to the topology of the vortical structures.

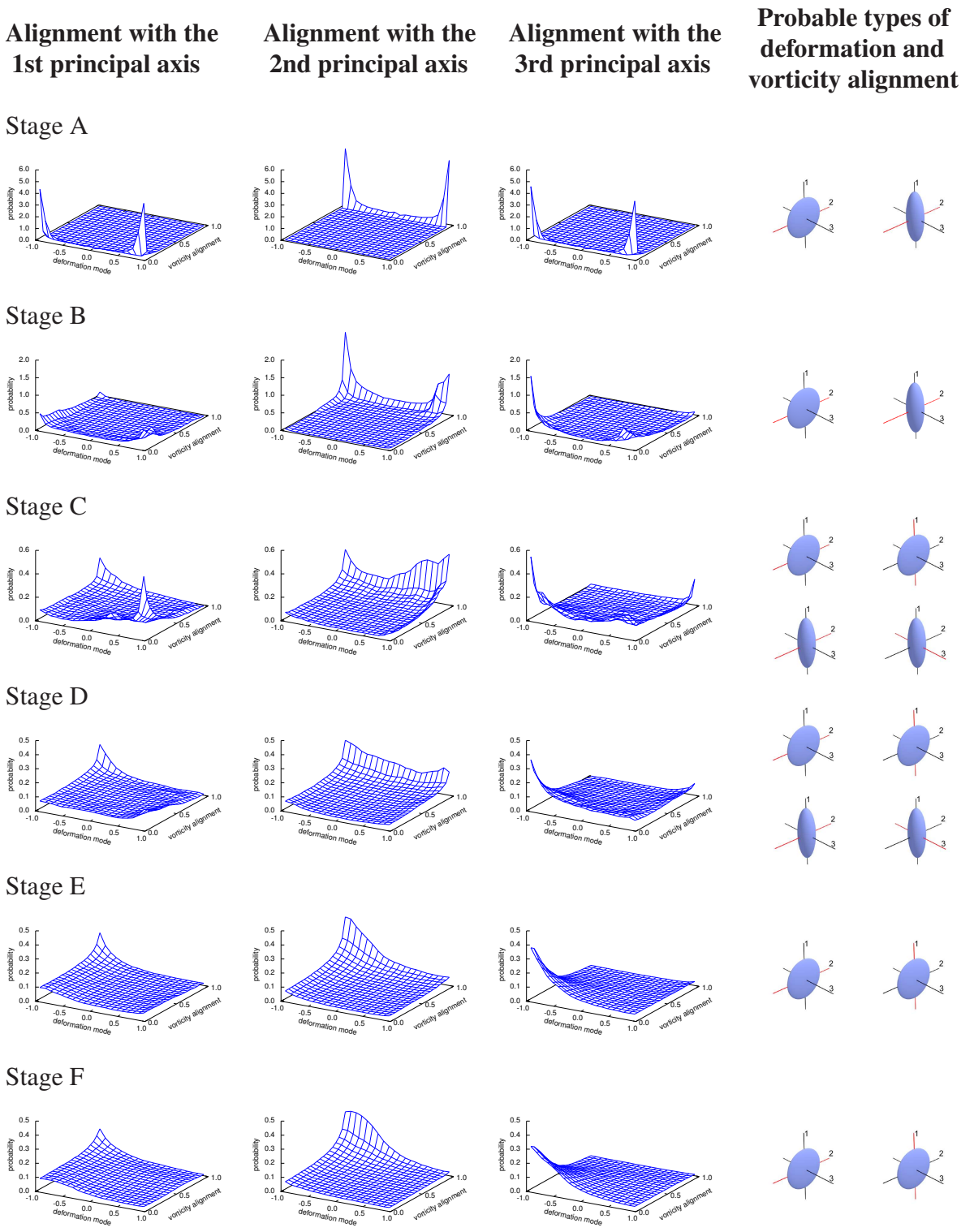

Figure I-3: Investigation of the deformation of the vorticity field for the six stages shown in Fig. I-1. Surface plots: Alignment of vorticity with the principal axis of the strain rate tensor for the different deformation modes. A negative deformation mode corresponds to a disc deformation whereas a positive deformation mode corresponds to a tube deformation. The right most column shows the types of fluid deformation (tube or disc) which is present at the given stages. Here the red axis indicates the alignment of the vorticity vector.

Article II

Iterative Brinkman penalisation for re-meshed vortex methods

Mads Mølholm Hejlesen[1], Petros Koumoutsakos[2],
Anthony Leonard[3], Jens Honoré Walther[1,2]

[1]Department of Mechanical Engineering, Technical University of Denmark, Building 403, DK-2800 Kgs. Lyngby, Denmark

[2]Computational Science and Engineering Laboratory, ETH Zürich, Clausiusstrasse 33, CH-8092 Zürich, Switzerland

[3]Division of Engineering and Applied Science, California Institute of Technology, 1200 E California Blvd., CA 91125 Pasadena, USA

This chapter consists of a modified version of the published journal article:
Iterative Brinkman penalisation for re-meshed vortex methods. J. Comput. Phys.,280:547–562, 2015.

Abstract

A novel iterative implementation of the Brinkman penalisation method is introduced for the enforcement of a fluid-solid interface in re-meshed vortex methods. The iterative scheme is shown to improve the enforcement of fluid-solid interfaces and also allow the simulation to perform significantly larger time steps, than what is customary for the Brinkman penalisation method. The improved accuracy of the iterative method is demonstrated by considering challenging benchmark problems such as an impulsively started flow past a cylinder and a flat plate normal or inclined to the flow. The iterative penalisation method is showed to enhance the quality of the solution by Brinkman penalisation significantly for simulations of highly unsteady flows past complex geometries. The iterative penalisation method thus improves both the qualitative enforcement of the fluid-solid interface as well as the computational cost of the original method, while maintaining the capability of the method to handle complex geometries.

II-1 Introduction

Simulations of bluff body flows using vortex methods have traditionally been associated with the computation of the vorticity flux, via boundary element methods (BEM), for the enforcement of the fluid-solid interfaces (Koumoutsakos and Leonard, 1995). In this context, the fluid-solid boundary conditions are enforced by first solving the potential flow problem using a vortex sheet at the fluid-solid interface. The vortex sheet (which is equivalent to a tangential slip velocity at the solid surface) is then translated into a vorticity flux in order to enforce the

no-slip boundary condition (Koumoutsakos et al., 1994).

The particle velocity can be computed by solving the Poisson equation using the Fast Multipole (Greengard and Rokhlin, 1987) or particle-mesh based methods (as in vortex-in-cell algorithms (Christiansen, 1973)). A combination of the boundary element method and the vortex-in-cell method was presented in (Morgenthal and Walther, 2007) using a particle-particle particle-mesh ($\mathrm{P^3M}$) algorithm (Walther, 2003) to correct the vortex-in-cell method with the vorticity obtained from the BEM.

The distortion of the particle locations can render vortex methods inaccurate. In order to amend this problem, re-meshing was introduced by (Koumoutsakos and Leonard, 1995; Koumoutsakos, 1997). In re-meshed vortex methods particles are advected with the velocity of the flow field. When particle locations get distorted their strength is interpolated onto mesh nodes, which become the particles to be advected in the next iteration.

The drawback of using re-meshing is that spurious vorticity can be introduced in the interior of the body. A remedy is to use locally one-sided interpolation or body fitted grids (Koumoutsakos and Leonard, 1995; Koumoutsakos and Shiels, 1996; Cottet et al., 2000). However both of these approaches have limited applicability. In order to overcome this difficulty for complex, deforming geometries, in recent years a number of efforts have combined the Brinkman penalisation techniques (Angot et al., 1999; Kevlahan and Ghidaglia, 2001) with re-meshed vortex methods (Coquerelle and Cottet, 2008; Rossinelli et al., 2010; Rasmussen et al., 2011; Gazzola et al., 2011, 2014). These simulations have demonstrated the capability of the penalisation method to produce results in good agreement with benchmark simulations. A significant drawback of these methods however, is that they impose a stringent time step on advancing the flow field to accurately capture vorticity generation at the boundary.

Here we propose a remedy to this situation by using an iterative scheme that ensures the accurate generation of vorticity at the boundary within each time step of the penalty method. We demonstrate the improvement in accuracy over the classical method, using a number of challenging benchmark problems, such as flow past an impulsively started cylinder and normal to a thin flat plate.

II-2 Methodology

II-2.1 Governing equations and Numerical Method

The velocity-vorticity form of the two-dimensional Navier-Stokes equations can be expressed in a Lagrangian reference frame as:

$$\frac{d\boldsymbol{x}}{dt} = \boldsymbol{v} \qquad \text{and} \qquad \frac{d\boldsymbol{\omega}}{dt} = \nu \boldsymbol{\nabla}^2 \boldsymbol{\omega}. \tag{II-1}$$

where ν is the kinematic viscosity, and the vorticity $\boldsymbol{\omega}$ is defined as the curl of the velocity field $\boldsymbol{\omega} = \boldsymbol{\nabla} \times \boldsymbol{v}$. The velocity field $\boldsymbol{v}$ can be obtained for an incompressible flow by solving the Poisson equation:

$$\boldsymbol{\nabla}^2 \boldsymbol{v} = -\boldsymbol{\nabla} \times \boldsymbol{\omega}. \tag{II-2}$$

We discretise the governing equations using the re-meshed vortex method (Koumoutsakos, 1997). The right-hand-sides of Eqs. (II-1) are evaluated by first interpolating the strength of the

particles (denoted by sub-script p) to a uniform mesh (denoted by sub-script m) by:

$$\boldsymbol{\omega}_m = \sum_p^N \boldsymbol{\omega}_p W\left(\frac{\boldsymbol{x}_p - \boldsymbol{x}_m}{h}\right). \tag{II-3}$$

Here $W(x)$ is the interpolation kernel and h the grid spacing of the mesh. In the present work a fourth order B-spline kernel is used: $W(\boldsymbol{x}) = M_4'(x)M_4'(y)$ which results in a third order accurate interpolation (Monaghan, 1985), where:

$$M_4'(x) = \begin{cases} 0 & \text{for} \quad 2 < |x| \\ \frac{1}{2}(2-|x|)^2(1-|x|) & \text{for} \quad 1 < |x| \leq 2 \\ 1 - \dfrac{5|x|^2}{2} + \dfrac{3|x|^3}{2} & \text{for} \quad |x| \leq 1 \end{cases} \tag{II-4}$$

We solve the Poisson equation for the velocity (Eq. (II-2)) using the high order Poisson solver of (Hejlesen et al., 2013). Here, the velocity is obtained using Fast Fourier Transforms (FFTs) on the mesh where free-space boundary conditions are obtained by zero padding the domain (Hockney and Eastwood, 1988; Chatelain and Koumoutsakos, 2010). In Fourier space the free-space Poisson may thus be solved by:

$$\widehat{\boldsymbol{v}} = \widehat{\boldsymbol{K}} \times \widehat{\boldsymbol{\omega}}. \tag{II-5}$$

Here $\widehat{\cdot}$ denotes the Fourier coefficients and $\boldsymbol{K}$ is the regularised Green's function solution corresponding to Eq. (II-2) by Eq. (II-5). In the present study we use a regularisation by a 4-th order Gaussian smoothing by which we get (Hejlesen et al., 2013) the 2D regularised Green's function:

$$\boldsymbol{K}(\boldsymbol{x}) = -\frac{1}{2\pi|\boldsymbol{x}|^2}\left(1 - \left(1 - \frac{|\boldsymbol{x}|^2}{2\sigma^2}\right)\exp\left(\frac{-|\boldsymbol{x}|^2}{2\sigma^2}\right)\right)\begin{pmatrix} x \\ y \end{pmatrix} \tag{II-6}$$

Here σ is the Gaussian smoothing length where the relation of $\sigma = 2h$ is chosen accordingly to (Hejlesen et al., 2013).

II-2.2 Brinkman penalisation of incompressible viscous flow

The penalisation method enforces the solid boundary condition on the surface of a body in an incompressible flow (Angot et al., 1999) by introducing a source term localised around the surface of the body. The velocity of the flow $\boldsymbol{v}$ is modified by the penalisation term as:

$$\frac{\partial \boldsymbol{v}}{\partial t} = \lambda\left[\chi(\mathbf{v} - \tilde{\boldsymbol{v}})\right]. \tag{II-7}$$

where $\mathbf{v}$ denotes the velocity of the body and $\tilde{\boldsymbol{v}}$ denotes the velocity field of the flow prior to penalisation i.e. from the solution of Eq. (II-2). The penalisation parameter λ has units of reciprocal time and is formally equivalent to a porosity of the body. We denote by χ the characteristic function which defines the region of active penalisation:

$$\chi = \begin{cases} 1 & \boldsymbol{x} \in S, \\ 0 & \boldsymbol{x} \in F. \end{cases} \tag{II-8}$$

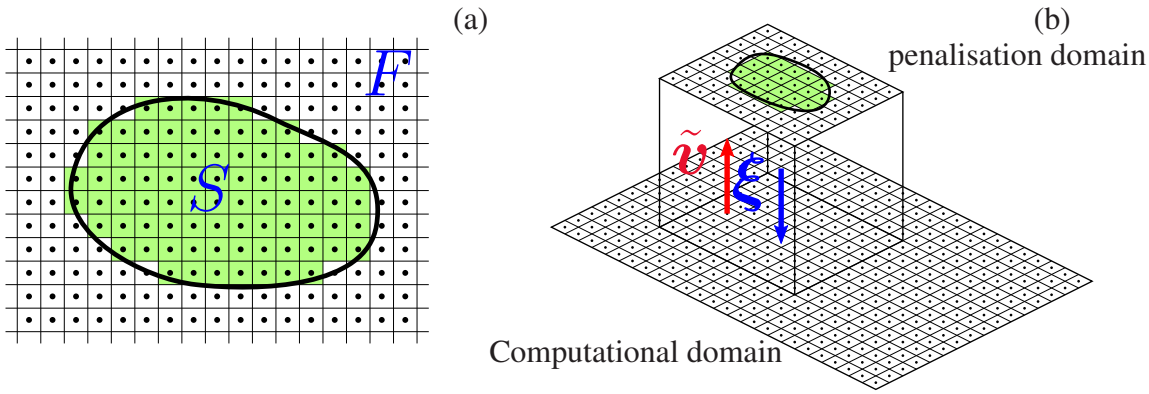

Figure II-1: Schematic of the computational domain. (a) The solid is discretised onto the Cartesian grid by penalising the mesh cells (S) that fall inside the solid surface (black curve). F denotes the fluid region. The • mark the center of the mesh cells. (b) The iterative penalisation annihilates the residual velocity ($\mathbf{v}_0$) through the creating of image vorticity $\boldsymbol{\xi}$. The iteration requires solution of the Poisson equation and is performed on the minimal "penalisation domain" surrounding the solid.

Here S denotes the mesh cells occupied by the solid and F the mesh cells occupied by the fluid cf. Fig. II-1.

As proposed by (Coquerelle and Cottet, 2008) penalisation can be implemented using a splitting algorithm. Hence the velocity field obtained from the non-penalised governing equations is corrected with the penalisation term which can be evaluated independently. Using an Euler time integration scheme for Eq. (II-7), the correction can be evaluated either explicitly or implicitly by:

$$\boldsymbol{v}_{exp} = \tilde{\boldsymbol{v}} + \lambda\,\delta t\,\chi(\mathbf{v} - \tilde{\boldsymbol{v}}) \qquad \text{or} \qquad \boldsymbol{v}_{imp} = \frac{\tilde{\boldsymbol{v}} + \lambda\,\delta t\,\chi\mathbf{v}}{1 + \lambda\,\delta t\,\chi}, \tag{II-9}$$

respectively.

Previous implementations of the Brinkman penalisation in the re-meshed vortex method (Rossinelli et al., 2010; Rasmussen et al., 2011; Gazzola et al., 2011) reports the need for an explicitly mollified characteristic function. In this work we do not mollify the characteristic function explicitly as the velocity field is ensured to be sufficiently smooth ($\boldsymbol{v} \in C^2$) by the use of the 4-th order regularisation cf. Sec. II-2.1. Thus we avoid having to impose an additional mollification of the flow field close to the solid interface.

The penalisation term can be expressed in the vorticity formulation (Kevlahan and Ghidaglia, 2001) as:

$$\frac{\partial \boldsymbol{\omega}}{\partial t} = \boldsymbol{\nabla} \times [\lambda\,\chi(\mathbf{v} - \tilde{\boldsymbol{v}})] \tag{II-10}$$

which is obtained by recalculating the vorticity from $\boldsymbol{\omega} = \boldsymbol{\nabla} \times \boldsymbol{v}$ using the penalised velocity of Eq. (II-9).

The vorticity form of the penalisation can be implemented either by an implicit (Coquerelle and Cottet, 2008; Rossinelli et al., 2010; Gazzola et al., 2011) or explicit evaluation (Rasmussen et al., 2011) of the velocity. (Rasmussen et al., 2011) furthermore introduced a semi-implicit method by choosing the penalisation parameter $\lambda = 1/\delta t$. In this way the expression may be viewed as simple linear interpolation between the velocity fields $\mathbf{v}$ and $\tilde{\boldsymbol{v}}$ cf. (Rasmussen et al.,

2011), thus:

$$\boldsymbol{v} = (1-\chi)\tilde{\boldsymbol{v}} + \chi\mathbf{v}. \tag{II-11}$$

The explicit Euler method enforces a stability constraint on the product of the time step δt and the penalisation parameter λ. A stability analysis gives the region of absolute stability as $0 \leq \lambda\delta t \leq 2$. Thus we may generalise the method of (Rasmussen et al., 2011) by using $\lambda = \alpha/\delta t$, which is subject to the constraint of $0 \leq \alpha \leq 2$. For this generalisation we obtain:

$$\boldsymbol{v} = (1-\alpha\chi)\tilde{\boldsymbol{v}} + \alpha\chi\mathbf{v} \qquad \text{and} \qquad \boldsymbol{v} - \tilde{\boldsymbol{v}} = \alpha\chi(\mathbf{v} - \tilde{\boldsymbol{v}}). \tag{II-12}$$

It was pointed out by (Rasmussen et al., 2011) that replacing the vorticity field by the finite difference evaluation of the vorticity introduces additional numerical diffusion of the vorticity field. To avoid this, the local correction of the vorticity field can be added to the vorticity field rather than replacing it by the curl of the penalised velocity field. In the present work, we update the vorticity using the expression:

$$\boldsymbol{\omega} = \tilde{\boldsymbol{\omega}} + \boldsymbol{\nabla} \times (\boldsymbol{v} - \tilde{\boldsymbol{v}}) = \tilde{\boldsymbol{\omega}} + \alpha\,\boldsymbol{\nabla} \times (\chi(\mathbf{v} - \tilde{\boldsymbol{v}})). \tag{II-13}$$

Here $\tilde{\boldsymbol{\omega}}$ denotes the non-corrected vorticity field prior to the penalisation.

II-2.3 An iterative Brinkman penalisation method for incompressible viscous flow

While the velocity field is globally related to the vorticity through the Poisson equation, the penalisation introduces only a local relation between velocity and vorticity. This inconsistency can be attributed to the non-consistent handling of the flow kinematics and the no-through flow boundary condition by the classical Brinkman penalisation technique.

Here we propose to compute the vorticity field from the penalty term and use it in turn to compute an updated velocity field, solving the corresponding Poisson equation. We iterate this process so that we obtain a kinematic consistency of the flow. The proposed *iterative Brinkman penalisation* requires solving the Poisson equation a number of times for each time step. In the following we will show that this cost can be reduced by solving the Poisson equation only on a subset of the computational domain and by distinguishing between the vorticity of the flow field and the vorticity generated by the penalisation.

In the penalised region, after each time step the velocity field computed by the flow solver ($\tilde{\boldsymbol{v}}$) may not comply with the imposed velocity field in the body ($\mathbf{v}$). We compensate for this error through an iterative procedure that computes a vorticity field ($\boldsymbol{\xi}$) that induces a velocity field ($\boldsymbol{v}_\xi$) such that:

$$\chi(\tilde{\boldsymbol{v}} + \boldsymbol{v}_\xi) = \chi\,\mathbf{v} \qquad \Rightarrow \qquad \chi\,\boldsymbol{v}_\xi = \chi(\mathbf{v} - \tilde{\boldsymbol{v}}) = \chi\,\mathbf{v}_0 \tag{II-14}$$

where $\mathbf{v}_0 = \mathbf{v} - \tilde{\boldsymbol{v}}$ is the velocity that needs to be penalised in order to enforce the given velocity $\mathbf{v}$ within the penalised region. The velocity $\mathbf{v}_0$ can be calculated outside the iterative loop after which it suffices to solve the unbounded Poisson equation (cf. Sec. II-2.1) in a small domain bounding the geometry cf. Fig. II-1b. The domain extends slightly beyond the geometry to ensure that the applied numerical schemes used to calculate the penalisation vorticity are fully supported on the mesh. For the results presented in this manuscript we use a second order

finite difference scheme. In this way the computational work of the iterative penalisation is significantly reduced as it becomes independent of the extent of the total vorticity field.

We evaluate the convergence of the iteration by measuring the total penalisation force. From Eq. (II-7) it is seen that the total force exerted on the fluid is given by the volume integral of the penalisation term. Hence the total force experienced by the simulated body is:

$$\boldsymbol{F} = -\rho \int_V \frac{D\boldsymbol{v}}{Dt}\, dV = -\rho \int_V \lambda\chi(\mathbf{v} - \tilde{\boldsymbol{v}})\, dV \tag{II-15}$$

which for an ideal penalisation gives the total aerodynamic force on a solid body immersed in the flow. In case of $\lambda = \alpha/\delta t$, Eq. (II-15) becomes:

$$\boldsymbol{F} = -\rho\alpha \int_V \chi \frac{\mathbf{v} - \tilde{\boldsymbol{v}}}{\delta t}\, dV. \tag{II-16}$$

The flow induced forces can alternatively be calculated by the temporal change in the vorticity moment of the flow cf. Wu (Wu, 1981):

$$\boldsymbol{F} = -\rho \frac{d}{dt} \int_V \boldsymbol{x} \times \boldsymbol{\omega}\, dV. \tag{II-17}$$

Again we make use of the decomposition of the vorticity field and notice that the force can be calculated by considering the penalisation vorticity only:

$$\boldsymbol{F} = -\rho \frac{d}{dt} \int_V \boldsymbol{x} \times \boldsymbol{\xi}\, dV \tag{II-18}$$

which for the iterative penalisation can be written as a sum of the force contributions ($\boldsymbol{\delta F}^k$) from the penalisation vorticity generated ($\boldsymbol{\delta\xi}^k$) in each iteration step k:

$$\boldsymbol{F} = \sum_{k=1}^{N_{it}} \boldsymbol{\delta F}^k \qquad \text{where} \qquad \boldsymbol{\delta F}^k = -\rho \frac{1}{\delta t} \int_V \boldsymbol{x} \times \boldsymbol{\delta\xi}^k\, dV. \tag{II-19}$$

A convergence criteria can thus be stated as $\|\boldsymbol{\delta F}^k\|/\|\boldsymbol{F}^k\| < \varepsilon$ where ε is the relative tolerance of the penalisation force. For the present study emphasis is placed on force comparison in different flow cases by which we have used the normalised change in the force as a natural criteria of convergence. Alternatively, we propose another convergence criteria based on the normalised change in enstrophy $\mathcal{E}$ of the penalisation vorticity:

$$\frac{|\mathcal{E}^k - \mathcal{E}^{k-1}|}{\mathcal{E}^k} < \varepsilon \qquad \text{where} \qquad \mathcal{E}^k = \int_V \boldsymbol{\xi}^k \cdot \boldsymbol{\xi}^k\, dV. \tag{II-20}$$

This criteria has the benefit of being a measure of the norm and is thus formally better suited as a convergence criteria. Similarly, a norm measure of the residual velocity inside the penalisation region may also be chosen as the convergence criteria. The residual velocity however, is not a suitable convergence criteria for investigating an impulsively started flow as we will show later in Sec. II-3.1. An outline of the iterative penalisation algorithm is shown in Fig. II-2.

We emphasise that the penalisation force evaluated by Eq. (II-16) or Eq. (II-19) is based on the Euler time integration scheme and is thus inherently first order accurate. Due to this, a

Algorithm outline of the iterative penalisation
- Obtain the non-penalised velocity $\tilde{\boldsymbol{v}}$ by solving the Poisson equation on the full domain.
- In the penalisation sub-domain store the velocity that needs to be penalised:
$\mathbf{v}_0 = \mathbf{v} - \tilde{\boldsymbol{v}}$.
- Initialise the iterative fields in the penalisation sub-domain: $\boldsymbol{\xi}^0 = \mathbf{0}$, $\boldsymbol{v}_\xi^0 = \mathbf{0}$, and $\boldsymbol{F}^0 = \mathbf{0}$, where the superscript refers to the iteration count.
for $k = 1, N_{it}$ **do**
  - Calculate the increment of the penalisation vorticity: $\boldsymbol{\delta\xi}^k = \alpha\,\boldsymbol{\nabla} \times [\chi(\mathbf{v}_0 - \boldsymbol{v}_\xi^{k-1})]$.
  - Update the penalisation vorticity: $\boldsymbol{\xi}^k = \boldsymbol{\xi}^{k-1} + \boldsymbol{\delta\xi}^k$.
  - Calculate the new penalisation velocity field from the Poisson equation using free space boundary conditions: $\nabla^2 \boldsymbol{v}_\xi^k = -\boldsymbol{\nabla} \times \boldsymbol{\xi}^k$.
  - Calculate the added penalisation force of the iteration step: $\boldsymbol{\delta F}^k = -\rho \frac{1}{\delta t} \int \boldsymbol{x} \times \boldsymbol{\delta\xi}^k \, dV$.
  - Calculate the total induced penalisation force: $\boldsymbol{F}^k = \boldsymbol{F}^{k-1} + \boldsymbol{\delta F}^k$.
  if $\|\boldsymbol{\delta F}^k\| / \|\boldsymbol{F}^k\| < \varepsilon$ **then** Break
- Compute the total vorticity field on the full domain: $\boldsymbol{\omega} = \tilde{\boldsymbol{\omega}} + \boldsymbol{\xi}^k$.
- Re-calculate the velocity field on the full domain: $\nabla^2 \boldsymbol{v} = -\boldsymbol{\nabla} \times \boldsymbol{\omega}$.

Figure II-2: Outline of the iterative Brinkman penalisation algorithm.

deviation may be seen from the force calculated by Eq. (II-17) if a higher order time integration is used to evolve the particle vorticity cf. Eq. (II-1). In the presented results we use an Euler scheme to evolve the particle vorticity (Eq. (II-1)) whereas the trajectory of each particle is evaluated using the mid-point 2nd order Runge-Kutta scheme. In this way, the forces calculated by Eq. (II-17) and Eq. (II-19) are consistent. Simulations were also made with higher order schemes for both equations in Eq. (II-1) (not shown). Here it was observed, that the forces calculated by the overall vorticity moment produced results in excellent agreement with the results presented in Sections II-3.1, II-3.2, and II-3.4.

The α-parameter is used to relax the incrementation of the penalisation vorticity. This is clarified by rewriting:

$$\boldsymbol{\xi} + \alpha\,\boldsymbol{\delta\xi} = (1-\alpha)\boldsymbol{\xi} + \alpha(\boldsymbol{\xi} + \boldsymbol{\delta\xi}). \tag{II-21}$$

Thus, as the penalisation is implemented iteratively until the penalisation force is converged, the penalisation parameter $\lambda = \alpha/\delta t$ is no longer a formal measure of porosity but serves instead as a relaxation factor. As observed, in Sec. II-3.1, using $1 < \alpha \leq 2$ can reduce the number of iterations needed for the convergence of the residual penalisation force.

We find that the number of iterations needed to satisfy the convergence criteria can be reduced by initially removing a large part of the image vorticity from the previous time step. Practically, the vortex particles inside the penalisation region which do not contribute to the vorticity field outside the penalisation region are discarded prior to interpolating the particle vorticity onto the mesh by Eq. (II-3). Thus, for the M_4' interpolation kernel in Eq. (II-4), particles located more than two cell lengths inside the penalisation region (equal to the stencil of the interpolation kernel) are removed. This ensures that the vorticity field outside the penalisation

region remains unaltered and the smoothness of the vorticity field, which is essential for the linear superposition of the vorticity. It is further noted that removing the image vorticity is in fact in accordance with the non-uniqueness of image vorticity cf. (Saffman, 1992).

The solution obtained by the penalisation is not subjected to any further constraint than that given by the velocity field. Consequently, the moments of the vorticity field are satisfied possibly only implicitly by the calculation of penalisation vorticity which is determined locally. This does not ensure a conservation of circulation, and furthermore, the convergence towards a unique solution is not evident. Previous studies of the vorticity based penalisation method (Coquerelle and Cottet, 2008; Rossinelli et al., 2010; Gazzola et al., 2011; Rasmussen et al., 2011) do not report on the need to satisfy the vorticity moments explicitly. However, by applying the iterative penalisation method and thereby gaining a stronger coupling of the degrees of freedom, might raise the need for an explicit handling of the conservation of the vorticity moments. We note that an additional constraint of the penalisation method e.g. from the Kelvin circulation theorem can be easily implemented in the current algorithm for the iterative penalisation. This can be done by continuously including any residual of the total vorticity field i.e. , the zero'th moment, in the calculation of the penalisation vorticity by distributing the residual vorticity onto the interior cells for each penalisation iteration.

II-3 Results

II-3.1 Impulsively started flow past a circular cylinder at Re = 9500

In this section we compare the new iterative penalisation with the classical non-iterative explicit penalisation method for the benchmark case of the impulsively started flow past a circular cylinder at Re $= 9500$. The Reynolds number, the non-dimensional time, and the drag coefficient for this case are defined by:

$$\mathrm{Re} = \frac{D\,U_\infty}{\nu}, \qquad t^* = \frac{tU_\infty}{D}, \qquad \text{and} \qquad C_D = \frac{2\boldsymbol{F}\cdot\boldsymbol{e}_x}{U_\infty D} \tag{II-22}$$

where D is the diameter of the cylinder. In order to compare with the BEM based vortex method of (Koumoutsakos and Leonard, 1995) the simulation is performed with the equivalent time step size of $\delta t^* = \delta t\, U_\infty/D = 5\cdot 10^{-3}$ and a spatial resolution given by the cell length of $\delta x/D = 1/512$.

Fig. II-4 shows the calculated streamlines and vorticity contours for the impulsively started flow past the circular cylinder at early times. The iterative penalisation method is compared to that obtained by the non-iterative penalisation method showing a clear difference between the two. The inherent problem of the non-iterative penalisation method is best illustrated by the streamlines for $t^* = 0$. Here it is observed that the non-iterative penalisation method fails to deflect the flow field around the cylinder, and the flow thus penetrates the solid boundary and remains active within the penalised region. For the iterative penalisation the flow is deflected from the first time step and the flow remains at rest within the cylinder as time progresses. At later times the two flow fields become more similar as the non-iterative penalisation method eventually succeed in deflecting the flow around the cylinder. However, a clear difference is observed for the location and shape of the vortical structures that are generated on the cylinder

boundary.

The calculated drag force for the iterative penalisation method using different convergence criteria are compared to the non-iterative penalisation method in Fig. II-5. It is seen that by using the iterative penalisation method it is possible to obtain results in good agreement with the BEM based method (Koumoutsakos and Leonard, 1995), whereas the non-iterative method fails to produce a similar result with the chosen time step. It is seen in Fig. II-5 that a significantly improved result is obtained even for large residual forces such as $\varepsilon = 10^{-1}$ and $\varepsilon = 10^{-2}$ which are achieved in $\mathcal{O}(1)$ and $\mathcal{O}(10)$ iterations, respectively cf. Fig. II-6a. It is also noticed that the results for the iterative penalisation show a consistency when the residual force $\varepsilon < 10^{-3}$. Moreover, Fig. II-6a shows that the number of iterations used to reach the convergence criteria can be increased or decreased by choosing an under-relaxation ($0 < \alpha < 1$) or an over-relaxation ($1 < \alpha \leq 2$), respectively. The resulting drag force for different values of α (not shown) is observed to vary within the range of the specified tolerated residual force ε.

Fig. II-6b demonstrates that the number of iterations can be reduced by removing a part of the image vorticity as described in Sec. II-2.3. Here, the number of iterations is approximately constant through the simulation, and consistent with the number of minimum iterations required when preserving the image vorticity cf. Fig. II-6a. We observe that the number of necessary iterations can change over different time steps when the residual velocity in the penalisation region changes significantly relative to the threshold allowed by the convergence criteria. This is observed in Fig. II-6b for the simulation using $\alpha = 0.5$ and $\varepsilon = 10^{-1}$, and was also observed for all simulations using $\alpha = 2$ and/or $\varepsilon = 10^{-4}$ which are omitted from the Fig. II-6b due to erratic behaviour. The variability on the number of penalisation iterations is also present in the calculated force (not shown). However, by choosing a lower value of the relaxation factor (α), the rate-of-change of the residual velocity in the penalisation region decreases, making the total residual velocity less varying between time steps.

The drag force which was obtained by the method, when removing image vorticity (not shown) was observed to be qualitatively equal to that obtained by the method, when the image vorticity was preserved (cf. Fig. II-5). This supports the notion that the image vorticity is not unique, and that the iterative penalisation in the present case indeed converges towards a unique external flow solution for different initial conditions.

For the computational domain shown in Fig. II-4, the additional cost of doing one penalisation iteration in the present re-meshed vortex method is less than 1 % of the total cost of a time step. Comparing with the number of penalisation iterations used to achieve convergence cf. Fig. II-6a for $\alpha = 1$, the additional work at $t^* = 3.0$ can be estimated to approximately 3 %, 6 %, 11 %, and 54 % for the tolerances $\varepsilon = 10^{-1}, 10^{-2}, 10^{-3}$, and 10^{-4}, respectively. A comparison of the computational efficiency was made, for the current test case, between the iterative penalisation method and the BEM used by the discrete vortex method of (Walther, 1994; Walther and Larsen, 1997; Rasmussen et al., 2010). It was found that for the current implementation the iterative penalisation method requires $4.3 \cdot 10^{-1}$ s per iteration whereas the linear solver of the BEM requires only $2.3 \cdot 10^{-2}$ s in total. Hence the iterative penalisation method show a large computational overhead for the current test case. However, as the BEM scales with the number of surface elements squared and the penalisation method with the volume of the solid body, this result can not be generalised to other cases in two or three dimensions.

The residual velocity inside the penalisation region is now investigated by defining the global

(a)

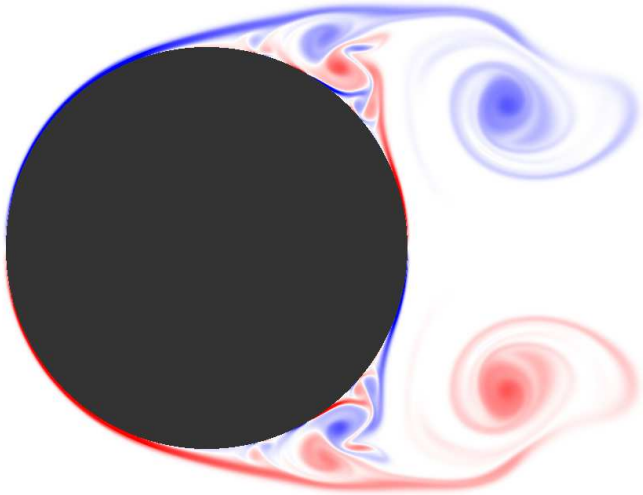

(b)

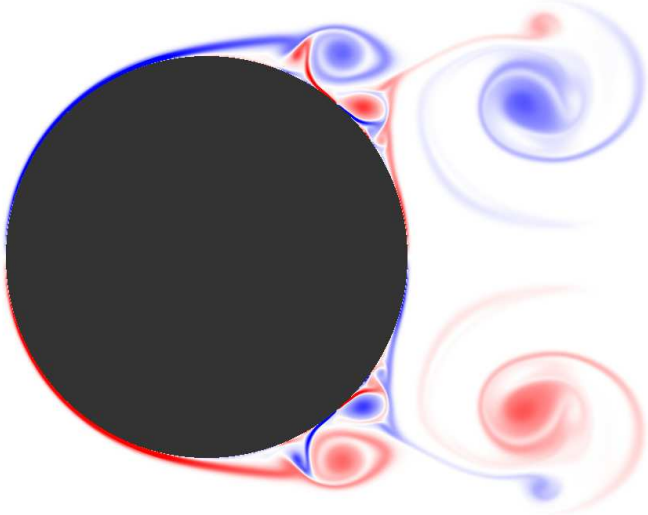

Figure II-3: The vorticity field at $t^* = 2.50$ for (a) the non-iterative penalisation and (b) the iterative penalisation method. A clear difference is noticed between the two methods.

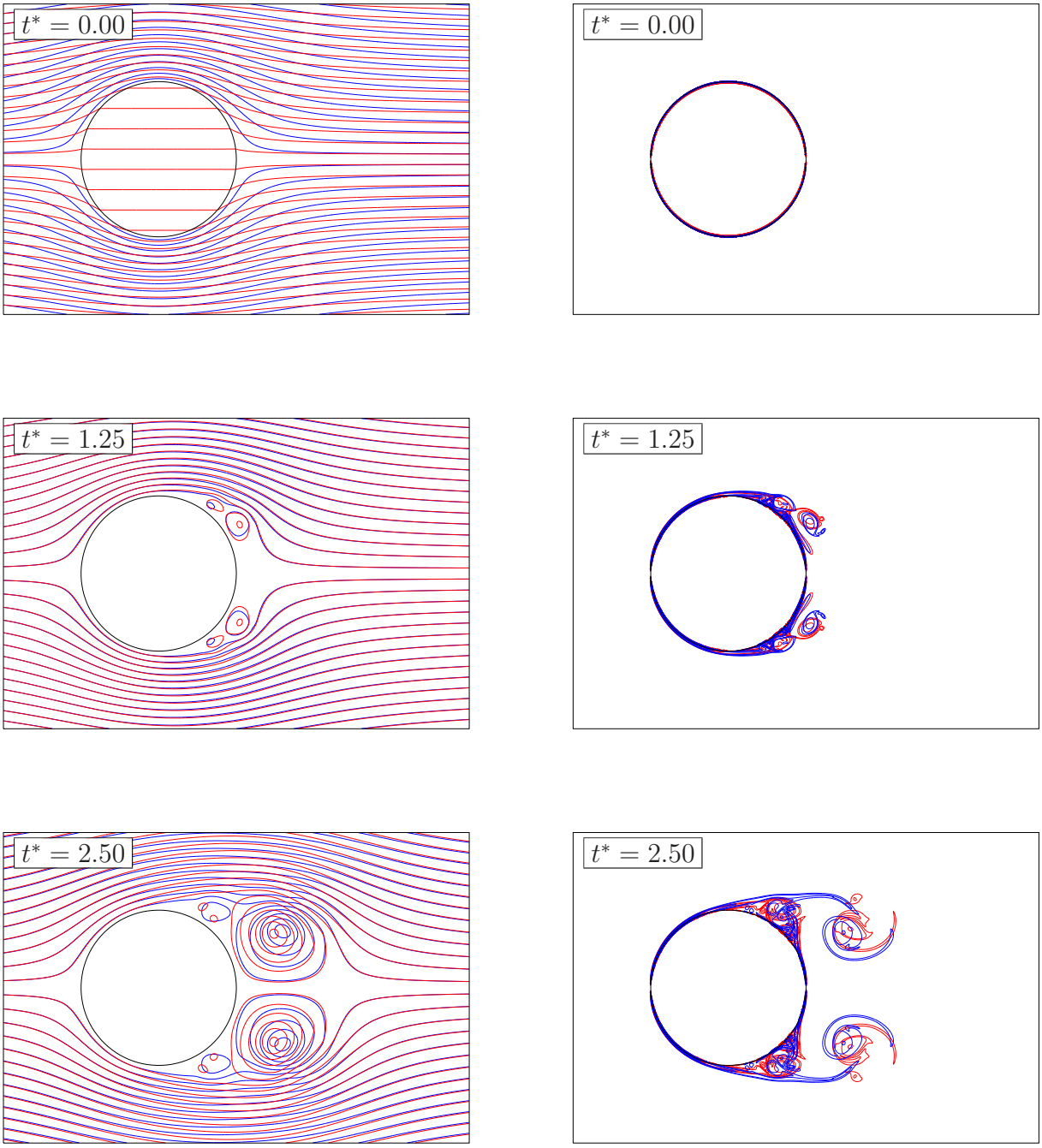

Figure II-4: Comparison of the streamlines (left) and vorticity contours (right) obtained by non-iterative penalisation (red), and iterative penalisation (blue) for an impulsively started flow past a circular cylinder. Vorticity contours are $\pm 2^i$ where $i = \{4, 5, 6, 7\}$.

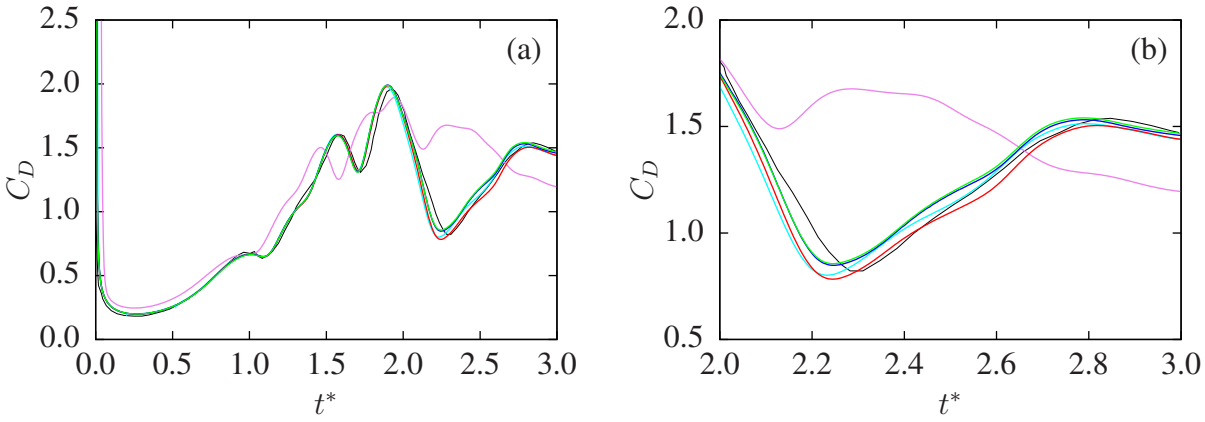

Figure II-5: The calculated drag coefficient of the impulsively started flow around a cylinder at Re $= 9500$. (a): Comparison of the iterative penalisation converged at a residual force of $\varepsilon = 10^{-1}$ (cyan), $\varepsilon = 10^{-2}$ (red), $\varepsilon = 10^{-3}$ (blue), and $\varepsilon = 10^{-4}$ (green), the non-iterative penalisation (violet), and the results of (Koumoutsakos and Leonard, 1995) (black). (b): Enlargement of the calculated drag coefficient from $t^* = 2.0$ to 3.0.

penalisation error e_2 and the maximum local penalisation error e_∞ by:

$$e_2 = \frac{1}{U_\infty}\sqrt{\frac{1}{A}\int_A \chi||\mathbf{v}-\boldsymbol{v}||^2\,dA} \qquad \text{and} \qquad e_\infty = \frac{1}{U_\infty}\left(\chi||\mathbf{v}-\boldsymbol{v}||\right)_{max}. \tag{II-23}$$

In Fig. II-7a the time history of e_2 and e_∞ is shown for different tolerances. It is here seen that both the global and the maximum local residual velocity is reduced by hardening the convergence criteria of the penalisation force. Secondly, it is noticed that for the given test case of an impulsively started flow that the residual velocity, of especially the lowest tolerances, resembles a singularity at $t^* = 0$. This of course requires a corresponding large number of penalisation iterations to fulfil the convergence criteria, which is why a measure for the residual velocity is not chosen as a convergence criteria in the present work.

Related work (Rossinelli et al., 2010; Rasmussen et al., 2011) have shown that an equally good agreement with the results of (Koumoutsakos and Leonard, 1995) can be obtained using the standard non-iterative penalisation however at a non-dimensional time step size of 10^{-4} which is 50 times smaller than that used by the iterative penalisation as well as in the reference work (Koumoutsakos and Leonard, 1995). The efficiency of the non-iterative penalisation method is therefore relying on the time step size being much smaller than the physical development of the flow. On this ground, we remark that the non-iterative penalisation method is unable to produce accurate simulations of impulsively started flow.

The inability of the non-iterative penalisation method to simulate the early phase of impulsively started flow is illustrated in Fig. II-7b. The predicted vortex sheet is compared with the analytical potential flow solution, demonstrating that the non-iterative penalisation method strongly under-predicts the strength of the vortex sheet at $t^* = 0$. It is noted that due to the specific geometry, the non-iterative penalisation method will create the correct vortex sheet by choosing an over-relaxation factor $\alpha = 2$. Doing so has been observed in the present study to give reasonable results, however this is only due to the special geometrical situation and does

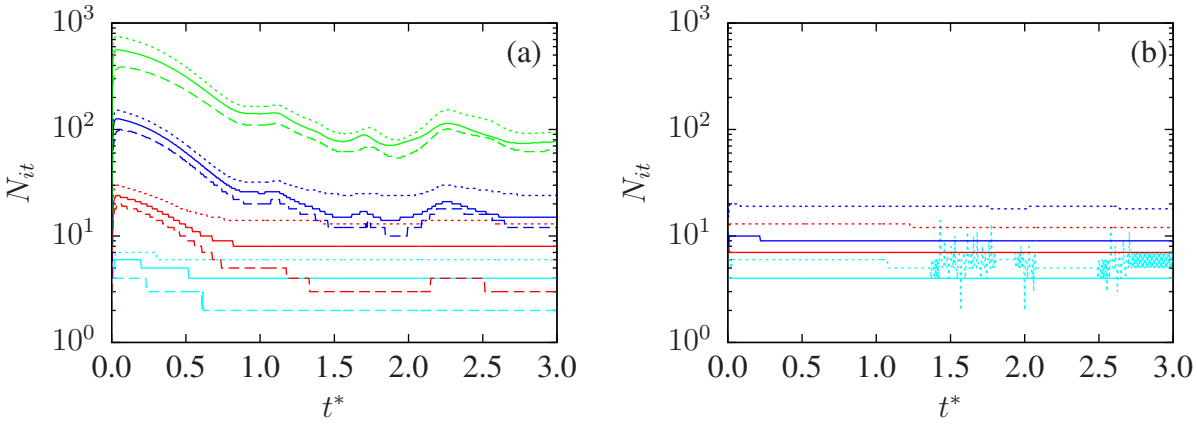

Figure II-6: The number of iterations used to reach convergence for the impulsively started flow past a cylinder at Re $= 9500$. Using a relaxation factor of: $\alpha = 0.5$ (dotted lines), $\alpha = 1.0$ (full lines), $\alpha = 2.0$ (dashed lines), and a residual force of: $\varepsilon = 10^{-1}$ (cyan), $\varepsilon = 10^{-2}$ (red), $\varepsilon = 10^{-3}$ (blue), and $\varepsilon = 10^{-4}$ (green). (a): Iterative penalisation when conserving the image vorticity of previous time steps. (b): Iterative penalisation when discarding the image vorticity before each time step.

not apply to the general case.

In Fig. II-8 the resulting surface vorticity is shown for the iterative and non-iterative penalisation method and compared to the results of (Koumoutsakos and Leonard, 1995). In the present study, the surface vorticity is obtained by interpolating the particle vorticity onto a polar mesh. The polar mesh has a radial discretisation equal to the smoothing radius ($\sigma = 2\delta x$), and a tangential discretisation of 300 mesh cells. It is seen that the iterative penalisation method again obtains a surface vorticity which is in good agreement with the results of (Koumoutsakos and Leonard, 1995), whereas a larger deviation is observed with the non-iterative penalisation method.

II-3.2 Impulsively started flow normal to a flat plate of finite thickness at Re = 1000

As mentioned earlier, the penalisation method alone does not enforce a global correction of the flow field. A consequence of this is an inherent delay in producing proper surface vorticity to enforce the no-through boundary condition. Hence the flow normal to a flat plate presents a particularly difficult test case for the penalisation method. For the impulsively started flow normal to a flat plate the Reynolds number, non-dimensional time, non-dimensional plate thickness, and the drag coefficient are defined as:

$$\mathrm{Re} = \frac{L\,U_\infty}{\nu}, \qquad t^* = \frac{tU_\infty}{L}, \qquad H^* = \frac{H}{L}, \qquad \text{and} \qquad C_D = \frac{2\boldsymbol{F}\cdot\boldsymbol{e}_x}{U_\infty L} \tag{II-24}$$

where L and H denotes the length and thickness of the plate, respectively. In this section we will investigate the flow normal to the flat plate at a Reynolds number of Re $= 1000$.

The penalisation method evidently requires a finite thickness of the geometry relative to the mesh cell length. In this section we present simulations for plate thickness of $H^* = 1/50$,

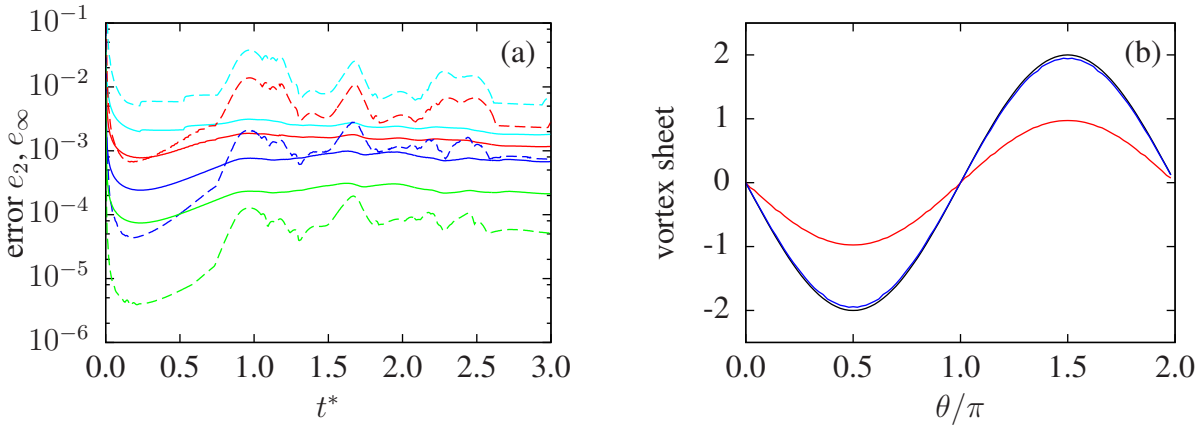

Figure II-7: a) The global penalisation error e_2 (full line) and the maximum local penalisation error e_∞ (dashed line) during the simulation of the impulsively started flow past a cylinder using a residual force convergence criteria of: $\varepsilon = 10^{-1}$ (cyan), $\varepsilon = 10^{-2}$ (red), $\varepsilon = 10^{-3}$ (blue), and $\varepsilon = 10^{-4}$ (green), and a relaxation factor of $\alpha = 1.0$. b) The calculated vortex sheet at $t^* = 0$ for the non-iterative penalisation method (red) and the iterative penalisation method (blue) compared to the exact vortex sheet for the potential flow $-2\sin(\theta)$ (black).

$1/100$, and $1/200$ which, by using a spatial resolution of $\delta x/L = 1/400$, corresponds to a plate thickness of 8, 4 and 2 cell lengths, respectively. Here the boundary is located between two mesh cells in order to ensure that the effective thickness of the simulated penalisation corresponds to the specified plate thickness. The time step size is chosen as $\delta t^* = \delta t\, U_\infty/L = 10^{-3}$ in order to show the comparability of the method to that of (Koumoutsakos and Shiels, 1996) who presented particle vortex method simulation using a BEM for an infinitely thin plate. For the iterative penalisation method the tolerance of the residual force was set to $\varepsilon = 10^{-3}$ and a convergence was generally achieved in approximately 140, 220, and 320 penalisation iterations per time step for the plates of $H^* = 1/50,\ 1/100$, and $1/200$, respectively.

The streamlines and vorticity contours for the calculated impulsively started flow normal to a flat plate of $H^* = 1/50$ is shown in Fig. II-9. Again it is clearly observed by the streamlines for $t^* = 0$ that the non-iterative penalisation method is unable to produce the correct flow at early times.

In Fig. II-10 the calculated drag coefficients of the simulations are shown for plates of different values of H^*. Here the drag coefficient calculated at early times are compared to calculations performed with the discrete vortex method of (Walther, 1994; Walther and Larsen, 1997; Rasmussen et al., 2010) using BEM for the potential part of the flow. Again a clear difference is noticed between the non-iterative and the iterative penalisation method with the iterative method showing excellent agreement to the results of the BEM method of Walther.

We observe that the finite plate thickness has a significant influence on the drag coefficient in the start-up phase of the flow. This is explained by investigating the vorticity at the tip of the plate as shown in Fig. II-11 for the iterative penalisation. Here, a separation angle can be estimated by considering the interface between positive and negative vorticity at the top of the plate. The separation angle at the plate tip reflects the magnitude of the change in flow momentum i.e. the drag force experienced by the plate. For the plate of $H^* = 1/200$ it is

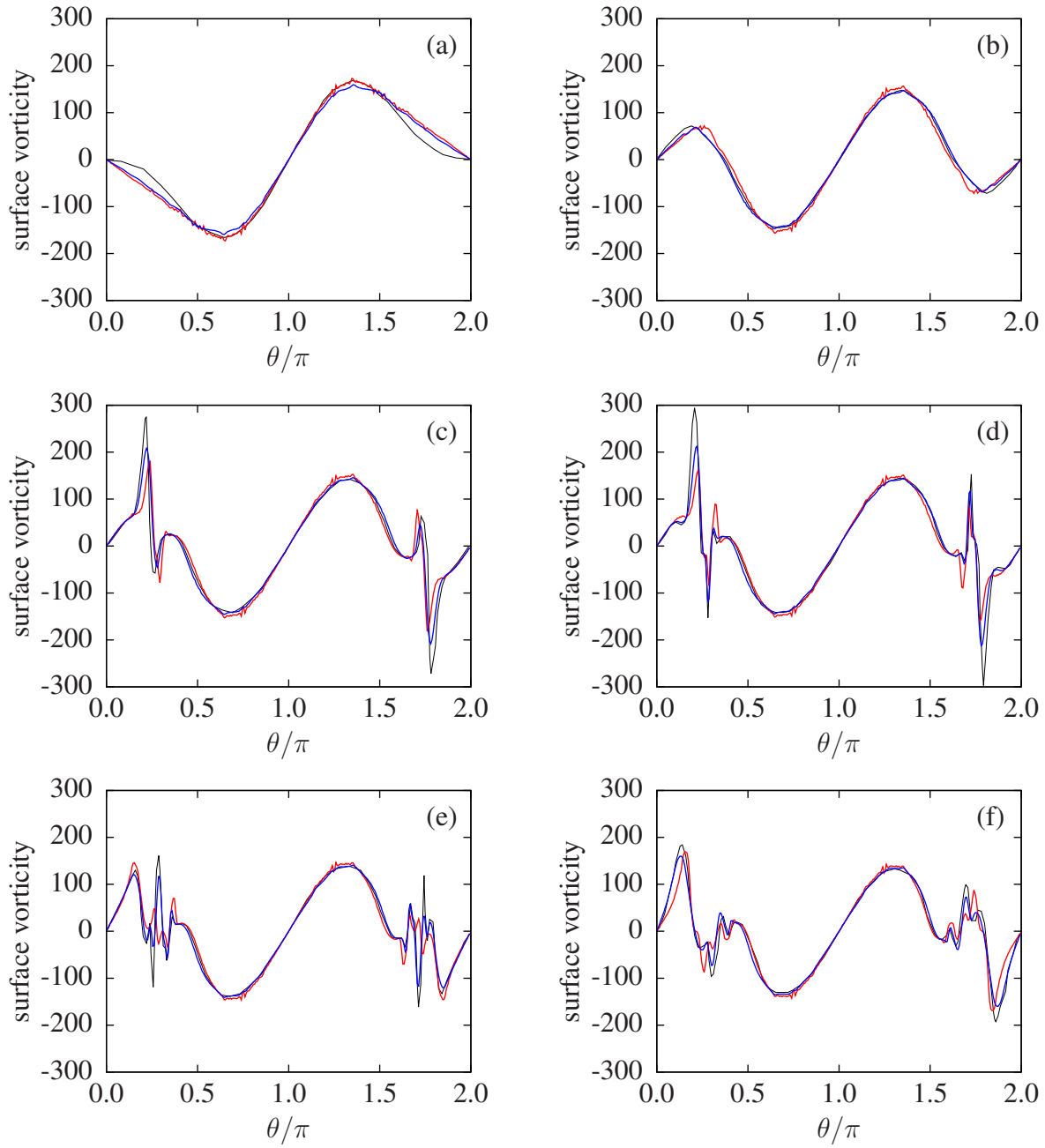

Figure II-8: The angular (θ) distribution of the surface vorticity of the circular cylinder at Re $=$ 9500 for the non-iterative, penalisation (red) and the iterative penalisation (blue) compared to the results of (Koumoutsakos and Leonard, 1995) (black). (a): $t^* = 0.2$ (b): $t^* = 0.6$ (c): $t^* = 0.9$ (d): $t^* = 1.0$ (e): $t^* = 1.3$ (f): $t^* = 1.6$.

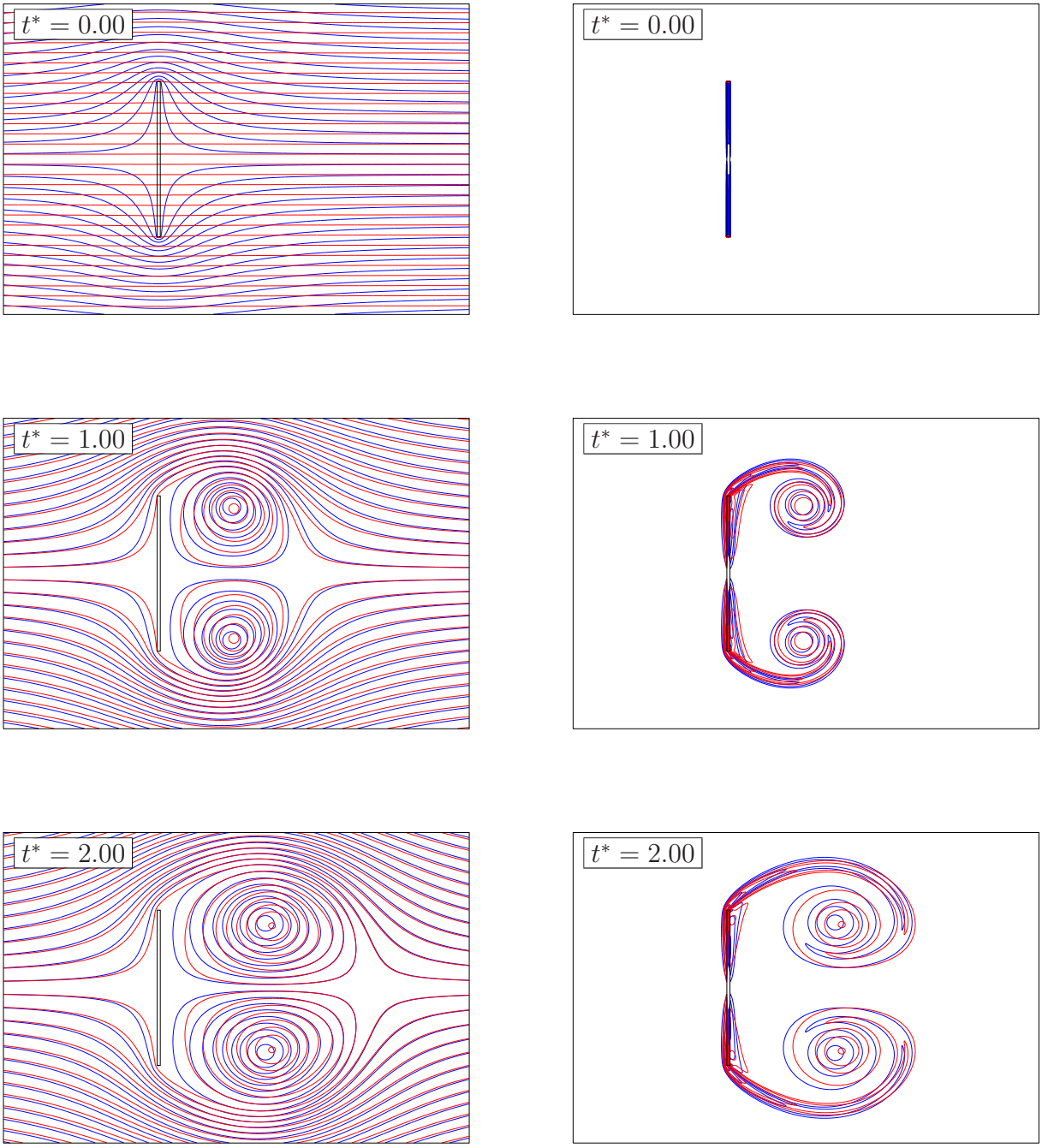

Figure II-9: Comparison of the streamlines (left) and vorticity contours (right) obtained by non-iterative penalisation (red), and iterative penalisation (blue) for an impulsively started flow normal to a flat plate of $H^* = 1/50$. Vorticity contours are $\pm 2^i$ where $i = \{2, 3, 4, 5, 6\}$.

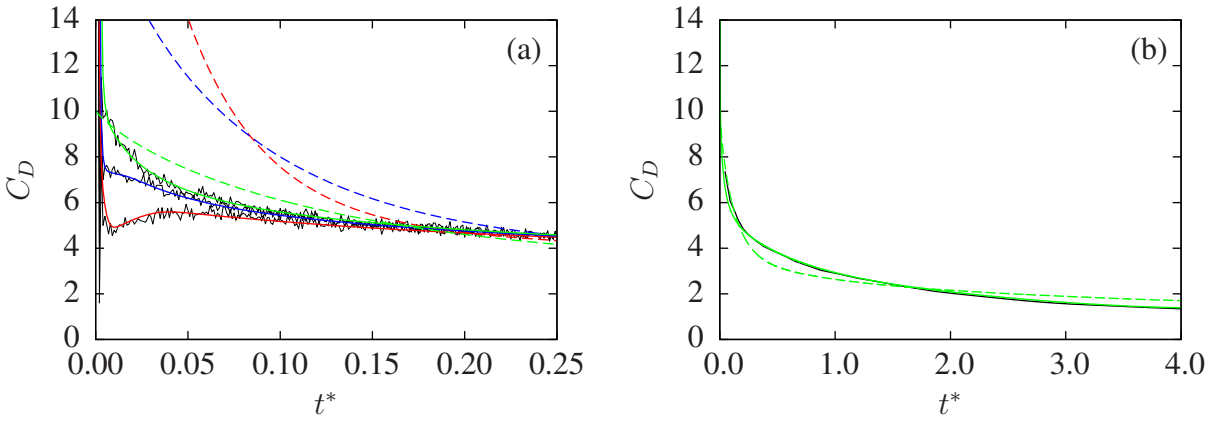

Figure II-10: The calculated drag force for the impulsively started flow normal to a flat plate. (a): Comparison between the iterative penalisation method (full line) and the non-iterative penalisation (dashed line) for plates of: $H^* = 1/50$ (red), $H^* = 1/100$ (blue) and $H^* = 1/200$ (green). The results obtained using the discrete vortex method of (Walther, 1994; Walther and Larsen, 1997; Rasmussen et al., 2010) (black). (b): The calculated drag force on the flat plate of $H^* = 1/200$ (green) as obtained by the non-iterative penalisation (dashed line) and the iterative penalisation method (full line) compared to the drag force of an infinitely thin plate by (Koumoutsakos and Shiels, 1996) (black).

observed that the separation angle is quickly formed whereas the formation is slower as the length-to-thickness ratio is increased. At a relatively large thickness the slow formation of the separation angle is believed to cause a local minimum of the drag coefficient in the start-up phase of the flow as is seen for the plate of $H^* = 1/50$ in Fig. II-10a. After some time when the separation angle is formed on each plate the drag coefficient shows a similar behaviour for all plates tested in this section. It is seen in Fig. II-10b that the drag coefficient of the plate of $H^* = 1/200$ is quite similar to the infinitely thin plate of (Koumoutsakos and Shiels, 1996). For the non-iterative penalisation method it is seen in Fig. II-11 that unlike the iterative penalisation method the formation of surface vorticity is artificially delayed, which prevents the flow from being correctly deflected around the structure. The formation of surface vorticity is identified as being essential to deflect the flow around the structure.

II-3.3 Flow past an impulsively started plate, inclined at 45 degrees and Re=1000

In order to validate the method on an inherently asymmetrical flow, we study the flow past an impulsively started plate at $45°$ with a thickness $H^* = 1/50$ and Re $= 1000$. The non-dimensionalised parameters are the same as those stated in Sec. II-3.2 cf. Eq. (II-24). In the present test case, the spatial resolution $\delta x/L = 1/400$, corresponding to 8 cell lengths across the plate thickness, and the time step is $\delta t^* = 10^{-3}$.

We observe in Fig. II-12 that the penalisation method does not conserve the zero'th moment of the vorticity field (i.e. the total circulation), which for the present simulations reached a level of $\mathcal{O}(10^{-2})$ for both the non-iterative and the iterative penalisation method. To ensure the

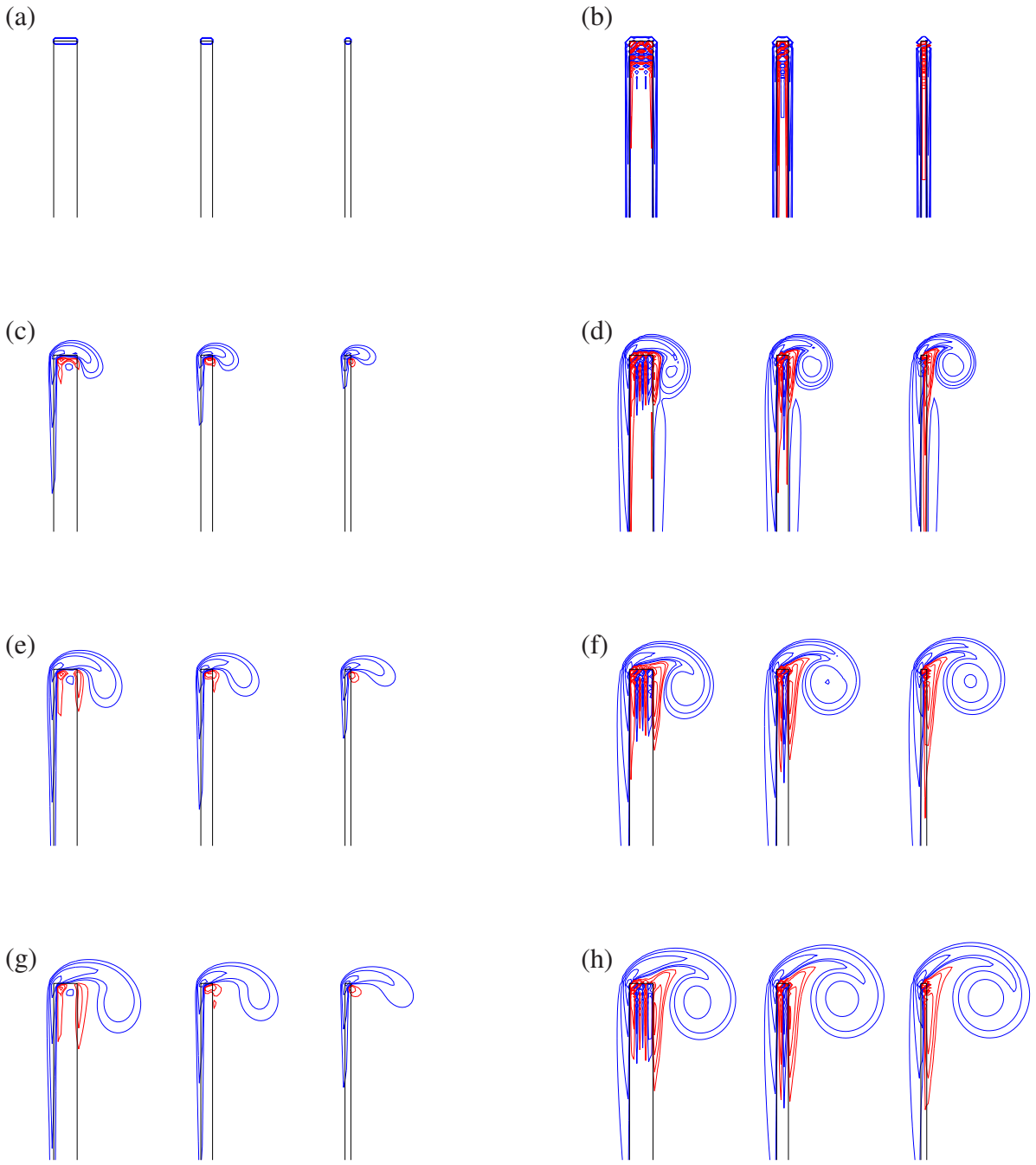

Figure II-11: The contours of vorticity for the impulsively started flow normal to a flat plate of $H^* = 1/50,\ 1/100$, and $1/200$ as obtained by the non-iterative penalisation (a,c,e,g) and the iterative penalisation method (b,d,f,h) at times (a) and (b): $t^* = 0.0$, (c) and (d): $t^* = 0.02$, (e) and (f): $t^* = 0.04$, (g) and (h): $t^* = 0.06$. Vorticity contours at $\pm 2^i$ where $i = \{6, 7, 8, 9, 10\}$ for positive values (red) and negative values (blue).

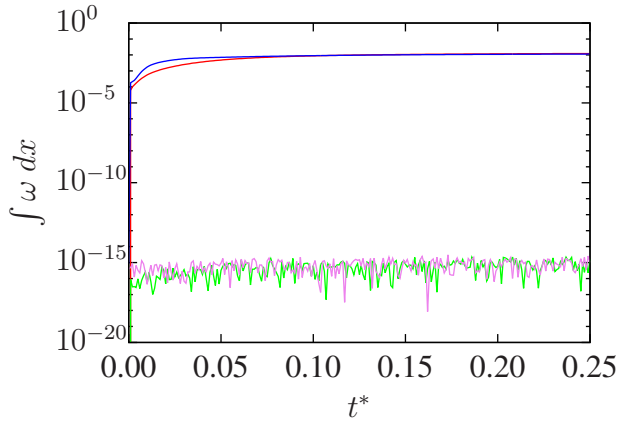

Figure II-12: The calculated 0-th vorticity moment for the impulsively started flow at a 45 degree angle to a flat plate of $H^* = 1/50$. Non-iterative penalisation without correction (red), non-iterative penalisation with correction (green), iterative penalisation without correction (blue), iterative penalisation with correction (violet).

conservation of the zero'th moment of the vorticity field we include the residual of the zero'th vorticity moment in the calculation of the penalisation vorticity (Sec. II-2.3). This is performed by distributing the residual vorticity onto the interior cells before each penalisation iteration.

In Fig. II-13 the calculated drag force is compared to calculations performed with the discrete vortex method of (Walther, 1994; Walther and Larsen, 1997; Rasmussen et al., 2010) which uses a BEM. The iterative penalisation method agrees well with the BEM whereas a clear delay and deviation is observed for the non-iterative penalisation. It is seen that for this case there is no noticeable difference in the force coefficients between the penalisation with and without a correction to conserve the zero'th vorticity moment. Additionally, data of a similar simulation using a plate of thickness $H^* = 0.023$ with semicircular edges has been provided by (Wang and Eldredge, 2013) and is shown in Fig. II-13 as a reference. It is seen that the forces at an early state differ slightly for the two plates which is to be expected as the effect of the edges are of great importance to the early vortex generation as was also seen in Sec. II-3.2.

In Fig. II-14 the streamlines and vorticity contours are compared for the non-iterative and iterative penalisation method. It is seen that the iterative penalisation method is able to predict non-trivial stagnation points at the initial time $t^* = 0.00$. Again there is no noticeable difference between the results obtained with and without the aforementioned correction of the zero'th vorticity moment (not shown).

II-3.4 Uniformly accelerated flow normal to a flat plate of finite thickness at an acceleration-formulated Reynolds number of 16.8 $\times$ 10^5

In this section we investigate a uniformly accelerated flow normal to a flat plate of finite thickness. The acceleration normalised Reynolds number β, the non-dimensional time, and the

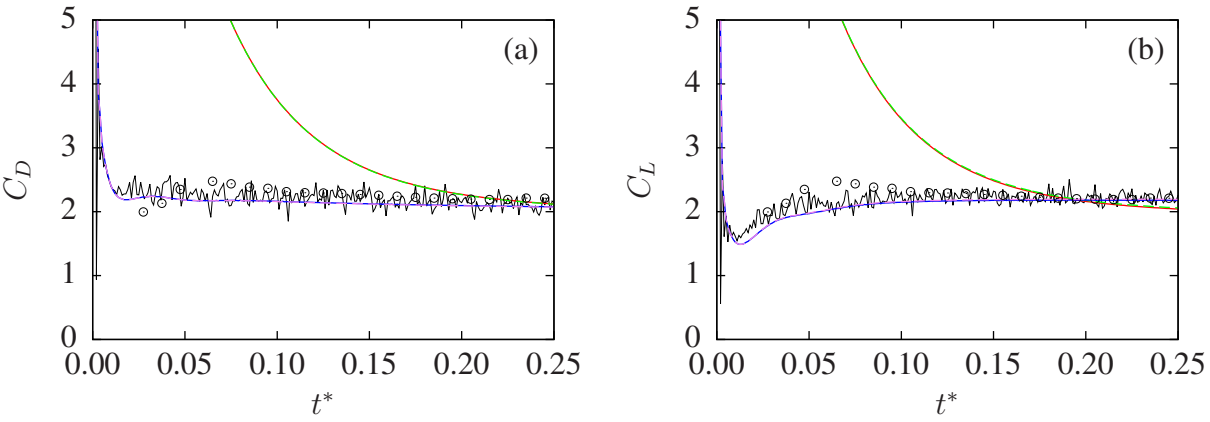

Figure II-13: The calculated force coefficients for the impulsively started flow at a 45 degree angle to a flat plate of $H^* = 1/50$. (a): Comparison between the drag coefficient. (b): Comparison between the lift coefficient. Non-iterative penalisation without correction of the 0-th vorticity moment (red), non-iterative penalisation with correction of the 0-th vorticity moment (green), iterative penalisation without correction of the 0-th vorticity moment (blue), iterative penalisation with correction of the 0-th vorticity moment (violet). The results obtained using the discrete vortex method of (Walther, 1994; Walther and Larsen, 1997; Rasmussen et al., 2010) (black line), results of (Wang and Eldredge, 2013) (black points) for a flat plate of similar thickness and rounded corners.

drag coefficient as given for this case by (Koumoutsakos and Shiels, 1996) are:

$$\beta = \frac{aL^3}{\nu^2}, \qquad t^* = \frac{at^2}{L}, \qquad \text{and} \qquad C_D = \frac{2\boldsymbol{F}\cdot\boldsymbol{e}_x}{(at_f)^2 L}. \tag{II-25}$$

where a is the constant acceleration of the plate.

Following (Koumoutsakos and Shiels, 1996) we chose t_f such that $t_f^* = 25.$ and $a = 1.68$ and $\nu = 10^{-3}$ to reach an acceleration-formulated Reynolds number of $\beta = 16.8 \times 10^5$. The time step used in the present simulation is limited by the Fourier number $\mathrm{Fo} = \delta t\nu/\delta x^2 < \frac{1}{4}$ cf. (Rasmussen et al., 2011), and $\delta t = 10^{-3}$ is chosen in order to be consistent with the simulation performed of the impulsively started flat plate, but approximately 4 times smaller than the time step used in (Koumoutsakos and Shiels, 1996).

The results for the uniformly accelerated flat plate of $H^* = 1/50$ is shown in Figs. II-15 and II-16 where a significant difference is observed between the non-iterative and the iterative penalisation method. For the iterative penalisation method the tolerance of the residual force is set to $\varepsilon = 10^{-3}$, and a convergence is generally achieved by approximately 140 penalisation iterations per time step. It is seen in Fig. II-15 that even at late times the non-iterative penalisation method is unable to deflect the flow around the plate and the flow is seen to penetrate the plate. The insufficient penalisation creates a distorted separation region and a large difference is noticed in the flow field compared to the results obtained using the iterative penalisation.

In Fig. II-16 the calculated drag coefficient compared to a simulation using the discrete vortex method of (Walther, 1994; Walther and Larsen, 1997; Rasmussen et al., 2010) for the start-up, and the results of (Koumoutsakos and Shiels, 1996) for the long time simulation. All

Figure II-14: Comparison of the streamlines (left) and vorticity contours (right) for an impulsively started flow at a 45 degree angle to a flat plate of $H^* = 1/50$. The results obtained by non-iterative penalisation (red), and iterative penalisation with correction of the zero'th vorticity moment (blue). Vorticity contours are $\pm 2^i$ where $i = \{1, 4, 8\}$.

simulations are performed with same non-dimensional parameters of Eq. (II-25), however the results of (Koumoutsakos and Shiels, 1996) were obtained using an infinitely thin plate whereas in the present simulations a plate of $H^* = 1/50$ is used. It is seen that while the non-iterative penalisation deviates from the reference solutions the iterative method again obtains results in excellent agreement with those obtained using BEM.

II-4 Conclusion

The need to extend the Brinkman penalisation method, by performing sub-iterations to improve its accuracy in enforcing the fluid-solid interface was demonstrated. The improved accuracy of the iterative method was showed using benchmark problems computed by re-meshed vortex methods with and without iterative penalisation. The calculated flow-induced forces of the iterative method are in excellent agreement with results obtained using a boundary element method (BEM). Furthermore, the resulting flow fields are shown to be significantly improved for the iterative method compared to that obtained by the standard non-iterative penalisation method. We note that the BEM methods rely on body-fitted grids to perform the re-meshing of the flow, while the penalisation allows the flexibility of simple uniform meshes.

Our results clearly demonstrate that the non-iterative penalisation method has inherent difficulties in correctly penalising the velocity component normal to the boundary within a single time step. Thus, the non-iterative penalisation method imposes very stringent conditions on the employed time step so as to produce accurate results. With the proposed iterative penalisation algorithm the correct boundary condition can indeed be obtained in a single time step at a reasonable additional cost. Furthermore it was shown that the iterative method produces results in excellent agreement to those of the BEM using an equal magnitude time step.

We note that in the present work the iterative penalisation algorithm was coupled with re-meshed vortex methods. We consider however that it can be readily coupled with other solvers, such as finite difference or finite volume, that are used widely for simulations past complex deforming geometries (Vasilyev and Kevlahan, 2002; Schneider and Farge, 2002). The method provides significantly enhanced accuracy while maintaining the flexibility of uniform grids in handling complex geometries. Current work includes the extension of the iterative penalisation method to three-dimensional problems with moving solid bodies (Spietz et al., 2015, 2016).

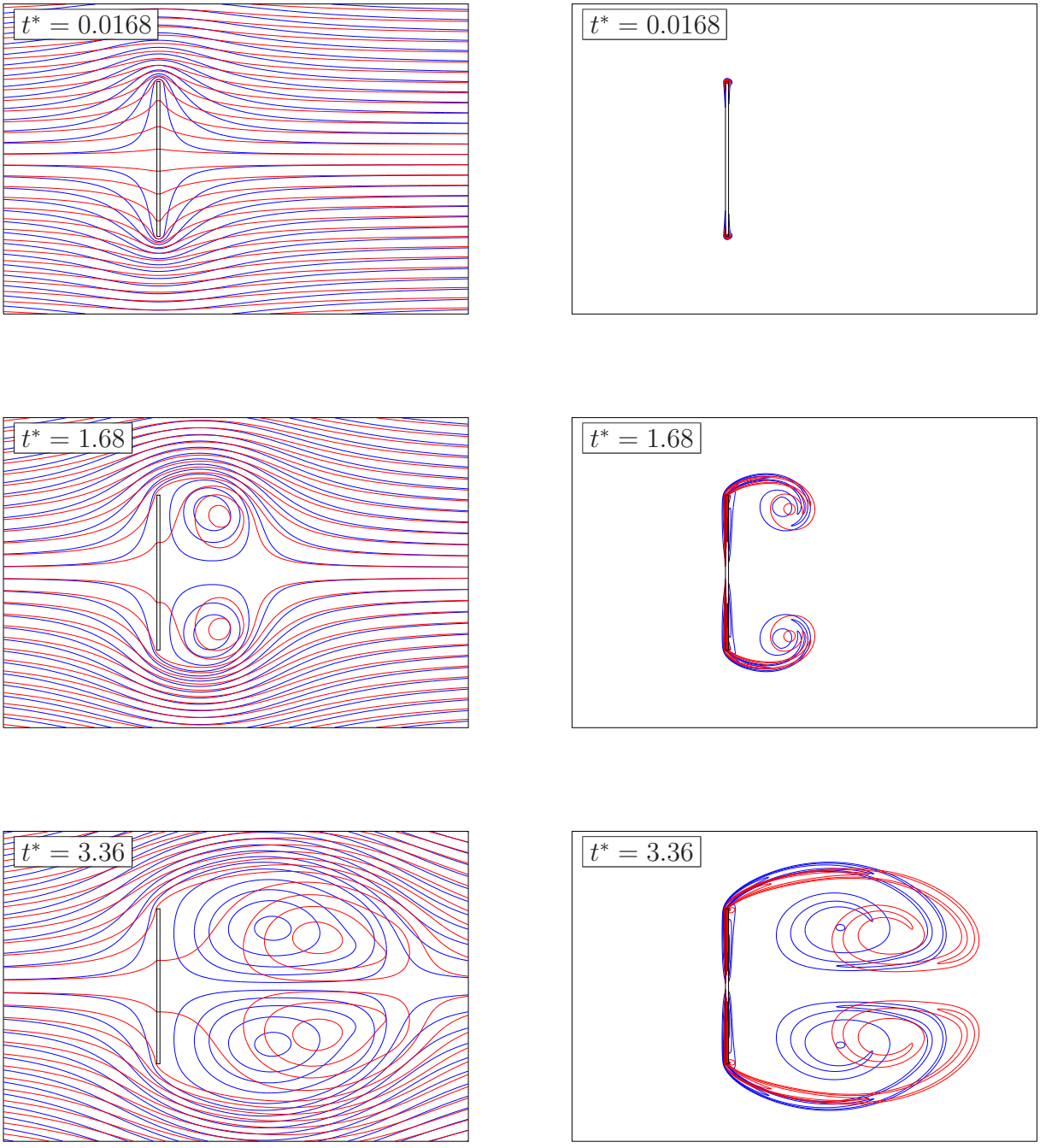

Figure II-15: Comparison of the streamlines (left) and vorticity contours (right) obtained by non-iterative penalisation (red), and iterative penalisation (blue) for an accelerated flow normal to a flat plate of $H^* = 1/50$. Vorticity contours are $\pm 2^i$ where $i = \{4, 5, 6, 7\}$.

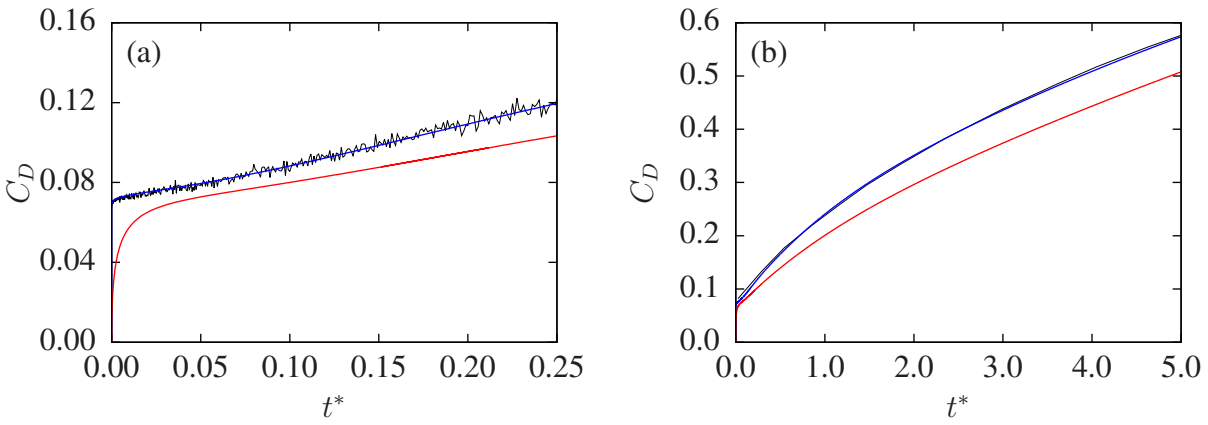

Figure II-16: The calculated drag force for the uniformly accelerated flow normal to a flat plate of $H^* = 1/50$ as obtained by the non-iterative penalisation (red) and the iterative penalisation method (blue) (a): The calculated drag coefficient on the flat plate compared to calculations using the discrete vortex method of (Walther, 1994; Walther and Larsen, 1997; Rasmussen et al., 2010) (black). (b): The calculated drag coefficient on the flat plate compared to the drag force of an infinitely thin plate by (Koumoutsakos and Shiels, 1996) (black).

Article III

On estimating the aerodynamic admittance of bridge sections by a mesh-free vortex method

Mads Mølholm Hejlesen[1], Johannes Tophøj Rasmussen[1],
Allan Larsen[2], Jens Honoré Walther[1,3]

[1]Department of Mechanical Engineering, Technical University of Denmark, Building 403, DK-2800 Kgs. Lyngby, Denmark
[2]COWI Consulting Engineers and Planners A/S, Denmark
[3]Computational Science and Engineering Laboratory, ETH Zürich, Clausiusstrasse 33, CH-8092 Zürich, Switzerland

This chapter consists of a modified version of the published journal articel:
On estimating the aerodynamic admittance of bridge sections by a mesh-free vortex method. J. Wind Eng. Ind. Aerodyn.,146:117–127, 2015.

Abstract

A stochastic method of generating a synthetic turbulent flow field is combined with a 2D mesh-free vortex method to simulate the effect of an oncoming turbulent flow on a bridge deck cross-section within the atmospheric boundary layer. The mesh-free vortex method is found to be capable of preserving the a priori specified statistics as well as anisotropic characteristics of the synthesized turbulent flow field. From the simulation, the aerodynamic admittance is estimated and the instantaneous effect of a time varying angle of attack is briefly investigated. The obtained aerodynamic admittance of four aerodynamically different bridge sections are compared to available wind tunnel data, showing good agreement between the two.

III-1 Introduction

In the design phase of large suspension bridges many resources are normally used to conduct extensive wind tunnel tests to prevent structural failure caused by aerodynamic forces. Various experimental methods are used to determine the influence of static, periodic and stochastic aerodynamic forces on the bridge, and how these excite certain structural responses of the bridge. Due to a required high structural stiffness, bridge decks are typically box-shaped and hence aerodynamically bluff bodies. The result is a highly complex flow around the bridge deck, which can cause a number of aero-elastic phenomena to occur under different conditions. Aerodynamically bluff bodies are generally more sensitive to flow separation, and thus a significant change in the aerodynamic forces may be observed when varying the angle of attack. Hence the effect of turbulence in the oncoming flow becomes important when evaluating the com-

plete aerodynamic performance of the bridge section, as the turbulence results in a fluctuating effective angle of attack.

The effect of a turbulent oncoming flow on the aero-elastic interactions of the bridge is indeed non-trivial. On one hand the turbulent fluctuations of the flow will introduce a stochastic aerodynamic force which will disturb any periodic excitation and thus stabilize the bridge against flutter. On the other hand the stochastic fluctuations may themselves be a cause to unpredicted high aerodynamic forcing on the bridge. As turbulence consists of eddies of multiple scales that are transported by the flow, the sampled flow velocity at a fixed point will show a time history which contains a large band of frequencies at different energy levels. Therefore, with a strong analogy to ocean waves, situations occur where the turbulent eddies at different flow scales becomes instantaneously synchronized resulting in a fluctuation that is even larger than the amplitude of the largest eddies in the flow. When subject to such super-scale fluctuations the bridge section will experience sudden large change in the aerodynamic forcing and a vortex formation on the leading edge of the bridge may occur. Vortex formation on the leading edge is of significant concern as it produces strong gusts on the traffic lane which may be dangerous for large vehicles travelling on the bridge deck.

(Prendergast and McRobie, 2006; Prendergast, 2007) presented a vortex method to simulate an oncoming turbulent flow in bluff body aerodynamics. The flow was simulated using the Discrete Vortex Method (DVM) implementation VXFlow by (Morgenthal, 2002). The oncoming turbulent flow was implemented by synthesizing a time varying turbulent velocity field by a stochastic method, originally proposed by (Shinozuka and Jan, 1972), on the corner-points of a single column of mesh cells upstream of the bridge section. The circulation of each cell of the velocity field was then calculated and included in the DVM simulation by seeding the circulation as vortex particles throughout the simulation.

(Rasmussen et al., 2010) used a similar approach, based on the DVM implementation DVMFLOW by (Walther, 1994; Walther and Larsen, 1997), to obtain an extended aerodynamic analysis of the effect of a turbulent oncoming flow. Emphasis was placed on the spectral transfer functions between the turbulent velocity fluctuations of the oncoming wind and the resulting buffeting forces acting on the bridge section. This transfer function is referred to as the aerodynamic admittance function. (Rasmussen et al., 2010) showed that the aforementioned method is able to to successfully calculate the aerodynamic admittance function of a flat plate.

The concept of aerodynamic admittance employed in the present paper represents the chord wise filtering action of the solid deck section on the incoming turbulence. This definition is concordant with the two-dimensional (2D) classical assumption that the turbulent wind impacting onto a given span wise section creates aerodynamic forces proportional to the steady state load coefficients at this section only and as a consequence the span wise coherence of the aerodynamic forces is identical to the span wise coherence of the oncoming turbulence. Recent research has demonstrated that this not the case for common bridge decks for which the span wise forces are found to be much more correlated than the oncoming turbulence although of less magnitude than expected from the classical assumption (Larose, 2003). Strip theory which splits the aerodynamic action of the turbulence in a chord wise (aerodynamic admittance) and a span wise component (root coherence of turbulence) is often employed in common commercial gust loading (buffeting) calculations for want of better models thus 2D aerodynamic admittance functions simulated in the present paper remain interesting to bridge designers.

In this paper, we extend the validation of the method of (Rasmussen et al., 2010) towards

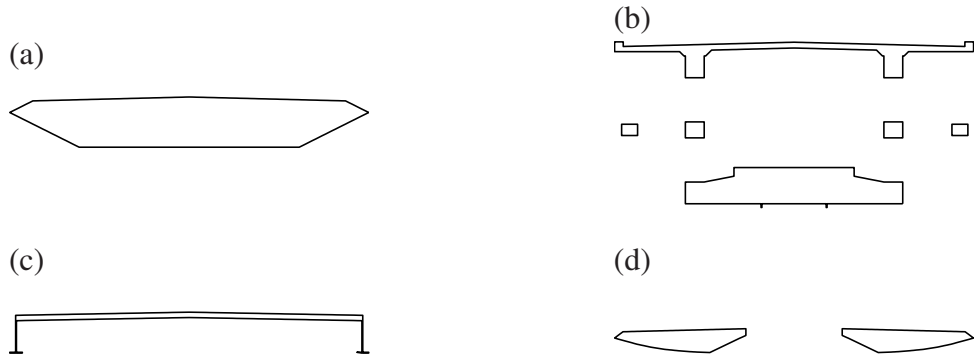

Figure III-1: Cross-sections of the four bridge decks (scaled to unity chord) which are investigated in the present study. m (a) Great Belt East bridge, mono box girder bridge, (b) Øresund bridge, double deck truss bridge, (c) Busan-Geoje bridge, plate girder bridge, (d) Stonecutters bridge, twin box girder bridge.

a practical application in bridge aerodynamics. The aerodynamic admittance function of four different bridge sections are investigated and compared with available experimental data. The bridge sections which are shown in Fig. III-1 represents a selection of the most common bridge deck types used in bridge design: the mono box bridge (Great Belt East bridge), the double deck truss bridge (Øresund bridge), the plate girder bridge (Busan-Geoje bridge) and the twin box bridge (Stonecutters bridge).

In this work only a brief outline of the method is presented and the reader is referred to (Rasmussen et al., 2010; Rasmussen, 2011) for a detailed description and validation of the applied numerical method.

III-2 Methodology

III-2.1 The discrete vortex method

The flow is simulated using the two-dimensional DVM implementation DVMFLOW by (Walther, 1994; Walther and Larsen, 1997). Here the velocity-vorticity formulation of the Navier-Stokes equation is solved in a Lagrangian frame of reference by simulating computational particles which represents an elementary distribution of vorticity referred to as a vortex blob. Hence, as vorticity is a material property which is advected with the flow, the particle position $\boldsymbol{x}_p$ is solved in the Eulerian frame of reference by:

$$\frac{d}{dt}\boldsymbol{x}_p = \boldsymbol{v}(\boldsymbol{x}_p). \tag{III-1}$$

The velocity field $\boldsymbol{v} = (u, v, 0)$ is obtained from the vorticity field $\boldsymbol{\omega} \equiv \boldsymbol{\nabla} \times \boldsymbol{v}$ by solving the inverted kinematic relation for an incompressible flow, where $\boldsymbol{\nabla} \cdot \boldsymbol{v} = 0$, by which:

$$\boldsymbol{\nabla}^2 \boldsymbol{v} = -\boldsymbol{\nabla} \times \boldsymbol{\omega}. \tag{III-2}$$

The vorticity only has the out-of-plane component in a 2D flow i.e. $\boldsymbol{\omega} = (0, 0, \omega)$. Eq. (III-2) is recognized as a Poisson equation and can be solved for an arbitrary point $\boldsymbol{x}_p$ by the Biot-Savart law which by using a Gaussian regularised is given by:

$$\boldsymbol{v}(\boldsymbol{x}_p) = \boldsymbol{V} - \sum_{i=1}^{N_p} \frac{\Gamma_i}{2\pi\, r_i^2} \left(1 - \exp\left(-\frac{r_i^2}{2\sigma^2}\right)\right) \begin{pmatrix} (y_p - y_i) \\ -(x_p - x_i) \end{pmatrix}. \tag{III-3}$$

Here $r = |\boldsymbol{x}_p - \boldsymbol{x}_i|$, σ is the Gaussian regularisation radius, N_p is the number of particles in the flow, $\boldsymbol{V} = (U, 0)$ is the free-stream velocity, and Γ_i is the circulation of the particles which super-positioned represents the integral of the vorticity field. To reduce the computational load, Eq. (III-3) is evaluated using the fast multi-pole method (Carrier et al., 1988).

The incompressible 2D Navier-Stokes equation is solved in velocity-vorticity form:

$$\frac{D}{Dt}\omega = \nu \boldsymbol{\nabla}^2 \omega, \tag{III-4}$$

where ν denotes the kinematic viscosity of the fluid. It is seen that Eq. (III-4) is a diffusion equation which may be solved by a stochastic random walk method (Chorin, 1973). Hence, the diffusion of vorticity (Eq. (III-4)) may be included in the trajectory equation (Eq. (III-1)) by introducing a random walk in which the trajectory equation becomes:

$$\frac{d}{dt}\boldsymbol{x}_p = \boldsymbol{v}_p + \sqrt{\frac{2\nu}{\delta t}}\, \boldsymbol{\eta}. \tag{III-5}$$

Here $\boldsymbol{\eta}$ is a Gaussian distributed random number with a zero mean and a unit standard deviation, and δt is the time step size used in the simulation.

III-2.2 Simulating the effect of turbulent upstream flow

Following the work of (Prendergast and McRobie, 2006; Prendergast, 2007) and (Rasmussen et al., 2010) the effect of turbulent oncoming flow is simulated by releasing vortex particles upstream of the bridge section to induce velocity fluctuations in the oncoming flow. This is done by seeding pre-generated vortex particles in a single column located at a specified distance upstream of the bridge section. A new column of particles is released at a specified time frequency during the simulation. Hence the simulated velocity fluctuations may contain frequencies up to half the seeding frequency (Nyqvist-Shannon sampling theorem). As the simulation progresses the seeded vortex particles creates a particle cloud consisting of multiple interacting vortex particles which emulates turbulent eddies of multiple scales. As the bridge becomes immersed in the particle cloud it will interact with the seeded particles and thus the effect of a turbulent oncoming flow is included in the simulation and the resulting buffeting forces may be extracted from the data.

The pre-generated vortex particles, which are seeded at a specified time interval δt_{gen} during the simulation, are constructed by defining a release ladder consisting of a $2 \times (N_p + 1)$ array of cell corner points with a uniform spacing of $\delta x = V\, \delta t_{gen}$ with the particles located at the cell centre as seen in Fig. III-2. In the corner points of the release ladder, two-component time signals of a turbulent velocity field are generated by a stochastic method originally proposed by

Figure III-2: Conceptual sketch of the release ladder (here $N_c = 8$ and $N_p = 3$) upstream of the bridge section. The velocity signal is generated at the corner points of the release ladder (red crosses) and the vortex particles at the cell centre (blue dots).

(Shinozuka and Jan, 1972) in order to reproduce the correlation characteristics of a turbulent flow.

Generating a multiple series of correlated random numbers by a stochastic simulation is done by first defining a correlation matrix which gives the correlation between each of the random number series i.e. each of the corner points of the release ladder. A random correlated field $\gamma(\boldsymbol{x}, t)$ which is a function of both space and time may be discretised as a multivariate process dependent on time only, hence:

$$\gamma(\boldsymbol{x}, t) \quad \Rightarrow \quad \{\gamma_1(t), \gamma_2(t), ..., \gamma_{N_c}(t)\} \tag{III-6}$$

where the sub-index refers to the corner-point positions sketched in Fig. III-2. The correlated random numbers are generated by convolving a white noise variable with a function which generates the desired correlation. For a multivariate process this may be written as:

$$\gamma_i(t) = \int_{-\infty}^{\infty} \mathcal{H}_{ij}(t-\tau)\, \phi_j(\tau)\, d\tau, \qquad \{i, j\} = \{1, 2, ..., N_c\}. \tag{III-7}$$

Here $\phi_j(t)$ is a random white noise time signal at point $\boldsymbol{x}_j$ and $\mathcal{H}_{ij}(t-\tau)$ is a matrix which generates the correlation between point $\boldsymbol{x}_i$ and $\boldsymbol{x}_j$ given a time lag of τ. The convolution of Eq. (III-7) is effectively done spectrally by fast Fourier transforms where the spectral functions of $\mathcal{H}_{ij}(t)$ which is denoted by $\widehat{\mathcal{H}}_{ij}(k)$, can be determined from the spectral correlation matrix $\widehat{C}_{ij}(k)$. The spectral correlation matrix is defined by the given spectral power density function $S(k)$, which gives the statistical characteristics of the turbulent kinetic energy at frequency $k = 2\pi/t$, combined with a coherence function (Davenport, 1968; Solari, 1987; Rossi et al., 2004) which correlates the points to give:

$$\widehat{C}_{ij}(k) = S(k)\, \exp\left(-\frac{k}{2\pi}\left(\frac{\sqrt{c_x^2(x_i - x_j)^2 + c_y^2(y_i - y_j)^2}}{U} + \iota\, \frac{2\pi\,(x_i - x_j)}{U}\right)\right) \tag{III-8}$$

where c_x and c_y are the directional decay parameters of turbulent eddies. The effect of free-stream advection is included by introducing a phase shift which is determined using Taylor's frozen turbulence hypothesis as the imaginary part of Eq. (III-8). The relation between $\widehat{C}_{ij}(k)$ and $\widehat{\mathcal{H}}_{ij}(k)$ is given by the spectral correlation function by inserting Eq. (III-7):

$$\widehat{C}_{ij}(k) = \widehat{\gamma}_i\,\widehat{\gamma}_j^* = (\widehat{\mathcal{H}}_{ik}\,\widehat{\phi}_k)(\widehat{\mathcal{H}}_{jl}\,\widehat{\phi}_l)^* = \widehat{\mathcal{H}}_{ik}\,\widehat{\mathcal{H}}_{kj}^{*T} \tag{III-9}$$

where the superscripts $*$ and T denote the complex conjugate and the transpose, respectively. Here the correlation properties of the white noise variable is used which in spectral form is:

$$\widehat{\phi}_k\,\widehat{\phi}_l^* = \begin{cases} 1 & \text{for } k = l \\ 0 & \text{for } k \neq l \end{cases} \tag{III-10}$$

From Eq. (III-8) we see that $\widehat{C}_{ij}$ is a Hermitian matrix (i.e. $\widehat{C}_{ij} = \widehat{C}_{ij}^{*T}$) which enables the determination of $\widehat{\mathcal{H}}_{ik}$ to be performed by the Cholesky decomposition of $\widehat{C}_{ij}$ given that $\widehat{C}_{ij}$ is positive definite which is indeed the case for the configurations used in this work. Once $\widehat{\mathcal{H}}_{ik}$ is defined, it is straight forward to calculate a series of correlated random variables $\gamma_i(t)$ by Eq. (III-7).

The process is performed independently for both components of the velocity field i.e. $\gamma_i = \{u_i, v_i\}$ without any cross-correlation between the components. For the spectral energy density functions $S(k)$ we use the semi-empirical spectral functions $S_u(k)$ and $S_v(k)$ which was proposed by (ESDU, 1993, 2001) for measured turbulence in the atmospheric boundary layer and are summarized in App. III-A. The ESDU spectra may be constructed by defining the turbulence intensity, the atmospheric boundary layer thickness, the height above ground, and the surface roughness length. For the present implementation these input parameters are the same for all points of the release ladder.

The approach outlined above implies that the resulting velocity field does not represent a solution to the Navier-Stokes equations hereunder the incompressibility condition of $\boldsymbol{\nabla} \cdot \boldsymbol{v} = 0$. The generated field is a synthetic flow field in which the fluctuations of the two velocity components posses the same statistical characteristics as the corresponding two velocity components of a 3D turbulent flow field measured in the atmospheric boundary layer. However the extensive analysis presented in (Prendergast and McRobie, 2006; Prendergast, 2007; Rasmussen et al., 2010; Rasmussen, 2011) showed that when the generated velocity field is converted to circulation and simulated in the discrete vortex method it is indeed possible to admissibly reproduce the statistical characteristics of the input energy density spectra.

The generated velocity field is converted to circulation of a cell centred particle for each time step by integrating the velocity of the surrounding cell corner points by:

$$\Gamma = \oint_{\mathcal{C}} \boldsymbol{v}(\boldsymbol{x}) \cdot d\boldsymbol{s} \tag{III-11}$$

Using the trapezoidal rule, the velocities of the corner points are integrated by assuming a linear variation between the corner points of the release ladder. To correct for the varying distance r from the cell edge to the centre of the cell, the circulation is corrected in magnitude by a factor of $\pi/2$ as proposed by (Prendergast, 2007).

III-2.3 The boundary element method

The bridge section is simulated by using a boundary element method (Wu, 1976; Walther, 1994). Here the geometry of the bridge section is discretised by a finite number of line segments referred to as panels and the boundary conditions of the fluid-solid interface is enforced by introducing linearly varying vortex sheets at each of the panels. The strength of the vortex sheets are initially unknown and provides a sufficient number of degrees of freedom in order to obtain a flow solution where the velocity component perpendicular to the surface of the geometry is zero i.e. the no-penetrating-flow boundary condition.

The solution is formally obtained by solving a linear system of equations with the added constraint of a zero sum circulation of the entire domain (Walther and Larsen, 1997) i.e. Kelvin's condition of constant total circulation. However, the circulation of the upstream particles that are seeded in order to simulate an oncoming turbulent flow as described in Sec. III-2.2, introduces a non-zero net circulation to the domain. This is accounted for by adjusting the constraint of total circulation to add up to the accumulated circulation $\Gamma_T(t)$ which is introduced by the seeded turbulence particles:

$$\sum_{i=1}^{N_p} \Gamma_i = \Gamma_T(t) \tag{III-12}$$

as was proposed by (Rasmussen et al., 2010). The vortex sheets are converted into a number of vortex particles at each panel which are diffused into the flow. For this, the random walk diffusion of the particles created from the vortex sheet is adjusted to give a one-sided diffusion in the direction normal to the panel. Particles located near the solid boundary may be moved into the solid due to the discrete time stepping or the random walk diffusion model. Such particles are removed from the simulation after which their circulation is implicitly included when solving the boundary conditions in the next time step due to the constraint of Eq. (III-12).

Knowing the strength of the vortex sheet γ_i located at each panel it is possible to calculate the pressure distribution by a simple discretisation of the relation:

$$\frac{1}{\rho}\frac{\partial p}{\partial l} = -\frac{\partial \gamma}{\partial t} \qquad \text{by which} \qquad \delta p_i = -\rho\,\frac{\delta \gamma_i}{\delta t}\,\delta l_i \tag{III-13}$$

Here ρ is the fluid density and δl_i denotes the length of the i-th panel. Given the pressure distribution the forces and moments are simply calculated by summing the contribution of each panel. The total forces and moments including viscous shear are computed from the vorticity moments cf. (Wu, 1978; Walther and Larsen, 1997).

III-2.4 Spectral analysis and the aerodynamic admittance function

Throughout the simulation, time signals of the velocity components u and v are sampled at a fixed sample point upstream of the bridge section together with the aerodynamic forces of lift L, drag D and pitching moment M acting on the bridge section. From the fluctuating part of the time series the power spectra $\mathbb{S}(k)$ are calculated using Welch's method (Welch, 1967) with a 50 % sample overlap.

The aerodynamic admittance function is a spectral relation between the energy of the fluctuating forces for lift or pitching moment and the energy of the fluctuations of the oncoming

velocity field. The calculated aerodynamic admittance function for the lift force $\mathbb{A}_L$ and pitching moment $\mathbb{A}_M$ may be expressed as:

$$\mathbb{A}_L(k) = \frac{\mathbb{S}_L(k)}{\left(\frac{1}{2}\rho U c\right)^2 \left[4C_L^2 \mathbb{S}_u(k) + \left(\frac{dC_L}{d\alpha} + C_D\right)^2 \mathbb{S}_v(k)\right]} \tag{III-14}$$

and:

$$\mathbb{A}_M(k) = \frac{\mathbb{S}_M(k)}{\left(\frac{1}{2}\rho U c^2\right)^2 \left[4C_M^2 \mathbb{S}_u(k) + \left(\frac{dC_M}{d\alpha}\right)^2 \mathbb{S}_v(k)\right]} \tag{III-15}$$

as proposed by (Gu and Qin, 2004). Here C_L and C_M are the force coefficients per unit length for lift and pitching moment respectively which is defined by:

$$C_L = \frac{L}{\frac{1}{2}\,\rho\, U^2\, c} \qquad \text{and} \qquad C_M = \frac{M}{\frac{1}{2}\,\rho\, U^2\, c^2} \tag{III-16}$$

where the angle of attack (α) may be estimated by the small angle approximation $\alpha \approx \tan\alpha = v/u$ when deriving Eqs. (III-14) and (III-15).

It is well stated in the literature (Jancauskas and Melbourne, 1986; Hatanaka and Tanaka, 2002; Costa, 2007) that the admittance function of bridge decks deviates from that of thin aerofoil theory, which is also the case with the numerical and experimental results presented in this work. Thin aerofoil theory however provides a good reference for the aerodynamic admittance functions of bluff bodies, and is presented by a simplification of the Sears function proposed by (Liepmann, 1952):

$$\mathcal{A}_L(k) = \mathcal{A}_M(k) = \frac{1}{1 + \pi c k/U}, \tag{III-17}$$

where $\mathcal{A}_L$ and $\mathcal{A}_M$ denotes the aerodynamic admittance functions for lift and pitching moment respectively of a thin aerofoil.

III-3 Results

III-3.1 Simulation parameters and numerical set up

The simulations of the four bridge sections was performed using input parameters which represent realistic conditions for a bridge deck within the atmospheric boundary layer. For generating the upstream turbulence particles cf. Sec. III-2.2 the input velocity power spectra of Eqs. (III-18) and (III-19) was constructed using a frequency discretisation of 4096 frequencies, giving a simulated highest and lowest frequency k of 5.83 and $1.42 \times 10^{-3}\,\mathrm{rad/s}$, respectively. The physical parameters used in Eqs. (III-18) and (III-19) are chosen to simulate an atmospheric turbulent wind over open landscape, with a turbulence intensity $I_v = \sigma_v/U$ of 5% where σ_v is the standard deviation of the vertical velocity component. The surface roughness used to calculated the shear velocity u_* is set to 3×10^{-3} m, the thickness of the atmospheric boundary layer $h = 660\,\mathrm{m}$, and height above ground $y_0 = 70\,\mathrm{m}$. To dimensionalise the input and output of the vortex simulation a chord length of $c = 30\,\mathrm{m}$ and a horizontal free stream velocity of

$U = 35$ m/s are used for all bridge decks. The horizontal free stream velocity is set to increase the distance between the released particles to achieve a wide particle cloud, without adding unnecessary computational load by simply adjusting the number of particles (Rasmussen et al., 2010). It is important that the particle cloud is wide to insure that the bridge section is fully immersed in the turbulent flow. A convergence of the results was found with 120 particles inserted with a non-dimensionalised distance of $\delta x/c = 0.117$. This produces a wide particle cloud without compromising the density of particles in the flow.

The vortex simulations are performed at a Reynolds number $\mathrm{Re} = U\,c/\nu = 10^4$. The simulations are performed with $40,000$ time steps of $\delta t\,U/c = 0.025$ corresponding to a dimensional time of 857 seconds. Before the spectral analysis, the initial 2000 sampled time steps are discarded ensuring that data is sampled only when the bridge is fully immersed in the turbulent flow.

As mentioned in Sec. III-2.3 the boundary element method uses a finite number of linear panels to define each bridge section, on which the surface circulation is created. The Great Belt East bridge was discretised with 200 panels, Øresund bridge with 420 panels, Busan-Geoje bridge with 200 panels, and the Stonecutters bridge with 300 panels.

III-3.2 Estimation of the static aerodynamic coefficients of the bridge sections

The aerodynamic admittance functions Eqs. (III-14) and (III-15) depend on the sampled velocity spectra $\mathbb{S}_u$ and $\mathbb{S}_v$ which are normalized by the static coefficients and their derivatives, assuming a linear variation with α. The dependence of the static coefficients on the angle of attack α is initially estimated in separate simulation using a laminar oncoming flow at different values of α.

It is seen in Fig. III-3 that the static coefficients for most of the bridge sections do not display any form of symmetry around $\alpha = 0$. This is because the geometry of the bridge sections are only single symmetric and not double symmetric. The non-linear behaviour of the coefficients indicates that the linear approximation which Eqs. (III-14) and (III-15) are based on, is valid only in a limited angular range. In Tab. III-1 and Fig. III-3 the linear fit of the static coefficients and their derivatives are summarised and visualised respectively.

III-3.3 The simulated oncoming turbulent flow

The statistical properties of the velocity field induced by the upstream particle cloud is influenced by the presence of the bridge section as well as the boundary of the particle cloud (Rasmussen et al., 2010). In order to diminish this influence and obtain converged velocity power spectra, the velocity was sampled during the simulations at the height of the bridge section, 6 chord lengths upstream of the bridge section and 19 chord lengths downstream of the particle release ladder. The resulting power spectra $\mathbb{S}_u$ and $\mathbb{S}_v$ of the simulated particle cloud are shown in Figs. III-4a and III-4b compared to the input spectra S_u and S_v of Eqs. (III-18) and (III-19) used to generate the turbulence particles by the stochastic method presented in Sec. III-2.2. In Figs. III-4c and III-4d the autocorrelation of the two velocity components are shown compared to the (ESDU, 1993, 2001) reference. The simulated velocity field is statistical consistent for all

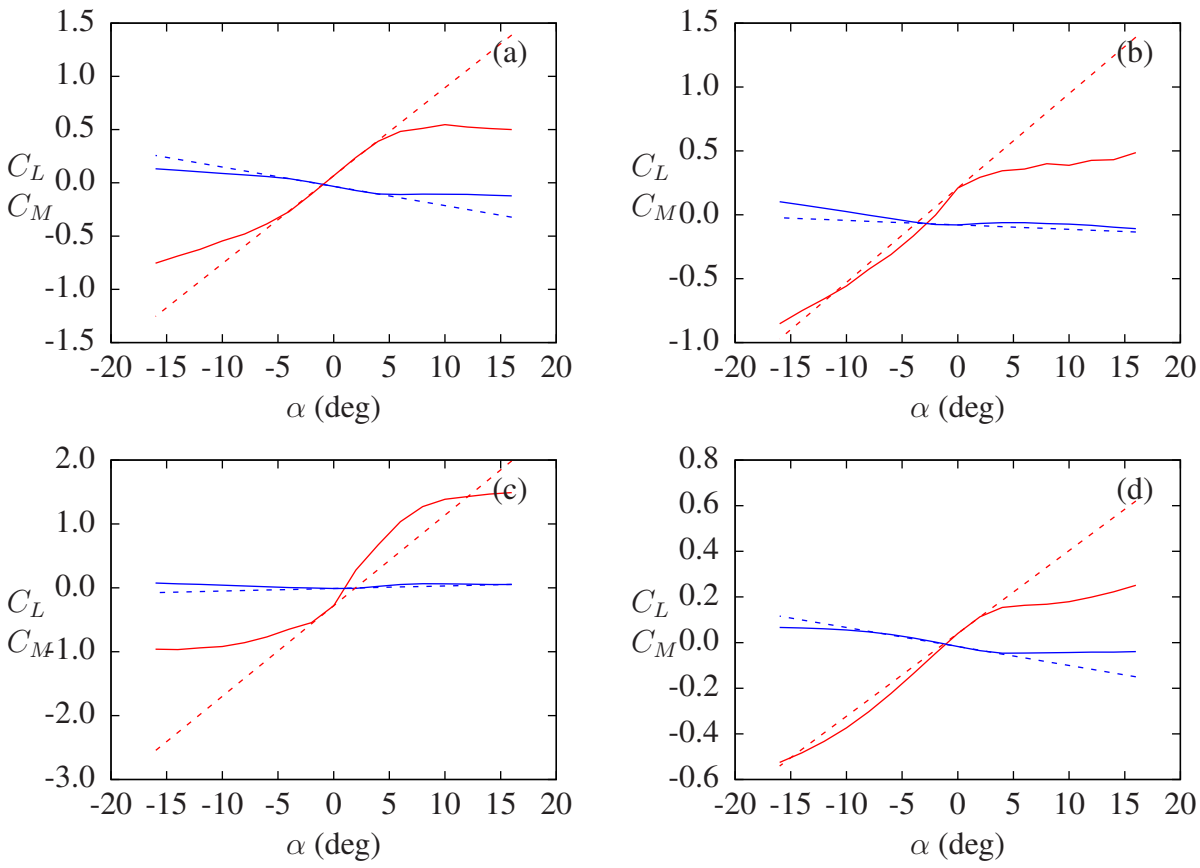

Figure III-3: The calculated static coefficients (full) for the lift force (red) and the pitching moment (blue) and the corresponding approximated linear fit (dashed). (a) Great Belt East bridge, (b) Øresund bridge, (c) Busan-Geoje bridge, (d) Stonecutters bridge.

Bridge	C_D	C_L	C_M	$\frac{\partial C_L}{\partial \alpha}$	$\frac{\partial C_M}{\partial \alpha}$	k_{sh}	St
Great Belt East bridge	0.06	0.07	-0.03	4.73	-1.04	1.43	0.20
Øresund bridge	0.37	0.21	-0.08	4.23	-0.20	1.80	0.25
Busan-Geoje bridge	0.13	-0.28	-0.01	8.12	0.13	1.11	0.15
Stonecutters bridge	0.05	0.04	-0.02	2.08	-0.48	2.18	0.30

Table III-1: The static aerodynamic coefficients of lift C_L, drag C_D and pitching moment C_M and their approximated derivatives with respect to the angle of attack α at $\alpha = 0$. k_{sh} denote the estimated vortex shedding frequency in rad/s and St $\equiv fc/U$ the corresponding Strouhal number.

simulations and is seen to produce a fair agreement with the input spectra though a noticeable deviation is observed for the vertical component at low frequencies. The same deviation is also observed for large time-lags τ in the autocorrelation function where the resulting integral length scales $\mathbb{L}_u = 7.22$ and $\mathbb{L}_v = 1.65$ were found compared to $L_u = 7.66$ and $L_v = 0.84$ of the input spectrum cf. Eq. (III-22). Altogether the deviation is noticed to be towards a more isotropic turbulent field than that of the anisotropic input spectra.

This deviation is partly believed to arise when converting the velocity field of the release ladder into an array of vortex particles. As the velocity components are generated independently on the release ladder allowing a divergence in the resulting velocity field, a part of the generated velocity field is discarded as the calculation of the circulation by Eq. (III-11) disregards any divergence of the velocity field. As a result the total kinetic energy of the vertical fluctuations is observed in Fig. III-4b to be increased compared to that of the input spectra. Additionally, the generated velocity field represents only two of the three velocity components of a 3D turbulent flow. Hence by simulating the flow in 2D only, the flow dynamics is constrained in a way that leads to a different energy transfer than that of the 3D flow and thus changes the energy spectra of the turbulent flow. A more thorough investigation of the evolution of the particle cloud is presented by (Rasmussen et al., 2010).

It is here emphasized that the deviation of the input and sampled velocity spectra has little effect on the estimated aerodynamic admittance function. As the aerodynamic admittance function is a spectral transfer function between the simulated flow velocity and the resulting aerodynamic forces the specific distribution of energy within the frequency range is only of little significance when determining such transfer function. In principle the aerodynamic admittance function could thus be obtained using any velocity field containing fluctuations at a given frequency range of interest.

III-3.4 Analysis of the simulated flow around the bridge sections

The simulated flow fields around the bridge sections are shown in Fig. III-5. Here the instantaneous position and velocity of each vortex particles are plotted. The bridge sections are immersed in the turbulent cloud of particles which is formed by seeding particles upstream of the bridge section as described in Sec. III-2.2. The upstream particle cloud interact with the particles created at the panels of the bridge section resulting in a more irregular vortex shedding than is observed without the upstream seeding of particles.

In a Lagrangian simulation as the DVM the computational elements i.e. the vortex particles are following the trajectory given by the velocity field. Thus it is easy from a flow plot such as those shown in Fig. III-5 to identify important flow structures such as recirculation zones and vortex shedding. It is seen in Fig. III-5 that all bridge sections have significant vortex shedding from the trailing edge of the sections. The vortex shedding is highly periodic and may cause large bridge deck oscillations if it is undisturbed. This is the case with the Great Belt East bridge where no other flow structures occur but the trailing edge vortex shedding (see Fig. III-5a). Consequently the Great Belt East bridge is sensitive to vortex induced vibration as verified in previous wind tunnel tests (Larsen, 1993) and numerical simulations (Larsen and Walther, 1997). For the completed bridge, guide vanes were attached beneath the bridge deck in order to reduce the vortex shedding and ultimately the bridge deck oscillations.

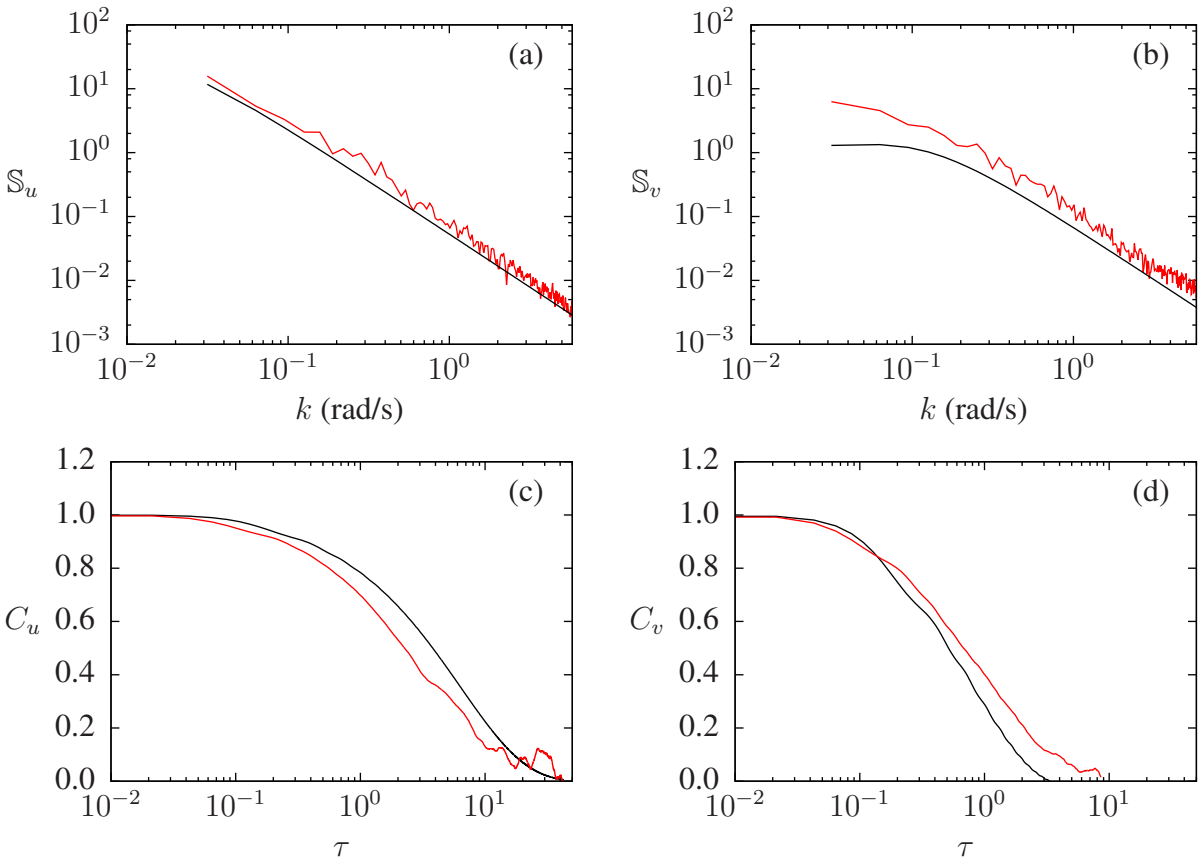

Figure III-4: The sampled velocity field (red) compared to the model of (ESDU, 1993) used to create the velocity field (black). (a) velocity power spectrum of the u-component, (b) velocity power spectrum of the v-component, (c) auto-correlation function of the u-component, (d) auto-correlation function of the v-component.

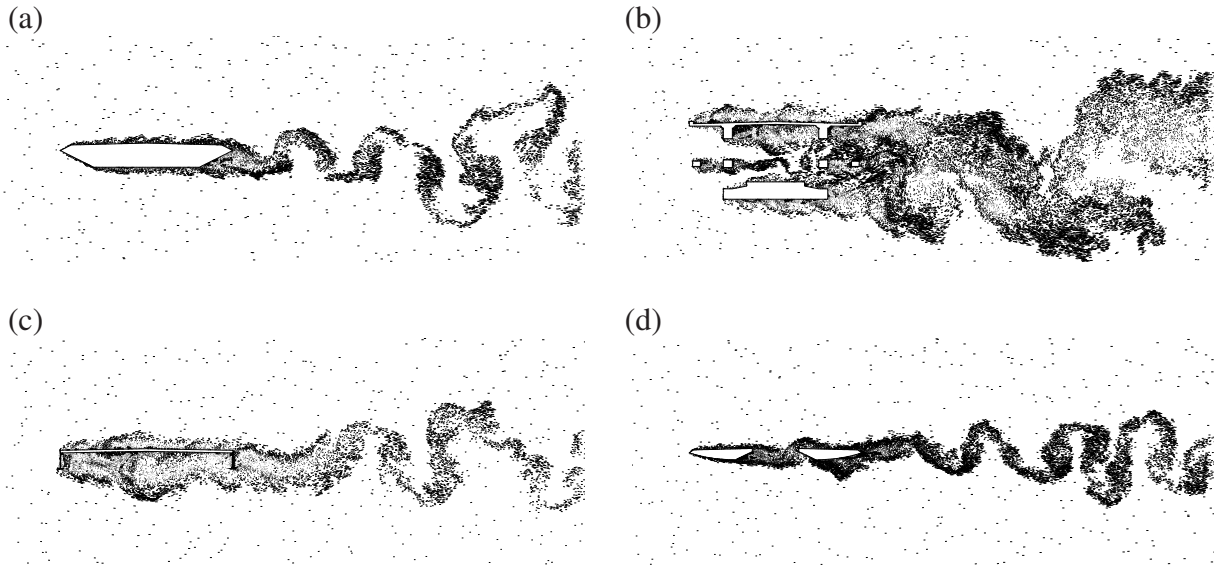

Figure III-5: The simulated turbulent flow field past the four bridge sections (scaled to unity chord). The figure shows the instantaneous position and velocity of the individual vortex particles. (a) Great Belt East bridge, (b) Øresund bridge, (c) Busan-Geoje bridge, (d) Stonecutters bridge.

The bridge deck cross section of the Øresund bridge consists of multiple sub-structures as the bridge deck itself is a double deck truss bridge. Each of the sub-structures have an individual vortex shedding (Fig. III-5b) which makes the combined vortex shedding of the bridge deck highly irregular. This disturbs the periodic effect of the force associated with vortex shedding making the bridge deck more aerodynamically stable.

The flow image of the Busan-Geoje bridge deck (Fig. III-5c) reveals that the girder structure of the bridge deck causes a significant re-circulation zone behind the leading edge girder. At times this re-circulation zone becomes unstable resulting in a large vortex which travels to the trailing edge girder of the bridge section. This kind of flow behaviour evidently creates a time-lagged correlation of the local aerodynamic forcing at the leading and trailing edges of the bridge and is known to cause a pitching motion of the bridge deck (Lawson, 1980).

The Stonecutters bridge deck consists of two relatively thin box-sections. It is seen in Fig. III-5d that the large gap between the boxes allows vortex shedding to form on the leading box which highly influences the flow around the trailing box. The wake of the leading box creates an oscillating inflow angle of attack on the trailing box which increase the periodic aerodynamic forcing and may result in leading edge flow separation on the trailing box.

III-3.5 Estimation of the aerodynamic admittance function

The aerodynamic admittance functions which are calculated from the data extracted from the simulations are shown in Fig. III-6 for the lift force and Fig. III-7 for the pitching moment along with available experimental data (Strømmen et al., 1996; COWI A/S, 2008) and the aerodynamic admittance functions of thin aerofoil theory (Eq. (III-17)). The calculated aerodynamic admittance functions are generally different from that of the thin aerofoil theory which

is to be expected and show an overall good agreement to the aerodynamic admittance functions of experimental investigations (Strømmen et al., 1996; COWI A/S, 2008). The observed deviations of the aerodynamic admittance function for the lift force at the low frequencies is believed to be caused by different integral lengths in the turbulence fields of the simulation and experiment. As proposed by (Larose and Mann, 1998) the relation between the vertical integral length scale of the turbulence and the chord length of the bridge section (i.e. $\mathbb{L}_v/c$) significantly effects the coherence function and thus also the aerodynamic admittance of the lift force. Increasing the relation was showed in (Larose and Mann, 1998) to increase the aerodynamic admittance function. This corresponds well with the observed deviations in Fig. III-6 where the simulated relation was $\mathbb{L}_v/c = 1.65$ which is believed to be higher than that of the presented wind tunnel experiments. The exact value of $\mathbb{L}_v/c$ obtained in the wind tunnel experiments (Strømmen et al., 1996; COWI A/S, 2008) are however not reported.

For all bridge section which are investigated in this work a peak is identified in the estimated aerodynamic admittance functions. These peaks are related to the primary vortex shedding of the bridge sections. The vortex shedding occur at a specific frequency related to the geometry of the bridge section and the dynamic characteristics of the oncoming flow. The vortex shedding frequency of the bridge sections for the current simulation parameters along with the corresponding non-dimensional Strouhal numbers are summarised in Tab. III-1.

Aside from the peak associated with vortex shedding it is seen that the Great Belt East bridge has an aerodynamic admittance which is close to that of thin aerofoil theory for the lift force as well as the pitching moment. The same is found regarding the Busan-Geoje bridge when it comes to the aerodynamic admittance of the lift force but a different behaviour is found for the pitching moment. Here the aerodynamic admittance is significantly higher for the frequency range investigated in the simulations. This agrees well with that of the experimental data and is also reported to be a general problem for plate girder bridges (Ito et al., 1991). The original Tacoma Narrows bridge (Farquharson, 1952), the Long Creeks bridge (Ito et al., 1991) and the Kessock bridge (Ito et al., 1991), all with geometries resembling that of the Busan-Geoje bridge, suffered from extensive pitching motion. The same increased aerodynamic admittance is found for both lifting and pitching moment of the Øresund bridge and the Stonecutters bridge whose cross sections consists of multiple structures. The increased aerodynamic admittance may be explained by a aerodynamic interaction between different parts of the structure. Evidently the vortex shedding of one part of the structure can influence the aerodynamic forcing of a downstream part which may result in a increased pitching moment as discussed earlier in Sec. III-3.4.

III-3.6 The effect of a turbulent oncoming flow

It is noticed in the simulations that the turbulent fluctuations of the oncoming wind causes the thickness and separation of the boundary layer on the bridge section to vary in time. This is mostly due to large fluctuations of the angle of attack caused by the turbulence in the oncoming flow. In Fig. III-8 a flow image of a laminar simulation is compared to flow images of two selected time instances of a turbulent simulation which illustrates the instantaneous change in the boundary layer. As mentioned in Sec. III-1 extreme fluctuations of the angle of attack may be experienced even at low turbulence intensities due to an instantaneous synchronization

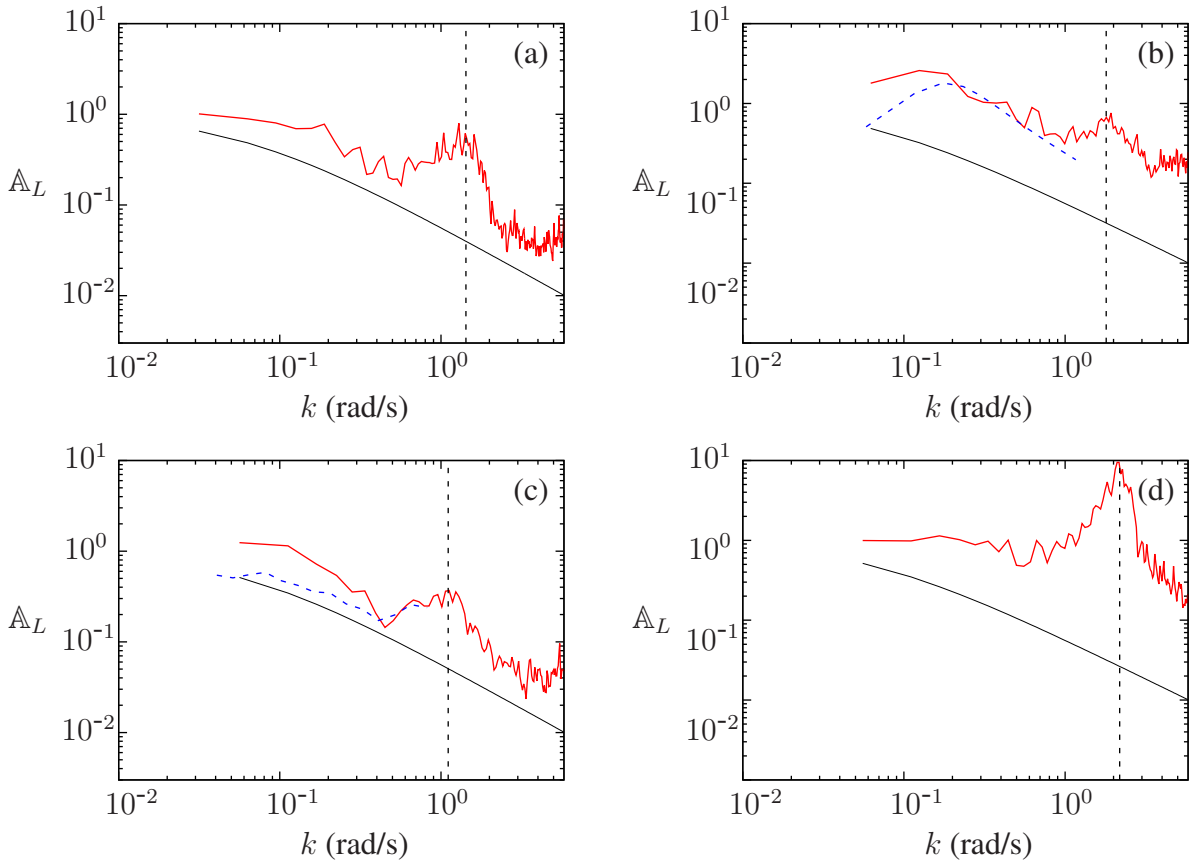

Figure III-6: The estimated aerodynamic admittance functions of the lift force $\mathbb{A}_L$ (full red) compared to the aerodynamic admittance function of thin aerofoil theory $\mathcal{A}_L$ (black), and available experimental result (dashed blue). The estimated Strouhal frequency is indicated by a vertical line (dashed black). (a) Great Belt East bridge, (b) Øresund bridge, (c) Busan-Geoje bridge, (d) Stonecutters bridge.

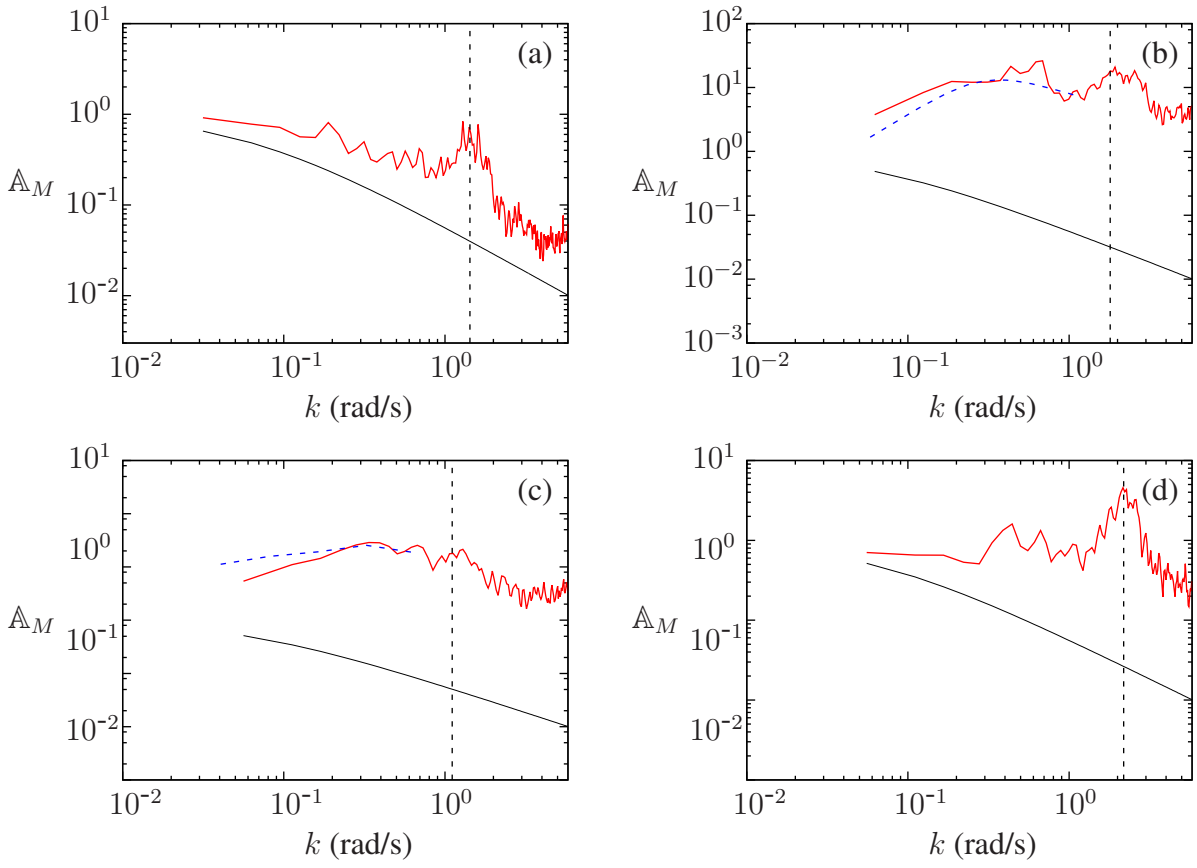

Figure III-7: The estimated aerodynamic admittance functions of the pitching moment $\mathbb{A}_M$ (full red) compared to the aerodynamic admittance function of thin aerofoil theory $\mathcal{A}_M$ (black) and available experimental result (dashed blue). The estimated Strouhal frequency is indicated by a vertical line (dashed black). (a) Great Belt East bridge, (b) Øresund bridge, (c) Busan-Geoje bridge, (d) Stonecutters bridge.

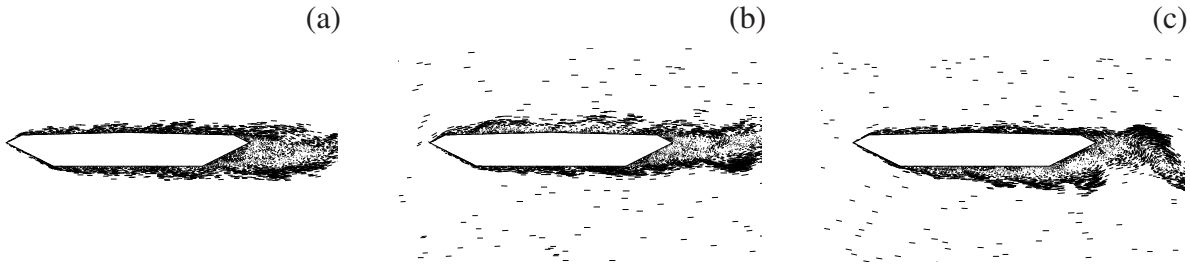

Figure III-8: Laminar flow Time varying separation of the flow around the bridge section. (a) laminar flow, (b) enhanced separation on top, (c) enhanced separation on bottom.

of small flow scales. Such fluctuations may cause the flow to separate on the leading edge bridge section which results in a large change in the aerodynamic forces acting on the bridge section. The phenomenon of extreme angles of attack, though statistically well defined by means of the turbulence intensity, can not be investigated by a spectral analysis but must be studied by the time signal itself. Examples of a time series where the aerodynamic force changes significantly is shown in Fig. III-9 comparing the laminar simulation to the turbulent simulation for turbulence intensities of 2%, 5%, and 7%. For all time series it is seen that large fluctuations cause the lift force to deviate significantly from the mean value and affects the lift force for some time as the boundary layer of the bridge section recovers from the irregular vortex shedding.

III-4 Conclusion

The discrete vortex method was found to be a good method to model the effect of an oncoming turbulent wind. The resulting velocity power spectra of the simulated 2D flow was found to agree well with the semi-empirical spectra of 3D atmospheric turbulence used in the presented stochastic method to create the turbulent flow. In spite of being 2D, the simulated flow showed to preserve most of the statistical characteristics of the generated turbulence with a slight loss of the anisotropic properties which is believed to arise when converting the generated turbulent velocity field into vortex particles.

The modelling of an oncoming turbulent flow in a two-dimensional discrete vortex method was applied to various bridge deck designs in order to extract the aerodynamic admittance function of bridge sections. The method is tested on four specific bridge sections representing the current state of the art bridge decks used in suspension and cable stayed bridges. The estimated aerodynamic admittance functions were compared to available experimental data as well as to Liepmann's approximation to Sears function used in thin aerofoil theory. The spectra extracted from the simulations show a general good agreement with the experimental results, and a deviation from thin aerofoil theory which is well documented in the literature of bluff body aerodynamics. A slight deviation was observed in the lowest frequencies which may to be caused by a different integral lengths in the turbulence fields of the simulation and experiment.

A short investigation was presented to illustrate the instantaneous effects of the oncoming turbulence. Here it was shown that the method can be used to perform temporal analysis to take into account the effect of statistically extreme fluctuations (gusts). Here it was shown that even at small turbulence intensities extreme fluctuations in the aerodynamic force occur creating

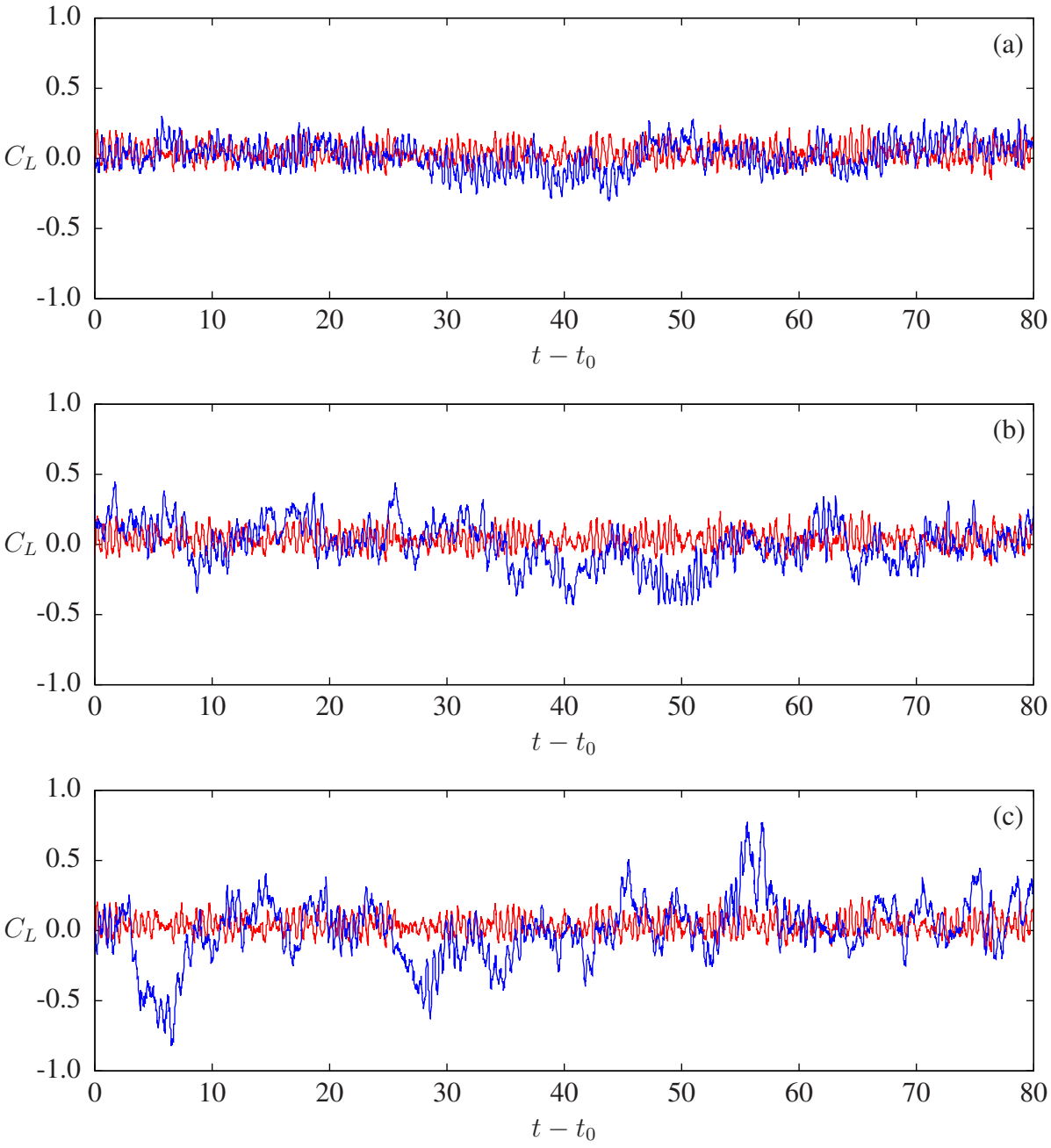

Figure III-9: Time signal of the lift coefficients for the laminar simulation (red) and the turbulent simulation (blue) of the flow around the Great Belt East bridge. Turbulence intensity of (a) 2%, (b) 5% and (c) 7%.

a noticeable difference in the time history of the aerodynamic forces at different turbulence intensities.

Hence the discrete vortex method was found to provide a useful tool to estimate the aerodynamic admittance function as well as investigate other aerodynamic phenomena of bluff bodies under the influence of a turbulent oncoming flow. The method is able to simulate a turbulent oncoming flow with a relation of length scales similar to that of a full scale bridge deck in atmospheric turbulence. Thus the method provides plausible results in a frequency range that significantly exceeded that of the experimental investigations. The parameters of the simulation is easily adjusted such that many different flow conditions can be investigated without extensive modifications, making the method a valuable design tool in bridge aerodynamics.

III-A The modified von Kármán spectra of atmospheric turbulence

The spectral power density function S_u and S_v for the two velocity components u and v are proposed by (ESDU, 1993) as a modified von Kármán spectra:

$$\frac{k\,S_u}{\sigma_u^2} = \beta_1 \frac{2.987\,\dfrac{n_u}{\beta_3}}{\left(1+\left(2\pi\dfrac{n_u}{\beta_3}\right)^2\right)^{5/6}} + \beta_2 \frac{1.294\,\dfrac{n_u}{\beta_3}}{\left(1+\left(\pi\dfrac{n_u}{\beta_3}\right)^2\right)^{5/6}} F_1 \tag{III-18}$$

and:

$$\frac{k\,S_v}{\sigma_v^2} = \beta_1 \frac{2.987\left(1+\dfrac{8}{3}\left(4\pi\dfrac{n_v}{\beta_3}\right)^2\right)\left(\dfrac{n_v}{\beta_3}\right)}{\left(1+\left(4\pi\dfrac{n_v}{\beta_3}\right)^2\right)^{11/6}} + \beta_2 \frac{1.294\,\dfrac{n_v}{\beta_3}}{\left(1+\left(2\pi\dfrac{n_v}{\beta_3}\right)^2\right)^{5/6}} F_2 \tag{III-19}$$

with the reduced frequencies:

$$n_u = \frac{k\,L_u}{U} \qquad \text{and} \qquad n_v = \frac{k\,L_v}{U} \tag{III-20}$$

and F_1 and F_2 being:

$$F_1 = 1{+}0.455\,\exp\left(-0.76\left(\frac{n_u}{\beta_3}\right)^{-0.8}\right) \qquad \text{and} \qquad F_2 = 1{+}2.88\,\exp\left(-0.218\left(\frac{n_v}{\beta_3}\right)^{-0.9}\right). \tag{III-21}$$

$\beta_1 = 0.80$, $\beta_2 = 0.2$, $\beta_3 = 0.662$ are spectral coefficients specified in (Harris, 1990) and the integral length scales L_u and L_v are calculated by:

$$L_u = \frac{A_k^{3/2}\left(\dfrac{\sigma_u}{u_*}\right)^3 y_0}{2.5\,K_z^{3/2}\left(1-\dfrac{y_0}{h}\right)^2\left(1+5.75\dfrac{y_0}{h}\right)} \qquad \text{and} \qquad L_v = L_u\left(0.5\left(\frac{\sigma_v}{\sigma_u}\right)^3\right). \tag{III-22}$$

$A_k^{\frac{3}{2}}$ and $K_z^{\frac{3}{2}}$ are parameters specified in (ESDU, 1993), u_* the shear velocity, h the thickness of the boundary layer and y_0 the height above ground.

Article IV

On stochastically generated turbulence with improved kinematic properties in the velocity and vorticity field

Mads Mølholm Hejlesen[1], Jens Honoré Walther[1,2]

[1]Department of Mechanical Engineering, Technical University of Denmark, Building 403, DK-2800 Kgs. Lyngby, Denmark
[3]Computational Science and Engineering Laboratory, ETH Zürich, Clausiusstrasse 33, CH-8092 Zürich, Switzerland

This chapter consists of an short note which is planned for submission to J. Comput. Phys.

IV-1 Introduction

Stochastic turbulence generators are used in numerical fluid dynamics simulations to emulate the effect of turbulence in a flow. A common use is in simulations of a fluid-structure interaction where a turbulent oncoming flow is implemented in order to investigate the effect of high-frequency fluctuations on the aero-elastic coupling (Prendergast and McRobie, 2006; Prendergast, 2007; Rasmussen et al., 2010; Hejlesen et al., 2015). A stochastic turbulent field is a randomly generated field that possess the same statistical properties as a given real turbulent field but is generally not a solution to the governing equations of fluid flow i.e. the Navier-Stokes equation.

Current stochastic turbulence generators (Mann, 1998; Prendergast, 2007) are based on the method of (Shinozuka and Jan, 1972) for simulating a statistically homogeneous process of the velocity field. However creating the velocity field by a stochastic process does not comply generally to the kinematic constraints of the flow field. Hence the generated turbulent energy is contained in an unconstrained velocity field. Consequently a large part of the kinetic energy may be lost in a numerical simulation when applying kinematic constraints on the unconstrained velocity field e.g. enforcing the divergence-free velocity field of an incompressible flow.

We show that by reformulating the stochastic method to a vorticity formulation some of these constraints are implicitly fulfilled and remaining constraints may be explicitly handled by a reprojection method. This approach ensures that the kinetic energy is contained in components which comply to the kinematics of the flow. Furthermore we discuss how to improve the numerical and physical properties of the generated field to insure that it can be introduced into a numerical simulation with a reduced loss of kinetic energy caused by numerical dissipation.

IV-2 Methodology

A vector field $\boldsymbol{v}$ that has at least two continuous derivatives (i.e. $\boldsymbol{v} \in C^2$) can be viewed as consisting of two intrinsic components according to the Helmholtz decomposition:

$$\boldsymbol{v} = \boldsymbol{\nabla} \times \boldsymbol{\psi} - \boldsymbol{\nabla}\phi \qquad \text{with} \qquad \boldsymbol{\nabla} \cdot \boldsymbol{\psi} = 0 \tag{IV-1}$$

Here ϕ is a scalar potential and $\boldsymbol{\psi}$ is a vector potential which is divergence-free in order to ensure the uniqueness of the decomposition in 3D. The two terms represents a divergence-free and a irrotational component, respectively. Due to the constraint of a incompressible and thus a divergence-free velocity field we have that $\boldsymbol{\nabla}\phi = \boldsymbol{0}$. Using the definition of vorticity $\boldsymbol{\omega} \equiv \boldsymbol{\nabla} \times \boldsymbol{v}$ we obtain the relation:

$$\boldsymbol{\omega} = \boldsymbol{\nabla}(\boldsymbol{\nabla} \cdot \boldsymbol{\psi}) - \boldsymbol{\nabla}^2\boldsymbol{\psi} = -\boldsymbol{\nabla}^2\boldsymbol{\psi} \qquad \text{by which} \qquad \boldsymbol{\nabla} \times \boldsymbol{\omega} = -\boldsymbol{\nabla}^2\boldsymbol{v} \tag{IV-2}$$

Thus we see that by generating a turbulent vorticity field the incompressibility constraint is implicitly fulfilled, in contrast to generating the velocity field directly, by which the kinetic energy is contained within the kinematic constraints.

A correlated random vector field can be generated by convolving a random white noise vector field $\boldsymbol{\phi}$ of unit variance with the desired covariance tensor function $\boldsymbol{H}$. Using index notation with Einstein summation we may expand this to a multi-variate formulation by which the vorticity vector ω_i can be generated by:

$$\omega_i(\boldsymbol{x}) = H_{ij}(\boldsymbol{x}) * \phi_j(\boldsymbol{x}) \qquad \text{and thus} \qquad \widehat{\omega}_i(\boldsymbol{k}) = \widehat{H}_{ij}(\boldsymbol{k})\, \widehat{\phi}_j(\boldsymbol{k}) \tag{IV-3}$$

Here $\widehat{\cdot}$ denotes the Fourier transform and $\boldsymbol{k}$ is the angular the wave-number. In this work the multi-variate formulation simply represents the components of the vorticity vector. However the multi-variate formulation may also be used to introduce a statistically inhomogeneous direction in the turbulence field cf. (Di Paola, 1998). Furthermore, for a turbulent field which is advected with the mean velocity U (e.g. in the x-direction) we may use the Taylor frozen turbulence assumption to transform a spacial dimension into a temporal one e.g. by $\boldsymbol{q} = (U\,t, y, z)$.

In order to find an expression for the covariance tensor H_{ij} we start by defining the desired spectral power density tensor of the turbulent vorticity field:

$$\widehat{\Omega}_{ij}(\boldsymbol{k}) = \frac{\widehat{\omega}_i\, \widehat{\omega}_j^*}{V} = \frac{(\widehat{H}_{ik}\widehat{\phi}_k)\, (\widehat{H}_{jl}\widehat{\phi}_l)^*}{V} \qquad \text{with} \qquad \widehat{\phi}_i\, \widehat{\phi}_j^* = \begin{cases} 1 & \text{for } i = j \\ 0 & \text{for } i \neq j \end{cases} \tag{IV-4}$$

Furthermore as $\Omega_{ij}(\boldsymbol{k})$ is a symmetric matrix with positive, real and even functions of $\boldsymbol{k}$ we may assume that $\widehat{H}_{jk}(\boldsymbol{k})$ is also an even function by which $\widehat{H}_{jk}^* = \widehat{H}_{jk}$. We thus get:

$$V\, \widehat{\Omega}_{ij}(\boldsymbol{k}) = \widehat{H}_{ik}\, \widehat{H}_{kj}^T \tag{IV-5}$$

we see that the multi-variate covariance function $\widehat{H}_{ij}$ may be found by a Cholesky decomposition of the multi-variate spectral vorticity power density function $\widehat{\Omega}_{ij}$ after which the turbulent vorticity field can be generated by Eq. (IV-3) given a well-defined $\widehat{\Omega}_{ij}$.

Letting the multi-variate decomposition represent the three components of the vorticity vector and defining the vorticity as an odd function i.e. $\widehat{\boldsymbol{\omega}}^*(\boldsymbol{k}) = -\widehat{\boldsymbol{\omega}}(\boldsymbol{k})$, the spectral vorticity power density tensor function is obtained:

$$\widehat{\boldsymbol{\Omega}}(\boldsymbol{k}) = -\frac{\widehat{\boldsymbol{\omega}}\,\widehat{\boldsymbol{\omega}}}{V} = \frac{|\widehat{\boldsymbol{v}}|^2(|\boldsymbol{k}|^2\boldsymbol{I} - \boldsymbol{k}\,\boldsymbol{k}) - |\boldsymbol{k}|^2\,\widehat{\boldsymbol{v}}\,\widehat{\boldsymbol{v}}}{V} \tag{IV-6}$$

Here we have used the definition of vorticity $\widehat{\boldsymbol{\omega}} = \iota\,\boldsymbol{k} \times \widehat{\boldsymbol{v}}$ and the incompressibility constraint $\iota\,\boldsymbol{k} \cdot \widehat{\boldsymbol{v}} = 0$. By further assuming an isotropic turbulence, the spectral vorticity power density tensor may be stated as:

$$\widehat{\boldsymbol{\Omega}}(\boldsymbol{k}) = \frac{E(|\boldsymbol{k}|)}{4\pi\,\rho\,|\boldsymbol{k}|^2}(|\boldsymbol{k}|^2\boldsymbol{I} - \boldsymbol{k}\,\boldsymbol{k}) \tag{IV-7}$$

where the $E(|\boldsymbol{k}|)$ is the kinetic energy spectrum (Eq. (IV-7) is also given by (Batchelor, 1953)).

The resulting field that is generated by Eq. (IV-3) is at this point strictly speaking a Monte Carlo method and thus powered by a random number generator. Consequently, the generated field does not posses any properties which allows the field to comply to a numerical simulation of differential equations, e.g. smoothness. Evidently this non-compliance will result in a large numerical dissipation and thus loss of kinetic energy when introducing the turbulent field in a numerical simulation. To amend this, we propose to perform an high order energy conserving smoothing of the turbulence field obtained by the approximate de-convolution method of (Stolz and Adams, 1999; Adams, 2011). Using a Gaussian filter we obtain and m-th order filter from:

$$\widehat{\zeta}(k) = D_m \exp\left(-\frac{\sigma^2\,k^2}{2}\right) \qquad \text{where} \qquad D_m = \sum_{n=0}^{m/2-1} \frac{(\sigma^2\,k^2/2)^n}{n!} \tag{IV-8}$$

where D_m is the m-th order Taylor approximation of the inverse Gaussian, $k = |\boldsymbol{k}|$ and σ is the smoothing radius. The smoothed turbulent vorticity field may now be obtained by:

$$\widehat{\boldsymbol{\omega}}(\boldsymbol{k}) = \widehat{\zeta}(|\boldsymbol{k}|)\,\widehat{\boldsymbol{\phi}}(\boldsymbol{k}) \cdot \widehat{\boldsymbol{H}}(\boldsymbol{k}) \tag{IV-9}$$

Once smoothed we apply an additional correction to the generated vorticity field in order to fulfil another kinematic constraint – that the vorticity field is also divergence-free. From the kinematic relations of Eq. (IV-2) we may deduce that a vorticity field $\boldsymbol{\omega}_*$ where $\boldsymbol{\nabla} \cdot \boldsymbol{\omega}_* \neq 0$ should be corrected accordingly to:

$$\boldsymbol{\omega} = \boldsymbol{\omega}_* + \boldsymbol{\nabla}(\boldsymbol{\nabla} \cdot \boldsymbol{\psi}_*) \qquad \text{where} \qquad \boldsymbol{\nabla} \cdot \boldsymbol{\omega}_* = -\boldsymbol{\nabla}^2(\boldsymbol{\nabla} \cdot \boldsymbol{\psi}_*) \tag{IV-10}$$

The divergence of the uncorrected vector potential $\boldsymbol{\psi}_*$ is found by solving the latter equation which conveniently constitutes a Poisson equation and can thus be easily solved using either spectral differentiation for periodic boundary conditions or by an unbounded Poisson solver e.g. Hejlesen et al. (2013) for free-space boundary conditions. As seen in Eq. (IV-2) we also obtain the velocity field by solving the Poisson equation.

Not only does the vorticity formulation of the turbulence generator provides a field with improved kinematic properties it also allows for an a priori determination of the Kolmogorov length which is the smallest length scale allowed by the viscous damping. By dimensional analysis we reformulate the conventional estimation of the Kolmogorov length as:

$$\eta = \left(\frac{\nu^2}{\overline{\varepsilon}}\right)^{1/4} \tag{IV-11}$$

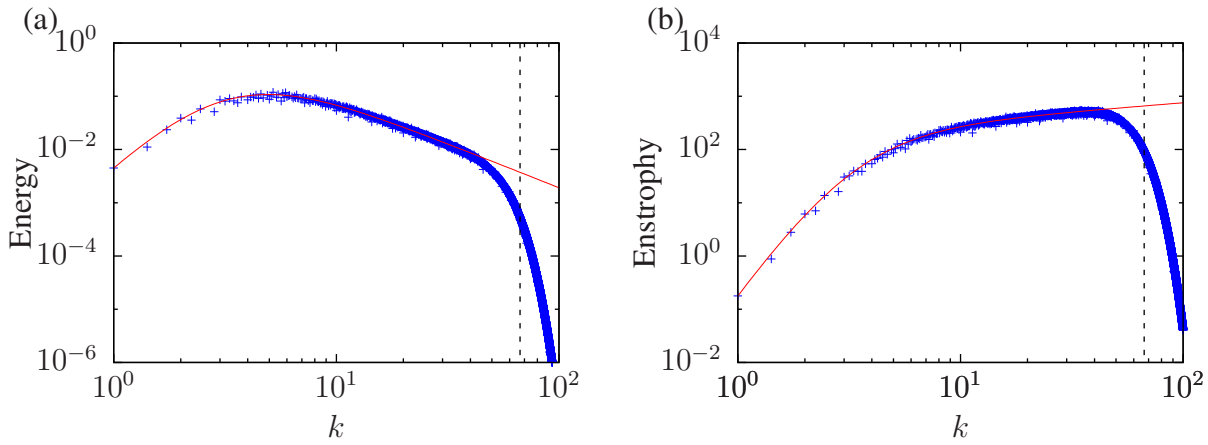

Figure IV-1: The energy spectrum (a) and the enstrophy spectrum (b) of the generated turbulent field. The stochastically generated turbulence field: (———) compared to the target spectra used to generate the field: (———). The wave-number corresponding to the Kolmogorov length:(– – – –).

where ν is the kinematic viscosity of the fluid, $\varepsilon = \boldsymbol{\omega} \cdot \boldsymbol{\omega}$ is the enstrophy density and $\overline{\varepsilon}$ its mean value which evidently can be determined from the generated field. The reformulated Kolmogorov length should be larger than the discretisation length i.e. $\eta > h$ for a direct numerical simulation in order to avoid an excessive numerical dissipation. The Kolmogorov length should additionally be used as the smoothing length σ in order to ensure that the generated kinetic energy is contained in length scales which is allowed by the physics of the fluid.

In Fig. IV-1 the kinetic energy spectrum and the enstrophy spectrum of a generated isotropic turbulence field is shown. The turbulent vorticity field is generated through Eq. (IV-7) using the von Kármán spectrum (von Kármán, 1948) for the turbulent kinetic energy $E(k)$. The von Kármán spectrum is here determined by defining an integral length L, and a scaling parameter $K = \rho \text{ trace}\left(\boldsymbol{\sigma}^2\right)/2$ which is the total turbulent kinetic energy:

$$E(k) = C\frac{L^4k^4}{(1+L^2k^2)^{17/6}} \qquad \text{where} \qquad C = K\left(\int_0^\infty \frac{L^4k^4}{(1+L^2k^2)^{17/6}}\,dk\right)^{-1} \tag{IV-12}$$

Hence we have the two input parameters L and $\boldsymbol{\sigma}$ representing the length scale of the largest coherent flow structures and the turbulence intensity, respectively. For the example shown in Fig. IV-1 (using $L = 0.05$ and $\boldsymbol{\sigma} = \boldsymbol{I}$) the generated turbulence field is shown to agree well to the design spectra. The calculated divergence in the velocity and the vorticity field was observed to be at the order of machine precision.

IV-3 Conclusion

A vorticity formulated stochastic turbulence generator was presented which improved the kinetic properties of the generated turbulent field compared to present methods. Additional measures, such as explicit high order smoothing of the flow field, was introduced to ensure that the generated field can be introduced into numerical simulations without an excessive loss of energy caused by numerical dissipation.

Bibliography

Abramowitz, M., Stegun, I. A., 1972. Handbook of Mathematical Functions With Formulas, Graphs and Mathematical Tables. National Bureau of Standards. Applied Mathematics Series. 55.

Adams, N. A., 2011. A stochastic extension of the approximate deconvolution model. Phys. Fluids 23, 055103.

Anderson, C. R., April 2014. High order expanding domain methods for the solution of Laplace's equation in infinity domains. CAM report 14-44, University of California.

Angot, P., Bruneau, C.-H., Fabrie, P., 1999. A penalization method to take into account obstacles in incompressible viscous flows. Numer. Math. 81, 497–520.

Archer, P. J., Thomas, T. G., Coleman, G. N., 2008. Direct numerical simulation of vortex ring evolution from the laminar to the early turbulent regime. J. Fluid Mech. 598, 201–226.

Ashurst, W. T., Kerstein, A. R., Kerr, R. M., Gibson, C. H., 1987. Alignment of vorticity and scalar gradient with strain rate in simulated Navier-Stokes turbulence. Phys. Fluids 30 (8), 2343–2353.

Barnes, J., Hut, P., 1986. A hierarchical $O(N \log(N))$ force-calculation algorithm. Nature 324 (4), 446–449.

Batchelor, G. K., 1953. The theory of homogeneous turbulence. Cambridge University Press.

Beale, J., Kato, T., Majda, A., 1984. Remarks of the breakdown of smooth solutions for the 3-D Euler equations. Commun. Math. Phys. 94, 61–66.

Beale, J. T., Majda, A., 1982a. Vortex methods. I: Convergence in three dimensions. Math. Comput. 39 (159), 1–27.

Beale, J. T., Majda, A., 1982b. Vortex methods. II: Higher order accuracy in two and three dimensions. Math. Comput. 39 (159), 29–52.

Beale, J. T., Majda, A., 1985. High order accurate vortex methods with explicit velocity kernels. J. Comput. Phys. 58, 188–208.

Bergdorf, M., Cottet, G.-H., Koumoutsakos, P., 2005. Multilevel adaptive particle methods for convection-diffusion equations. Multiscale Model. Simul. 4 (1), 328–357.

Bergdorf, M., Koumoutsakos, P., 2006. A Lagrangian particle-wavelet method. Multiscale Model. Simul. 5 (3), 980–995.

Bergdorf, M., Koumoutsakos, P., Leonard, A., 2007. Direct numerical simulations of vortex rings at $\mathrm{Re}_\gamma = 7500$. J. Fluid Mech. 581, 495–505.

Bernard, P. S., 2006. Turbulent flow properties of large-scale vortex systems. Proc. Natl. Acad. Sci. USA 103 (27), 10174–10179.

Carrier, J., Greengard, L., Rokhlin, V., 1988. A fast adaptive multipole algorithm for particle simulations. SIAM J. Sci. Stat. Comput. 9 (4), 669–686.

Chatelain, P., Koumoutsakos, P., 2010. A Fourier-based elliptic solver for vortical flows with periodic and unbounded directions. J. Comput. Phys. 229, 2425–2431.

Chorin, A. J., 1973. Numerical study of slightly viscous flow. J. Fluid Mech. 57 (4), 785–796.

Christiansen, J. P., 1973. Numerical simulation of hydrodynamics by the method of point vortices. J. Comput. Phys. 13, 363–379.

Coquerelle, M., Cottet, G.-H., 2008. A vortex level set method for the two-way coupling of an incompressible fluid with colliding rigid bodies. J. Comput. Phys. 227 (21), 9121–9137.

Costa, C., 2007. Aerodynamic admittance functions and buffeting forces for bridges via indicial functions. J. Fluids and Structures 23, 413–428.

Cottet, G.-H., Koumoutsakos, P., 2000. Vortex Methods – Theory and Practice. Cambridge University Press, New York.

Cottet, G.-H., Koumoutsakos, P., Salihi, M. L. O., 2000. Vortex methods with spatially varying cores. J. Comput. Phys. 162 (1), 164–185.

COWI A/S, 2008. Busan-Geoje fixed link - Admittance function.

Davenport, A. G., 1968. The dependence of wind load upon meteorological parameters. Proceedings of the International Research Seminar on Wind Effects on Buildings and Structures, 19–82.

Di Paola, M., 1998. Digital simulation of wind field velocity. J. Wind Eng. Ind. Aerodyn. 74, 91–109.

El Ossmani, M., Poncet, P., 2010. Efficiency of multiscale hybrid grid-particle vortex methods. Multiscale Model. Simul. 8 (5), 1671–1690.

ESDU, 1993. Characteristics of atmospheric turbulence near the ground, part ii: single point data for strong winds (neutral atmosphere). Tech. rep., Engineering Sciences Data Unit.

ESDU, 2001. Characteristics of atmospheric turbulence near the ground, part iii: variations in space and time for strong winds (neutral atmosphere). Tech. rep., Engineering Sciences Data Unit.

Farquharson, F. B., 1952. Aerodynamic stability of suspension bridges. Tech. rep., University of Washington Experiment Station, no. 116 Part I and III.

Gazzola, M., Chatelain, P., van Rees, W. M., Koumoutsakos, P., 2011. Simulations of single and multiple swimmers with non-divergence free deforming geometries. J. Comput. Phys. 230, 7093–7114.

Gazzola, M., Hejazialhosseini, B., Koumoutsakos, P., 2014. Reinforcement learning and wavelet adapted vortex methods for simulations of self-propelled swimmers. SIAM J. Sci. Comput., in press.

Greengard, L., Rokhlin, V., 1987. A fast algorithm for particle simulations. J. Comput. Phys. 73, 325–348.

Griebel, M., Knapek, S., Zumbusch, G. W., 2007. Numerical Simulation in Molecular Dynamics. Springer-Verlag, Berlin.

Gu, M., Qin, X. R., 2004. Direct identification of flutter derivatives and aerodynamic admittances of bridge decks. Engng. Struct. 26 (14), 2161–2172.

Hald, O. H., 1987. Convergence of vortex methods for Euler's equations, III. SIAM J. Numer. Anal. 24 (3), 538–582.

Harris, R. I., 1990. Some further thoughts on the spectrum of gustiness in strong winds. J. Wind Eng. Ind. Aerodyn. 33, 461–477.

Hatanaka, A., Tanaka, H., 2002. New estimation method of aerodynamic admittance function. J. Wind Eng. Ind. Aerodyn. 90, 2073–2086.

Hejlesen, M. M., Rasmussen, J. T., Chatelain, P., Walther, J. H., 2013. A high order solver for the unbounded Poisson equation. J. Comput. Phys. 252, 458–467.

Hejlesen, M. M., Rasmussen, J. T., Larsen, A., Walther, J. H., 2015. On estimating the aerodynamic admittance of bridge sections by a mesh-free vortex method. J. Wind Eng. Ind. Aerodyn. 146, 117–127.

Hockney, R. W., Eastwood, J. W., 1988. Computer Simulation Using Particles, 2nd Edition. Institute of Physics Publishing, Bristol, PA, USA.

Ito, M., Fujino, Y., Miyata, T., Narita, N., December 1991. Cable-stayed bridges-recent developments and their future. In: (Ed.), Proceedings of the Seminar. Elsevier, Amsterdam.

Jancauskas, E. D., Melbourne, W. H., 1986. The aerodynamic admittance of two-dimensional rectangular section cylinders in smooth flow. J. Wind Eng. Ind. Aerodyn. 23, 395–408.

Jiménez, J., Wray, A. A., 1998. On the characteristics of vortex filaments in isotropic turbulence. J. Fluid Mech. 373, 255–285.

Jimenez, J., Wray, A. A., Saffman, P. G., Rogallo, R. S., 1993. The structure of intense vorticity in isotropic turbulence. J. Fluid Mech. 2545, 65–90.

Kevlahan, N. K.-R., Ghidaglia, J.-M., 2001. Computation of turbulent flow past an array of cylinders using a spectral method with Brinkman penalization. Eur. J. Mech., B 20, 333–350.

Körner, T. W., 1988. Fourier Analysis. Cambridge University Press, Cambridge.

Koumoutsakos, P., 1997. Inviscid axisymmetrization of an elliptical vortex ring. J. Comput. Phys. 138, 821–857.

Koumoutsakos, P., 2005. Multiscale flow simulations using particles. Annu. Rev. Fluid Mech. 37, 457–487.

Koumoutsakos, P., Leonard, A., 1995. High-resolution simulation of the flow around an impulsively started cylinder using vortex methods. J. Fluid Mech. 296, 1–38.

Koumoutsakos, P., Leonard, A., Pépin, F., 1994. Boundary conditions for viscous vortex methods. J. Comput. Phys. 113 (1), 52–61.

Koumoutsakos, P., Shiels, D., 1996. Simulations of the viscous flow normal to an impulsively started and uniformly accelerated flat plate. J. Fluid Mech. 328, 177–227.

Larose, G. L., 2003. The spatial distribution of unsteady loading due to gusts on bridge decks. J. Wind Eng. Ind. Aerodyn. 91, 1431–1443.

Larose, G. L., Mann, J., 1998. Gust loading on streamlined bridge decks. J. Fluids and Structures 12, 511–536.

Larsen, A., 1993. A generalized model for assessment of vortex-induced vibrations of flexible bridges. In: Seventh United States National Wind Engineering Conference, University of California, Los Angeles, June 27-30, 1993. Wind Engineering Research Council, pp. 383–392.

Larsen, A., Walther, J. H., 1997. Aeroelastic analysis of bridge girder sections based on discrete vortex simulations. J. Wind Eng. Ind. Aerodyn. 67–68, 253–265.

Lawson, T., 1980. Wind effects on building. Applied Science Publishers Ltd., London.

Leonard, A., 1980. Vortex methods for flow simulation. J. Comput. Phys. 37, 289–335.

Liepmann, H. W., 1952. On the application of statistical concepts to the buffeting problems. J. Aero. Sci. 19 (12), 793–800.

Luty, B. A., van Gunsteren, W., 1996. Calculating electrostatic interactions using the particle-particle particle-mesh method with nonperiodic long-range interactions. J. Phys. Chem. 100, 2581–2587.

Mann, J., 1998. Wind field simulation. Prob. Engng. Mech. 13 (4), 269–282.

Monaghan, J. J., 1985. Extrapolating B splines for interpolation. J. Comput. Phys. 60 (2), 253–262.

Morgenthal, G., October 2002. Aerodynamic analysis of structures using high-resolution vortex particle methods. Ph.D. thesis, Department of Engineering. University of Cambridge.

Morgenthal, G., Walther, J. H., 2007. An immersed interface method for the vortex-in-cell algorithm. Computers & Structures 85, 712–726.

Moser, R. D., Kim, J., Mansour, N. N., 1999. Direct numerical simulation of turbulent channel flow up to $\mathrm{Re}_\tau = 590$. Phys. Fluids 11 (4), 943–945.

Olver, F. W. J., Lozier, D. W., Boisvert, R. F., Clark, C. W., 2010. NIST handbook of mathematical functions. Cambridge University Press, New York.

Perlman, M., 1985. On the accuracy of vortex methods. J. Comput. Phys. 59, 200–223.

Powell, A., 1964. Theory of vortex sound. J. Acoust. Soc. Am. 36 (1), 177–195.

Prendergast, J., 2007. Simulation of unsteady 2-D wind by a vortex method. Ph.D. thesis, Department of Engineering. University of Cambridge.

Prendergast, J. M., McRobie, F. A., 2006. Simulation of 2D unsteady wind by a vortex method and application to studying bluff body flow. In: 7th UK Conference on Wind Engineering.

Rasmussen, J. T., October 2011. Particle methods in bluff body aerodynamics. Ph.D. thesis, Technical University of Denmark.

Rasmussen, J. T., Cottet, G.-H., Walther, J. H., 2011. A multiresolution remeshed vortex-in-cell algorithm using patches. J. Comput. Phys. 230 (17), 6742–6755.

Rasmussen, J. T., Hejlesen, M. M., Larsen, A., Walther, J. H., 2010. Discrete vortex method simulations of the aerodynamic admittance in bridge aerodynamics. J. Wind Eng. Ind. Aerodyn. 98, 754–766.

Rossi, R., Lazzari, M., Vitaliani, R., 2004. Wind field simulation for structural engineering purposes. Int. J. for Numer. Methods In Engng. 61 (5), 738–763.

Rossinelli, D., Bergdorf, M., Cottet, G.-H., Koumoutsakos, P., 2010. GPU accelerated simulations of bluff body flows using vortex particle methods. J. Comput. Phys. 229 (89), 3316–3333.

Saffman, P. G., 1992. Vortex Dynamics. Cambridge University Press.

Sagaut, P., 1998. Large Eddy Simulation for Incompressible Flows. Springer.

Sbalzarini, I. F., Walther, J. H., Bergdorf, M., Hieber, S. E., Kotsalis, E. M., Koumoutsakos, P., 2006. PPM – a highly efficient parallel particle-mesh library for the simulation of continuum systems. J. Comput. Phys. 215, 566–588.

Schneider, K., Farge, M., 2002. Adaptive wavelet simulation of a flow around an impulsively started cylinder using penalization. Appl. Comput. Harmon. Anal. 12, 374–380.

Shariff, K., Leonard, A., 1992. Vortex rings. Annu. Rev. Fluid Mech. 24, 235–279.

Shinozuka, M., Jan, C.-M., 1972. Digital simulation of random processes and its applications. J. Sound Vibration 25 (1), 111–128.

Solari, G., 1987. Turbulence modeling for gust loading. J. Struct. Engng. 113, 1550–1569.

Spietz, H. J., Hejlesen, M. M., Walther, J. H., June 2016. Simulation of bluff-body flows using iterative penalization in a multiresolution particle-mesh vortex method. In: ECCOMAS Congress 2016.

Spietz, H. J., Hejlesen, M. M., Walther, J. H., Larsen, A., November 2015. Simulating external flow using vortex method in two- and three dimensions. In: American Physical Society, 68th Annual Meeting of the Division of Fluid Dynamics. American Physical Society, Boston, Massachusetts.

Stolz, S., Adams, N. A., 1999. An approximate deconvolution procedure for large-eddy simulation. Phys. Fluids 11 (7), 1699–1701.

Strømmen, E., Hjorth-Hansen, E., Hansen, S. O., Bogunovic Jakobsen, J., 1996. Wind tunnel tests for the Öresund link bridge, report no. 1, high bridge - section model test. Tech. rep., Sundlink.

van Rees, W. M., Leonard, A., Pullin, D. I., Koumoutsakos, P., 2011. A comparison of vortex and pseudo-spectral methods for the simulation of periodic vortical flows at high Reynolds numbers. J. Comput. Phys. 230, 2794–2805.

Vasilyev, O. V., Kevlahan, N. K.-R., 2002. Hybrid wavelet collocation-Brinkman penalization method for complex geometry flows. Int. J. Numer. Meth. Fluids 40, 531–538.

Villumsen, J. V., 1989. A new hierarchical particle-mesh code for very large scale cosmological n-body simulations. The Astro. J. Supp. 71, 407–431.

von Kármán, T., 1948. Progress in the statistical theory of turbulence. Proceedings of the National Academy of Sciences of the United States of America 34 (11), 530–539.

Wallace, J. M., 2009. Twenty years of experimental and direct numerical simulation access to the velocity gradient tensor: What have we learned about turbulence? Phys. Fluids 21 (021301), 1–17.

Walther, J. H., September 1994. Discrete vortex method for two-dimensional flow past bodies of arbitrary shape undergoing prescribed rotary and translational motion. Ph.D. thesis, Department of Fluid Mechanics. Technical University of Denmark, unpublished.

Walther, J. H., 2003. An influence matrix particle-particle particle-mesh algorithm with exact particle-particle correction. J. Comput. Phys. 184, 670–678.

Walther, J. H., Larsen, A., 1997. Two dimensional discrete vortex method for application to bluff body aerodynamics. J. Wind Eng. Ind. Aerodyn. 67–68, 183–193.

Wang, C., Eldredge, J. D., 2013. Low-order phenomenological modeling of leading-edge vortex formation. Theor. Comput. Fluid Dyn. 27, 577–598.

Welch, P. D., 1967. The use of fast Fourier transform for the estimation of power spectra: a method based on time averaging over short, modified periodograms. IEEE Transactions on audio and electroacoustics 15 (2), 70–73.

Winckelmans, G. S., Leonard, A., 1993. Contribution to vortex particle methods for the computation of three-dimensional incompressible unsteady flows. J. Comput. Phys. 109, 247–273.

Wu, J. C., 1976. Numerical boundary conditions for viscous flow problems. AIAA J. 14 (8), 1042–1049.

Wu, J. C., September 1978. A theory for aerodynamic forces and moments. Technical report, Georgia Institute of Technology.

Wu, J. C., 1981. Theory for aerodynamics force and moments in viscous flows. AIAA J. 19 (4), 432–441.

Wu, J.-Z., Ma, H.-Y., Zhou, M.-D., 2006a. Vorticity and Vortex Dynamics. Springer-Verlag, Berlin Heidelberg New York.

Wu, Y., Tepper, H. L., Voth, G. A., 2006b. Flexible simple point-charge water model with improved liquid-state properties. J. Chem. Phys. 124, 024503.

Zeff, B. W., Lanterman, D. D., McAllister, R., Roy, R., Kostelich, E. J., Lathrop, D. P., 2003. Measuring intense rotation and dissipation in turbulent flows. Nature 421, 146–149.

DTU Mechanical Engineering
Section of Thermal Energy
Technical University of Denmark

Nils Koppels Allé, Bld. 403
DK-2800 Kgs. Lyngby
Denmark
Phone (+45) 4525 4131
Fax (+45) 4588 4325
www.mek.dtu.dk
ISBN: 978-87-7475-444-2

DCAMM
Danish Center for Applied Mathematics and Mechanics

Nils Koppels Allé, Bld. 404
DK-2800 Kgs. Lyngby
Denmark
Phone (+45) 4525 4250
Fax (+45) 4593 1475
www.dcamm.dk
ISSN: 0903-1685